Cavity Optomechanics with nm-Thick Membranes



Anna Pearson

Supervisors: Prof G.A.D. Briggs & Dr N. Ares

St Anne's College

University of Oxford

A thesis submitted for the degree of

Doctor of Philosophy

Trinity 2020

This thesis is dedicated to
those who helped and inspired me along the way
- you know who you are.

Acknowledgements

Professional

One of my favourite things about science is the fact that it crosses continents. This thesis is in part the result of fruitful international collaboration. I wish to thank all the co-authors I have worked with (outlined in the next section), I learned a lot from you all and it was a joy to work with you, as well as thanking Prof Gerard Milburn for guidance and academic inspiration, and Dr Matt Woolley and Dr Matt Matheny for useful discussions.

There are a few people who I need to acknowledge whose work is included in this thesis. The first is Dr Yelena Guryanova who in collaboration did the data analysis of the data I took for chapter 3. The second is Dr Kiran Khosla, who as a PhD student supervised by Prof Gerard Milburn did the calculation in section 6.2 with his derivation being included in appendix B. The sensitivity estimate in section 6.4 was done by Dr Edward Laird. An extra special thanks goes to my supervisors Dr Natalia Ares and Prof Andrew Briggs who have taught, encouraged, inspired, obtained funding and helped me along the rocky path of learning to become a scientist. None of this would have been possible without them and I wish to express my heartfelt thanks to both of them for believing in me, especially when I doubted myself.

I would not have been able to carry out this doctorate without funding, and so I am indebted to Maria and David Ferreras-Willetts who extended their philanthropy to encourage a young woman to pursue a career in the sciences. My thanks for standing behind me both financially, allowing for the international travel I have been able to undertake, and also in spirit. I also wish to thank St Anne's College for the college fee scholarship.

Personal

It is not with a small sigh of a relief that I reach the end of and submit this thesis, having discovered that mechanical signals can be quite taxing to work with (at least when one is starting out). Thankfully, this has not been a journey that I have had to take alone, as already mentioned I have had the pleasure of working

with two wonderful supervisors as well as a fantastic group of colleagues in the Materials department who I am scared to name by name least I miss someone out. To risk mentioning a few, my office and lab mates - Dr Florian Vigneau, Dr Yutian Wen, Dr Nicola Dotti, Dr Reuben Harding, Dominic Lennon, Jonas Schuff and Nina van Esbroeck gave a real sense of community and the cleanroom and lab managers Paul Pattinson, Radka Chakalova, Tom Orton and Dr Serkan Kaya were all incredibly helpful and approachable.

I wish to thank my mentor and friend Dr Bethany Sollereder. Her cheery smile, friendship and steady repetition of *just keep going, one step at a time* week in and week out really helped me when the going got tough. My uncle Dr Nigel Pearson gave me a place to live for two years and was also a steady source of encouragement. Other friends whose support made this possible include, but are not limited to, Sarah Bruhn, Mari Ovsepyan, Andrius Vaicenavičius, Katie Fisher, Kezia Gaitskell, Alison Laurele and the other members of Wadham Chapel Choir and Chapel community (in particular the Rev Wendy Wale and choir director Dr Katharine Pardee), the members of St Anne's MCR, and housemates past and present. Heather Munro and Wendy and Tom Wale looked after me when I first got ill and in addition the pastoral team at St Aldate's church, and the members of Lliswerry Baptist Church have been a tremendous help, as were the team at OCCA during my first year. The work of CiS (Christians in Science), The Faraday Institute, and the Oxford Pastorate has been a steady encouragement for me to stay in the sciences, so a big thank you to all the staff and volunteers who enable that work to continue.

Oskar you appeared on the scene towards the end of this work, but you have encouraged me in more ways than one. I want to thank my family; my parents, brothers, aunts and uncles, cousins and grandparents. I'm blessed to have such an amazing group of people to call my family. I don't know what I would do without you all.

I would also like to acknowledge the college community at St Anne's in addition to the aforementioned MCR. I always said that I would include *Spotify* in my acknowledgements so I had better do so, music really does help me work.

To end, my final acknowledgement is that my motivation for studying foundational questions is not to serve the one whom I believe in, but to honour Him. As my tradition states: *The God who made the world and everything in it is the Lord of heaven and earth and does not live in temples built by human hands. And he is not served by human hands, as if he needed anything. Rather, he himself gives everyone life and breath and everything else..... For in him we live and move and have our being.*

Publications and Conference Presentations

Publications

The data presented in chapter 2 is included in the following publication:

Pearson, A. N., Khosla, K. E., Mergenthaler, M., Briggs, G. A. D., Laird, E. A., and Ares, N. Radio-frequency optomechanical characterization of a silicon nitride drum *Scientific reports*, **10**, 1654 (2020).

The data presented in chapter 3 is included in the following publication (which will be uploaded to the Arxiv in time for the *Viva* examination):

Pearson, A.N., Guryanova, Y., Erker, P., Laird, E.A., Briggs, G.A.D., Huber, M., and Ares, N. Measuring the thermodynamic cost of timekeeping *arXiv:2006.08670*

In addition the following book chapter is in press:

Ares, N., Pearson, A.N., and Briggs, G.A.D. Eight Oxford Questions: Quantum Mechanics under a new light *In: Do wave functions jump?* in honour of G.C. Ghirardi *In press, Springer* Editor: Angelo Bassi

Conference Presentations

July 2019 Poster at Summer School Nanotechnology meets Quantum Information, San Sebastian: Circuit Optomechanics with Silicon Nitride Membranes

May 2019 Invited visit and talk at the Institute for Quantum Optics and Quantum Information in Vienna (Huber group): Radio-frequency Optomechanical Characterization of a Silicon Nitride Drum

March 2019 Talk at APS March Meeting, Boston: Radio-frequency Optomechanical Characterization of a Silicon Nitride Drum

January 2019 Talk at Workshop Quantum Networks and Non-Equilibrium Systems, Obergurgl: Radio-frequency Optomechanical Characterization of a Silicon Nitride Drum

November 2018 Talk at 2nd Quantum User Meeting (Zurich Instruments), London: Radio-frequency Optomechanical Characterization of a Silicon Nitride Drum

September 2017 Poster at Summer School Complex Quantum Systems, Vienna: Circuit Optomechanics with Silicon Nitride Membranes

September 2015 Poster at Conference Experimental Tests of Quantum Reality, Oxford: Controversy in Quantum Mechanics – The Skeleton of Contention that gives Life to the Debate.

Abstract

This thesis focuses on fast and sensitive readout of mechanical motion to answer questions in the foundations of physics. By coupling a silicon nitride membrane to different readout cavities I have explored the thermodynamic costs of time keeping and carried out a bench-top experiment to put bounds on the theory of classical channel gravity. In order to reach these aims, I have developed real time displacement measurements of the motion of a nm-thick silicon nitride membrane. For this, a lumped element LC circuit is capacitively coupled to the metallized silicon nitride membrane. This approach allows for the estimation of key parameters without the need for frequency matching or cryogenic cooling. I demonstrate electromechanical characterization of several mechanical modes of the silicon nitride membrane. In addition, I show optomechanically induced transparency on chip in this high loss cavity.

The real time displacement measurements of the membrane's motion allow the device to be operated as a thermomechanical clock and to be used to investigate a thermodynamic trade-off in a nanoscale clock. The system follows a trade-off derived for the idealised quantum setting, indicating a fundamental universality of a relation previously predicted to hold in the quantum regime.

This system is compatible with cryogenic temperatures, allowing me to actuate and detect the resonance frequency of a membrane at low temperatures. At these temperatures, one can perform tests of the theory of classical channel gravity which models the gravitational interaction as a classical measurement channel. The theory predicts a density dependent heating effect due to the gravitational interactions within the membrane itself. Bounds could be put on this theory using a membrane capacitively coupled to a 3D superconducting microwave cavity which has a much higher Q factor than the LC circuit. With this cavity, I achieved 10 mHz resolution of the mechanical signal, which is required for an accurate estimation of the mode temperature and thus to put bounds on the theory.

Contents

1 Introduction **1**

1.1 Cavity Optomechanics 2

1.2 Micro and Nano-Electromechanical Resonators (MEMS/NEMS) . . 5

1.3 Fundamental Tests of Physics using MEMS and NEMS 6

1.3.1 Cooling to the Ground State 7

1.3.2 The Creation of Massive Superpositions 10

1.3.3 Testing of Collapse Theories 12

1.3.4 Other Achievements 14

2 Radio Frequency Probing of Mechanical Motion **17**

2.1 Device Fabrication 18

2.2 The Circuit (Cavity) 18

2.3 Coupling to the Cavity 22

2.4 Direct Driving of the Membrane 23

2.5 Driving the Membrane with White Noise 24

2.5.1 Mechanical Quality Factors 27

2.5.2 Extraction of g_0 from Mechanical Sidebands 28

2.6 Optomechanically Induced Transparency 30

2.7 Time Domain Measurements 33

3 Thermomechanical Clocks **35**

3.1 Background: Autonomous Clocks 36

3.2 Experimental Determination of a Thermodynamic Trade-off in a Nanoscale Clock 39

3.3 Discussion 44

4 Radio Frequency Probing of Mechanical Motion at Cryogenic Temperatures **47**

4.1 Measuring Motion at Cryogenic Temperatures 47

4.2 Direct Driving of the Membrane 48

4.3 Driving the Membrane with White Noise 51

4.4 Discussion 53

5 Microwave Optomechanics with a 3D Cavity **55**
5.1 Device Design 56
5.2 Measuring Superconducting Cavities at Cryogenic Temperatures . . 57
5.3 Measurements of Electromechanical Sidebands 60
5.4 Increasing the Measurement Resolution 61
5.5 Determination of the Mode Temperature 64
5.6 Discussion 67

6 A Test of Classical Channel Gravity **68**
6.1 Gravitation as an Observer of Quantum States 69
6.2 The Predicted Heating Rate of a SiN Membrane 71
6.3 Experimental Results 73
6.4 Estimating the Sensitivity of the Setup 75
6.5 Outlook 77

7 Conclusion **78**

Appendices

A Extraction of g_0 from Thermomechanical Sidebands: Theory **82**

B Derivation of the Heating Rate of a Silicon Nitride Membrane **85**

References **89**

1 Introduction

Contents

1.1 Cavity Optomechanics 2
1.2 Micro and Nano-Electromechanical Resonators (MEMS/NEMS) 5
1.3 Fundamental Tests of Physics using MEMS and NEMS 6
1.3.1 Cooling to the Ground State 7
1.3.2 The Creation of Massive Superpositions 10
1.3.3 Testing of Collapse Theories 12
1.3.4 Other Achievements 14

Any Physics graduate will have learnt to accept the strange goings on of the quantum realm, superpositions are standard due to the linearity of the solutions to the Schroedinger equation, probabilities rather than certainties are the currency of the trade and all of this only goes on while one 'isn't looking.' Whilst one can 'sit tight and it will all come out in the wash' (the sound advice of an undergraduate lecturer to his students when faced with blackboards of algebra) there is a certain dissatisfaction with our current understanding of the quantum realm. The answer to all this of course is experiments (informed by theory of course, but this is an experimentalist writing).

That is where this thesis comes in, it is a small step, a very small step, in an attempt towards filling in some of the gaps in our understanding of foundational

questions in physics. Specifically, I focus on using fast and sensitive readout of mechanical motion.

There are two main foundational questions that I have sought to answer during the course of this doctorate. The first is *Do trade-offs pertaining to the thermodynamics of time keeping, derived in the quantum domain, hold for a larger more complex system?*. To answer this I have developed an electromechanical system that consists of a silicon nitride membrane capacitively coupled to an LC circuit (described in chapter 2). The system allows me to read out in real time the oscillations of the membrane, which can be thought of as the ticks of a clock. Noise is injected to the system to act as an effective heat bath providing the perfect testbed for the investigation of the thermodynamics of time keeping (chapter 3). In chapter 4 the system is shown to be compatible with cryogenic temperatures which provides a tool for efficient characterization of membranes at low temperatures and sets the stage for the second question I seek to answer, namely *Is the gravitational interaction classical rather than quantum?* In an attempt to put bounds on the theory of classical channel gravity the silicon nitride membrane is placed inside and capacitively coupled to a superconducting 3D microwave cavity at cryogenic temperatures. Chapter 5 describes the experimental setup and chapter 6 outlines the theory of classical channel gravity and presents my experimental results. Chapter 7 summarises the results presented in this thesis. This current chapter will explain the background physics required for the subsequent ones.

1.1 Cavity Optomechanics

The domain of physics which this work falls into is Cavity Optomechanics which is the study of the interaction between electromagnetic radiation and mechanical motion. For a comprehensive review of the field see Ref. [1], which this brief outline follows and unless otherwise stated is where all the equations in this section are taken from.

I studied the interaction of radio frequency (rf) and microwave radiation and the motion of a metallized silicon nitride membrane. For conceptual understanding it can be easiest to visualise the physical goings on in the optical regime. The

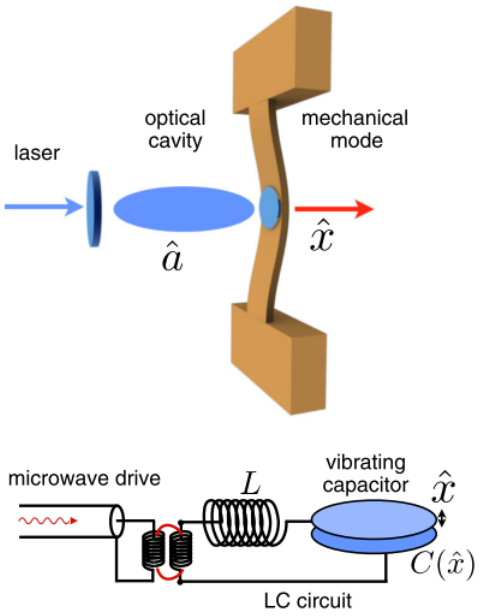


Figure 1.1: A generic optomechanical system in the optical domain (top) and the microwave domain (bottom) from [1]

theory derived for radiation in the optical regime holds for rf and microwaves as well. Figure 1.1 shows two schematics for the experimental implementation of this interaction. A Fabry-Perot resonator or cavity is made up of two highly reflective mirrors separated by a distance L. It will exhibit resonances of angular frequency $\omega = n \cdot \pi \frac{c}{L}$ with integer spacing n and where c is the speed of light. Most experiments only use one cavity mode denoted as ω_C

A cavity is further characterised by its quality factor

$$Q = \omega_C / \kappa \tag{1.1}$$

where κ is the inverse of the photon lifetime or the cavity decay rate (also known as the cavity linewidth). The quality factor denotes the number of times a photon will circulate inside the cavity before decaying/leaving the cavity. The decay rate has two contributions; $\kappa = \kappa_e + \kappa_i$. κ_e is the external loss rate associated with the input coupling and κ_i is the internal loss rate or the loss rate from within the cavity.

The coupling to the cavity is controlled by κ_e and three different regimes exist. If κ_e dominates the decay rate (i.e. the internal losses are very small) the cavity is

said to be overcoupled. In this case very few photons are absorbed or lost inside the cavity. If $\kappa_e = \kappa_i$ the cavity is said to be critically coupled and it means that on resonance zero photons are reflected from the cavity as they are fully dissipated within the resonator. If κ_e is much smaller than κ_i the cavity is undercoupled and means that the losses are dominated by internal losses. This can be a disadvantage in experiments as it leads to a loss of information (some photons that reach the cavity are not reflected back to the measuring apparatus as they are lost within the cavity).

In the Fabry-Perot model one of the mirrors of the cavity is free to move and thus acts as a mechanical resonator. As it moves it changes the length L of the cavity subsequently changing ω_C. As the mirror moves it changes the phase and amplitude of photons inside the cavity, hence photons leaving the cavity carry information about the position of the mirror. In addition to the mechanics affecting the phase and amplitude of the photons, the photons also affect the position of the mechanics. Each photon that impinges on the mirror imparts a momentum kick of $2h/\lambda$, (where h is Planck's constant and λ is the wavelength of the photon) with this interaction being known as the radiation pressure interaction or measurement backaction. In the Fabry-Perot model this changes the position of the mirror that is free to move and this length change changes the resonant frequency of the cavity. This frequency shift per unit displacement is given by the optomechanical coupling strength G

$$G \equiv \frac{\delta\omega_C(x)}{\delta x} \tag{1.2}$$

$$= \frac{\omega_C}{L} \tag{1.3}$$

The vacuum optomechanical coupling rate gives the frequency shift per zero-point oscillation of the mechanical resonator and is defined as

$$g_0 \equiv G x_{ZPM} \tag{1.4}$$

where x_{ZPM} is the zero point motion of the resonator and is given by

$$x_{ZPM} \equiv \sqrt{\frac{\hbar}{2m\omega_m}} \tag{1.5}$$

where $\hbar$ is Planck's constant divided by 2π, m is the mass and ω_m is the resonant angular frequency of the mechanical resonator.

As radiation pressure can be controlled by controlling the number of photons impinging on the mechanical resonator, the motion of the mechanical resonator can be controlled. g is known as the optomechanical coupling strength which is the vacuum optomechanical coupling g_0 enhanced by the strength of the drive

$$g \equiv g_0\sqrt{\bar{n}_{cav}} \tag{1.6}$$

where $\bar{n}_{cav}$ is the average number of photons in the cavity.

If the condition $g > \kappa$ is met the system is in the strong coupling regime in which the mechanical resonator and the driven cavity mode hybridize. If the much more stringent condition of $g_0 > \kappa$ is met then nonlinear quantum effects become observable.

This type of coupling, where it is in the resonant frequency of the cavity which changes, is known as dispersive coupling and is the most commonly implemented way of coupling mechanical motion to cavities. The motion of the mechanical resonator can also change the cavity linewidth [2] with this type of coupling being known as dissipative coupling. This thesis focuses on dispersive coupling.

In the rf or microwave regime the picture remains the same with either a coplanar waveguide, LC circuit or 3D microwave cavity acting as an rf or microwave 'cavity' with resonant frequency $\omega_C = 1/\sqrt{LC}$. The mirror in the Fabry-Perot model is replaced by one plate of a capacitor which is free to move. As it moves the capacitance of the circuit changes, changing the resonant frequency of the cavity allowing for dispersive coupling.

1.2 Micro and Nano-Electromechanical Resonators (MEMS/NEMS)

The key parameters used describe a mechanical resonator are its mass m, resonant frequency ω_m, linewidth γ_m and quality factor Q_m. There will be multiple resonant

frequencies but most experiments only make use of the fundamental mode. The quality factor is defined as $Q_m = \omega_m/\gamma_m$ as in the case of the cavity and it gives the ratio of energy stored in the oscillator compared to energy dissipated per radian of oscillation. The larger the quality factor the longer lived the vibrational states. For ease of detection it is desirable that the zero-point motion, defined in equation 1.5, is as large as possible, so that the resonator has a small mass and/or high resonant frequency.

The number of thermal phonons in the membrane at thermal equilibrium is given by

$$n_{eq} = \frac{k_B T}{\hbar \omega_m} \tag{1.7}$$

This equation links the mode temperature of a resonator to its phonon occupation.

The nano-electromechanical device (where thickness is concerned) used throughout this thesis is a nm-thick silicon nitride (SiN) membrane. Silicon nitride membranes have been fabricated to exhibit very high tensile stress, resulting in high quality factors [3–5], and have been used for a number of applications including measurement of radiation pressure shot noise [6], optical squeezing [7], microwave frequency conversion [8], bidirectional conversion between microwave and optical light [9] and the optical detection of radio waves [10, 11] to name just a few. The use of nano-electromechanical and micro-electromechanical resonators (NEMS and MEMS) in general is extensive and the interested reader is directed to Ref. [12] for a review.

1.3 Fundamental Tests of Physics using MEMS and NEMS

As this thesis focuses on fast and sensitive measurements of the position of a nanomechanical resonator for use in tests of fundamental physics I will give a brief background to some of the achievements of the field which include position measurements of MEMS and NEMS.

1.3.1 Cooling to the Ground State

To observe quantum behaviour in mechanical resonators the thermal fluctuations must be smaller than the mechanical excitations. State of the art dilution refrigerators have a base temperature of around 10 mK and this corresponds to an oscillator frequency of around 209 MHz. An experiment of note is Ref. [13] where the ground state was reached and single phonon control was achieved over a 6 GHz piezoelectric resonator coupled to a qubit. Often it is desirable to use lower frequency oscillators as they have a larger zero-point motion, which increases the coupling strength, and therefore cooling techniques must be implemented to remove the thermal phonons in the oscillator. Below I discuss a few different cooling techniques.

Backaction Cooling

If the temperature of the cavity field is lower than the resonator (as tends to be the case due to the higher resonant frequencies of microwave cavities) the backaction force can be used to damp the motion of the resonator and hence cool it down. This process is also known as backaction cooling, self-cooling or passive feedback cooling as the cooling happens 'by itself', one can think of it as the resonator reaching thermal equilibrium with the cavity field. The condition for this to happen is that the coupling between the resonator and the cavity is strong enough so that the damping induced by the backaction is larger than the intrinsic damping of the resonator [12].

Brown *et al.* used this method to cool a 7 kHz cantilever from room temperature to 45 K [14] by coupling it to a driven rf circuit. Fink *et al.* cooled a 4.48 MHz nanobeam to the ground state at millikelvin temperatures [15].

The limitation of passive cooling, besides the strong coupling requirement, is that one can not cool to a lower temperature than the cavity field. For optical frequencies of 100's THz one is deep in the ground state of the optical field even at room temperature however for microwave frequencies in the GHz regime one must be at cryogenic temperatures to be in the ground state of the microwave field.

Sideband Cooling

An alternative way to cool a resonator is via sideband cooling [1, 16, 17]. The regime of interest for sideband cooling is the resolved sideband regime where $\kappa << \omega_m$. The opposite regime where $\kappa > \omega_m$ is known as the unresolved sideband regime or bad cavity limit. The sideband ratio κ/ω_m is used to quantify how far into the resolved sideband regime an experiment is. Intuitively one can think of sideband cooling in the following manner. At the resonant frequency of the cavity the photon density of states is at its highest and therefore so is the probability of photon emission. If the cavity is driven with a detuning equal to $\Delta = \pm\omega_m$ photons arriving in the cavity either can lose or gain energy equal to ω_m in order to leave the cavity at the resonance frequency. Negative detuning of the drive frequency (also known as the red sideband) leads to cooling of the oscillator as the red detuned photons absorb one quanta of mechanical energy to be upconverted to the resonance frequency of the cavity.

Positive detuning of the drive frequency (also known as the blue sideband) leads to heating of the oscillator as the blue detuned photons deposit one quanta of mechanical energy in order to be downconverted to the resonance frequency of the cavity.

The final minimum phonon occupation for a sideband cooled resonator is given by [1]

$$\bar{n}_{min} = \left(\frac{\kappa}{4\Omega_m}\right)^2 \tag{1.8}$$

In the resolved sideband regime ($\kappa << \Omega_m$) and $\bar{n}_{min}$ is less than one, however in the unresolved sideband regime it is larger than one and so the ground state can not be reached. This equation assumes that the cavity field has a negligible thermal occupation.

Sideband cooling was implemented in electromechanical systems [18–20] with the ground state being reached by Teufel *et al.* in 2011 [21]. The setup consisted of a 15 μm 100 nm thick aluminium drum with a resonant frequency of 10.56 MHz. This was embedded into a superconducting microwave circuit with a resonant frequency of $2\pi \times 7.54\ GHz$ and decay rate of 200 kHz. The device was placed in a dilution refrigerator and at 20 mK the thermal occupancy of the oscillator was 40 quanta.

The experiment was deep in the resolved sideband regime with a sideband ratio of around 50. As the drive was increased from 18 to 180,000 photons, thus increasing the coupling strength, the mode temperature (number of phonons) was decreased right down to 0.34 at 89,000 drive photons. When the drive was increased to 180,000 the phonon number increased slightly to 0.42 due to entering the strong coupling regime which allows for the coherent exchange of phonons and photons and so the cavity has a slight heating effect on the resonator.

Sideband cooling has been implemented in a 3D microwave cavity setup with a 1 mm x 1 mm SiN oscillator [22]. The final thermal occupation reached was 5.2 phonons even though they expected to be able to cool to a phonon occupation of 0.2. These extra phonons were attributed to cavity noise. This oscillator had an initial mode temperature of 180 mK which is above the base temperature of the dilution refrigerator and corresponds to 3.06 $\times 10^4$ phonons.

Noguchi *et al.* modified this setup [23] by introducing galvanic connections between the antenna and cavity and reducing the capacitor gap formed between the membrane and antenna. They achieved a single photon coupling strength of 7 Hz and were able to cool to a minimum occupation of 0.51 $\pm$ 0.12 phonons.

Cooling via Noise Interference (Dissipative Coupling)

Sideband cooling only works in the resolved sideband regime, however outside of this regime (in the bad-cavity regime) cooling can be implemented in a system with dissipative coupling (where the mechanical motion modulates the damping rate κ of the cavity) by making use of noise interference effects. In fact when the interference is destructive the cavity effectively acts as a zero-temperature bath independent of the ratio of κ/ω_m [2].

Dissipative coupling was verified for the first time in an optical system where a SiN membrane was cooled to an effective temperature of 126 mk from room temperature [24].

The implementation of dissipative cooling in the microwave regime has been discussed [25] but it has yet to be carried out. Figure 1.2 shows how a microwave setup

to implement dissipative coupling is different from one implementing dispersive coupling. (Note that dispersive coupling will be present in the dissipative case as well)

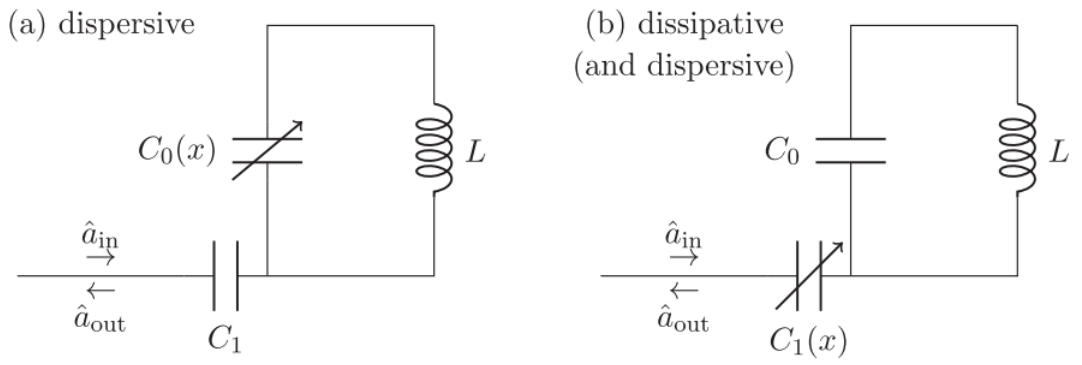


Figure 1.2: Electromechanical implementation of dispersively and dissipatively coupled systems. From Ref. [25]

1.3.2 The Creation of Massive Superpositions

It has been proposed that if one can map the quantum state of a qubit onto a mechanical resonator then one can create a massive superposition [26, 27], and the experiment mentioned earlier with the 6 GHz mechanical resonator went some way towards that goal achieving single phonon control [13]. However, instead of using a qubit one can also use a single photon to produce a superposition in a mechanical resonator [28]. The experiment consists of a Michelson interferometer with a cavity in either arm, as depicted in Fig. 1.4. In one of the cavities one of the mirrors is free to move (constituting the mechanical resonator), and for strong enough single photon coupling the radiation pressure of a single photon will displace it. If the single photon is in a superposition of being in both arms of the cavity it follows that the mirror is in a superposition of its normal and its displaced position. Although conceptually this idea is beautifully simple, in practice the experimental requirements are extremely stringent as one requires that $g_0 > \omega_m >> \kappa$. This idea has been further developed for use in the optical regime and the interested reader is referred to [29–33].

An alternative way to create a superposition even if $g_0/\omega_m << 1$ was proposed by Liao *et al.* [34, 35]. It involves coupling a single mechanical oscillator to two

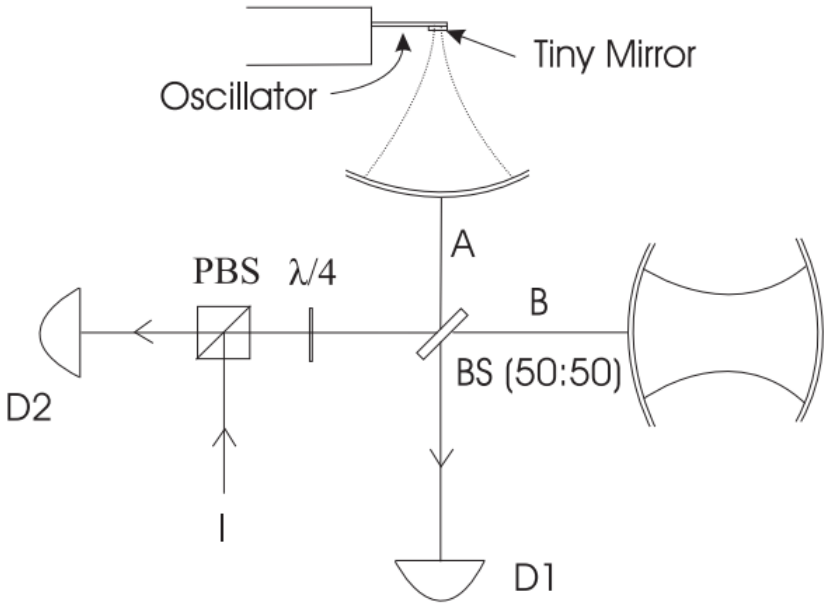


Figure 1.3: Proposed setup for creating a massive superposition in an optomechcanical setup: a Michelson interferometer for a single photon with a cavity in each arm A and B. The one end of the cavity in arm A is free to move forming a mechanical resonator. The single photon enters through I and is detected at detectors D1 or D2. PBS = polarising beam splitter. BS = beam splitter. From Ref. [28].

cavities using a 'membrane-in-the-middle' configuration. Their setup allows for photon tunnelling between the two cavities through the membrane. A frequency modulation is introduced to modulate the frequencies of the two cavities in addition to the modulation induced by the membrane and under the right conditions the photon tunnelling interaction allows a single photon to displace the membrane to form a superposition even when not in the single photon strong coupling regime.

This idea could be implemented in the microwave regime with a metallized resonator forming a capacitor replacing the semitransparent membrane [36, 37].

Should the creation of superpositions of macroscopically distinct states be possible the natural question to ask oneself is what is the size limit to these superpositions? As perhaps the biggest open question in modern physics is the relationship between quantum mechanics and general relativity, does gravity set the ultimate bound on the borders of the quantum realm? In foundations of quantum mechanics communities there is no consensus about the concept of a limit to the quantum realm; since many interpretation of quantum mechanics suffer from being

untestable experimentally, it is rather difficult to agree on the matter. There is however one interpretation which, with technological advancement, is testable. The broad name for this interpretation is Continuous Spontaneous Localization (CSL) and theories based on this interpretation as sometimes referred to as collapse models.

1.3.3 Testing of Collapse Theories

Collapse models are testable as due to spontaneous collapse of the wave function they violate energy conservation [38–40]. These models predict that although to us quantum mechanics seems entirely random, below the surface so to speak, there are events, called flashes or hittings, which determine the outcome of experimental runs and restore determinism to quantum mechanics. Any measuring apparatus entangles itself with the quantum system under scrutiny and as a result the mass of the entire system is now very large. Quantum superpositions of large mass scales can only survive for a minuscule amount of time as they are subject to more hittings, and this accounts for why we never observe quantum superpositions of large objects. In addition the time the superposition can exist for scales inversely with the length scale separating the two states so the probability of the existence of macroscopic superpositions is suppressed as the size increases.

The two key parameters in the theory are the collapse rate λ which gives the frequency of the hittings or the flashes and the localisation distance r_C which characterises the spatial resolution of the spontaneous collapse. If this theory is correct these constants acquire the status of new constants of nature. The standard values suggested for these constants are $\lambda \approx 10^{-17}$ s$^{-1}, r_C = 10^{-7}$ m although Adler has suggested less conservative values of $\lambda_{Adler} = 10^{9\pm2}\lambda$ for $r_c = 10^{-7}$m and $\lambda_{Adler} = 10^{11\pm2}\lambda$ for $r_c = 10^{-6}$m [41].

It was proposed in several publications that the heating effect of sponatneous wave function collapse models would imply a change in equilibrium temperature of a mechanical oscillator [42–44]. That is to say that the experimental signature of CSL is a slight temperature-independent violation of the equipartition theorem due to wavefunction collapse. This excess energy can be expressed as a temperature

increase which depends on the geometry of the system, with the increase being maximised for the highest possible mass density and quality factor and lowest possible resonant frequency [45, 46]. Viante *et al.* used a 100 μm cantilever with a ferromagnetic microsphere attached at one end to enable detection of the motion using a superconducting quantum interference device (SQUID). Their measurements of the thermal fluctuations of the cantilever reveal a nonthermal force noise of unknown origin, which is compatible with the CSL heating predicted by Adler. Whilst several physical mechanisms able to explain the observed noise have been ruled out they conclude that further tests need to be carried out with a different setup or in a different lab [45, 46].

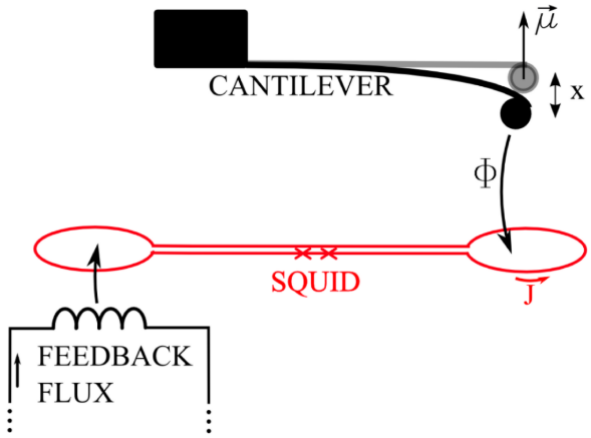


Figure 1.4: The simplified measurement setup of Ref. [46]. The motion of a cantilever with a ferromagnetic microsphere is monitored using a SQUID. Figure taken from Ref. [46].

Straying slightly away from optomechanics with mechanical resonators it has been proposed that CSL could also be tested by examining the parametric heating rate of a trapped nanosphere [47]. Using a Paul trap to levitate the particle and optical cooling it should be possible to reduce environmental decoherence to a level where CSL dominates the dynamics and is the main source of heating [48]. Another proposal states that the tiny energy-momentum violation predicted by CSL also implies that the stochastic kicks experienced by an isolated object will induce a random walk [49].

Going back to nanoscale optomechanics a more involved proposal combines phonon counting with mitigation of technical noise including non-linear photon

conversion and photon coincidence counting. The authors state that their system would be able to resolve the small phonon fluxed required to test collapse models and that it also may be able to identify their physical origin [50].

A key candidate for the source of the CSL flashes is gravity, as there is still much to be understood about the merging of quantum mechanics and general relativity. The jury is still out as to whether gravity is quantum or classical. A proposal by Kafri, Taylor and Milburn [51] models gravity as a classical channel. Testing this theory is one of the main aims of this thesis and it is discussed in more detail and tested in chapter 6.

1.3.4 Other Achievements

Detecting the Casimir Effect

Quantum mechanics also predicts that the vacuum field should have a zero-point energy analogous to the zero-point motion of a mechanical oscillator. It is predicted to lead to two effects — the (static) Casimir effect which is the force in a vacuum produced by the quantum fluctuations of the vacuum energy and also the dynamical Casimir effect which occurs if a mirror is accelerating fast enough in a vacuum. The dynamical Casimir effect can be thought of as amplifying the vacuum fluctuations/creating real photons from the virtual vacuum ones depending on your preferred interpretation of virtual processes. The static Casimir effect has been detected numerous times e.g. [52, 53] and there is some discussion as to whether or not this confirms the existence of vacuum fluctuations or simply fluctuations of the conductors used in the experiment [54, 55]. The dynamical Casimir effect has been detected using microwave cavities [56–58].

In addition to the static and dynamical Casimir effects which arise due from the vacuum of the electromagnetic field, there is a prediction that in theory, if gravity is quantized, there should also be a Casimir effect due to the gravitational field [59]. (Of course if gravity is not quantized, which is one of the claims of the theory of classical channel gravity discussed in chapter 6, then this effect would not arise.) An experiment designed to detect this effect between two superconducting nanobeams

was performed [60]. Although the effect was not observed, this could have been due the geometry of the system, the calculations done for two plates might have overestimated the effect. The authors mention however that the overestimation for the static Casimir force is one order of magnitude too large when calculated for plates compared with simulations done for a similar device [61], whereas the gravitational Casimir effect would need to be two orders of magnitude smaller than the prediction for two plates for it not to be observable in their setup

Squeezing

In the quantum realm the uncertainty principle must be obeyed which leads to a standard quantum limit of measurement precision [62], however the standard quantum limit can be surpassed by''squeezing' one quadrature so that its imprecision is reduced with the variance in the complementary quadrature becoming larger.

Squeezing was predicted to be possible in laser light [63] and observed two years later [64]. Blencowe and Wybourne [65] proposed its implementation in mechanical oscillators. This idea was further developed [66, 67] and was implemented by Pirkkalainen *et al.* in a 15 μm drum resonator [68]. They obtained squeezing of one quadrature amplitude 1.1 $\pm$ 0.4 dB below the standard quantum limit. As squeezing is an inherently quantum property one could take this as verification of the quantum nature of motion in a micromechanical device.

Single quadrature measurements of a mechanical oscillator were carried out by Lecocq *et al.* by coupling a micromechanical resonator to two microwave cavities [69] which allowed for measurements of a single quadrature and thus avoided the measurement backaction limit by more than 13 dB.

Entangling Two Mechanical Resonators

Entanglement is a key feature of the quanutm realm and it has only recently been shown that it is possible to experimentally entangle two mechanical oscillators [70]. The experiment consisted of two micromechanical aluminium drums separated by 600 μm, both coupled to a microwave cavity.

As this brief introduction has shown, there are many exciting tests of fundamental physics which can be carried out using optomechanical systems. Knowledge of the system parameters in an essential part of constructing an experiment to test foundational questions, and the next chapter will introduce a system which amongst other things is capable of characterising an optomechanical setup incorporating a silicon nitride membrane ready to be used in foundational experiments.

2

Radio Frequency Probing of Mechanical Motion

Contents

2.1 Device Fabrication 18
2.2 The Circuit (Cavity) 18
2.3 Coupling to the Cavity 22
2.4 Direct Driving of the Membrane 23
2.5 Driving the Membrane with White Noise 24
2.5.1 Mechanical Quality Factors 27
2.5.2 Extraction of g_0 from Mechanical Sidebands 28
2.6 Optomechanically Induced Transparency 30
2.7 Time Domain Measurements 33

(This chapter is also presented in publication format in Ref [71].)

Radio frequency (rf) circuits allow for sensitive mechanical readout on-chip [10, 14, 72–74]. In this chapter I characterize a silicon nitride membrane at room temperature making use of an off-resonant rf cavity. In this approach, the use of lumped elements greatly simplifies the detection circuit in terms of fabrication and allows the integration on chip with the mechanical oscillator. The circuit has a lower, and thus more convenient, operation frequency than microwave cavities [72, 74], and allows for a larger readout bandwidth than previous works [14]. Also,

this cavity allows me to inject noise, effectively increasing the mechanical mode temperature. I am able to detect several modes and extract the quality factor and cavity coupling strength for each of them. When the membrane is driven, I am able to resolve the membrane's motion in real time. I observe optomechanically induced transparency (OMIT) and optomechanically induced absorption (OMIA) on-chip and deep in the unresolved sideband regime, allowing for the characterisation of the membrane's motion under radiation pressure.

2.1 Device Fabrication

The device, shown in Fig. 2.1, consists of a 50 nm thick, high-stress, 1.5 mm×1.5 mm silicon nitride membrane with 90% of its area metallized with 20 nm of aluminium (Al) in order to form one plate of a capacitor. The membrane is purchased commercially (in a custom made order) from *Norcada*. The membrane is suspended in a 5 mm×5 mm, 200μm thick, high resistivity (>3500Ω cm) silicon frame. The base chip consists of two chrome/gold (Cr/Au) electrodes (approx 10/110 nm) patterned on a silicon chip using shadow mask evaporation. Two 10/90 nm, 3 mm long Cr/Au pillars are evaporated on either electrode to support the membrane in order to suspend it. The membrane is placed upside down (metallized membrane side towards the electrodes) on top of the pillars and secured with a drop of epoxy. One of the electrodes is grounded and the other is connected to a lumped element radio frequency (rf) tank circuit using a wire bonder.

2.2 The Circuit (Cavity)

A schematic of the electromechanical setup is shown in Fig. 2.2. The rf circuit acts as a cavity. It consists of an on-chip inductor L and capacitors C_{D} and C_{M} mounted on the sample holder, in addition to the capacitance formed by the membrane C_{C}. The circuit behaves as an LC resonator with total capacitance $C_{\mathrm{T}} = C_{\mathrm{C}} + C_{\mathrm{P}}$, where C_{P} accounts for the capacitance between the two sides of the antenna and other parasitic capacitances. Parasitic capacitances contribute to C_{M}. The role of

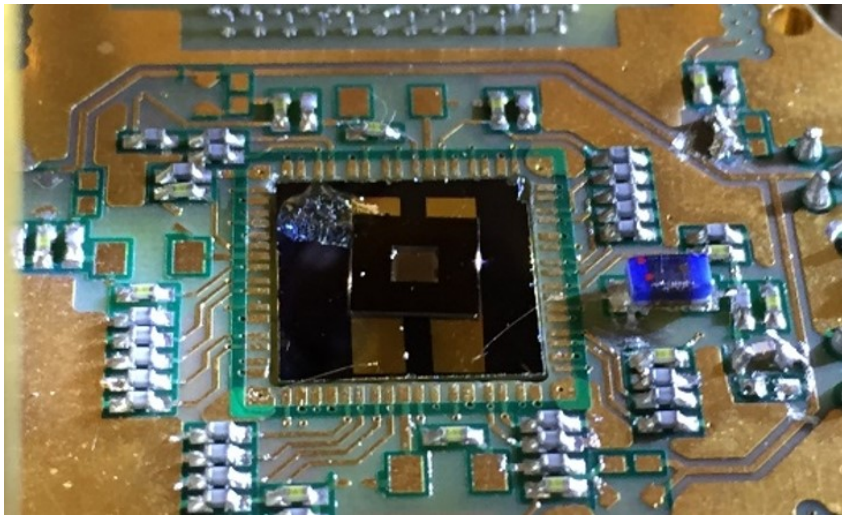


Figure 2.1: Photo of the device which consists of a 1.5 mm square silicon nitride membrane in a 5 mm silicon frame suspended over Cr/Au electrodes on a 1cm square silicon chip. One electrode is grounded and one is connected to an rf tank circuit.

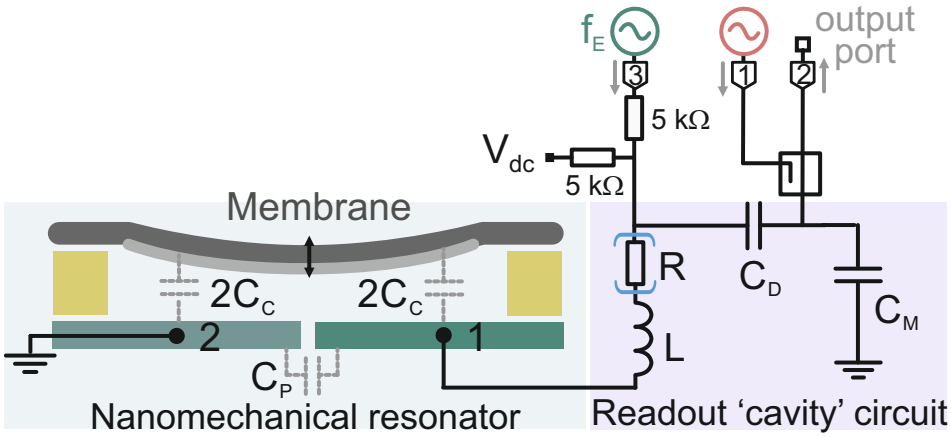


Figure 2.2: Schematic of the electromechanical device consisting of a metallized silicon nitride membrane suspended over two metal electrodes. Electrode 2 is grounded and electrode 1 is connected to an rf tank circuit acting as a readout cavity. The cavity is formed from an inductor $L = 223$ nH and 10 pF fixed capacitors C_{D} and C_{M}. Parasitic losses in the circuit are parametrized by an effective resistance R. To probe the cavity an rf signal is injected at port 1, passed via a directional coupler, and after reflection received at port 2. The membrane's motion is excited via port 3. Bias resistors allow a dc voltage V_{dc} to be added to the membrane drive signal.

C_{M} is to improve on the impedance matching between the circuit and the 50 Ω line. C_{D} controls the coupling to the cavity, i.e. the number of photons entering the cavity. Because these capacitors are larger than C_{T} , they do not strongly affect the cavity frequency. This cavity can be driven by injecting a rf signal to

the input (port 1) via a directional coupler and port 3 allows injection of an ac signal to excite the membrane's motion. A dc voltage $V_{\rm dc} = 15$ V is applied to electrode 1, with electrode 2 grounded. The entire setup forms a three-terminal circuit with input ports 1 and 3 and output port 2 (Fig.2.2).

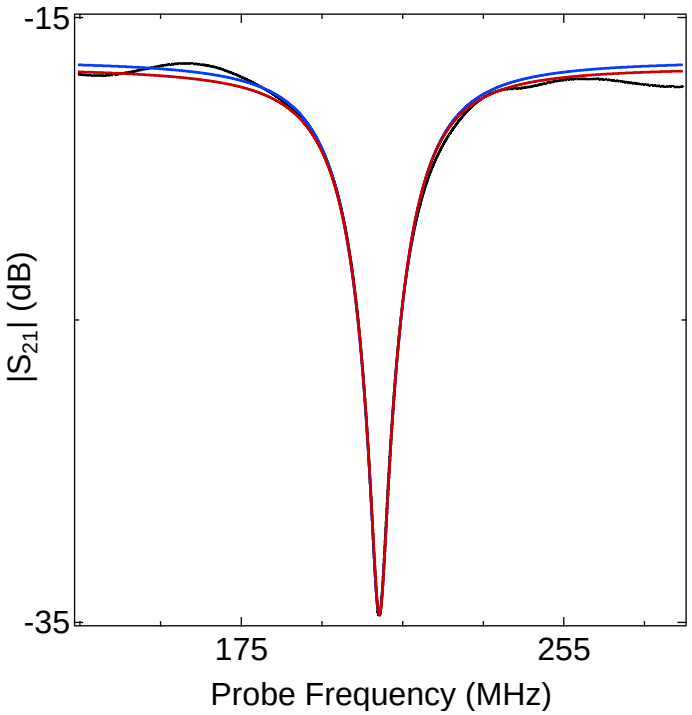


Figure 2.3: $|S_{21}|$ as a function of cavity probe frequency. Black is the data, blue is a fit to Eq. 2.1 and red is a fit to the circuit model.

A vector network analyser can be used to measure the cavity reflection, $|S_{21}|$, as a function of cavity probe frequency, shown in Fig. 2.3. The cavity resonance is evident in reflection as a minimum in the cavity reflection with quality factor $Q_{\rm E} \approx 7.4$. The reflection is fit (shown in blue in Fig. 2.3) using

$$S_{21}(f_{\rm P}) = \alpha e^{i\phi} + (1-\alpha)(1 - \frac{\kappa_e}{-2\pi i(f_{\rm P} - f_{\rm C}) + \kappa/2}) \tag{2.1}$$

where α is the isolation of the directional coupler (ZEDC-15-2B) and ϕ a phase [75]. $f_{\rm C}$ is the cavity resonance frequency, κ_e is the external dissipation rate and κ the total dissipation rate of the cavity. From a fit with a fixed value of $\alpha = 0.001$ from the directional coupler data sheet and correcting for an insertion loss of -16.4 dB from the

leads and directional coupler, the values $\phi = (0.9\pm0.1)\pi$ rad, $f_{\rm C} = 209.23\pm0.01$ MHz, $\kappa/(2\pi) = 28.20\pm0.01$ MHz and $\kappa_e/(2\pi) = 15.80\pm0.01$ MHz are extracted (Fig. 2.3).

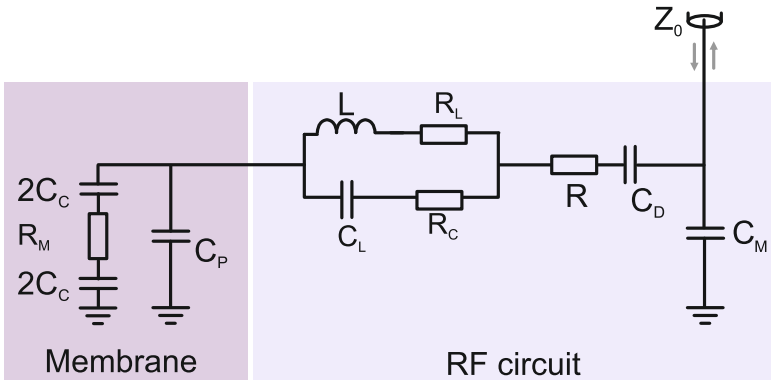


Figure 2.4: Circuit model. Capacitors $C_{\rm M}$ and $C_{\rm D}$ are taken as simple lumped elements, including any parasitic capacitances in parallel. Elements $R_{\rm L}$, $R_{\rm C}$ and $C_{\rm L}$ model parasitic contributions to the impedance of the inductor L. The effective resistance R models other losses in the circuit. The membrane is modelled by the combination of $R_{\rm M}$ and $C_{\rm C}$, the capacitance between the metallized area of the membrane and both antenna electrodes. To each electrode, the membrane-electrode capacitance is $2C_{\rm C}$, which when summed together in series gives $C_{\rm C}$.

The cavity response can also be fit using the circuit model in Fig. 2.4 (shown in red in Fig. 2.3) in order to extract circuit parameters. The capacitors $C_{\rm D}$ and $C_{\rm M}$ are taken as simple lumped elements. The capacitor formed between the electrodes and the metallized membrane, $C_{\rm C}$, formed by two electrode-membrane capacitors of value $2C_{\rm C}$, as well as the capacitance between antenna electrodes and other parasitics, $\rm C_P$, are considered. The inductor is modelled as a network of elements as shown, which simulates its self-resonances and losses. The membrane has a resistance R_M and other losses in the circuit are modelled by an effective resistance R.

The reflection coefficient Γ is equal to

$$\Gamma(f_{\rm P}) = \frac{Z_{\rm tot}(f_{\rm P}) - Z_0}{Z_{\rm tot}(f_{\rm P}) + Z_0}, \tag{2.2}$$

where $Z_{\rm tot}$ is the total impedance from the circuit's input port and $Z_0 = 50\ \Omega$ is the line impedance. The measured transmission S_{21} is related to Γ by assuming a constant overall insertion loss A, incorporating attenuation in the lines and the coupling of the directional coupler, such that

$$|S_{21}(f_{\rm P})| = A|\Gamma(f_{\rm P})|. \tag{2.3}$$

The data shown in Fig.2.3 is fit with parameter $C_{\mathrm{D}} = 10$ pF from the known component value, $L = 223$ nH, $R_{\mathrm{L}} = 3.15 \times 10^{-4}\ \Omega \times \sqrt{f_{\mathrm{P}}\ [\mathrm{Hz}]}$, $\mathrm{R_C} = 25\ \Omega$ and $\mathrm{C_L} = 0.082$ pF from the datasheet of the inductor. For the resistance of the aluminium film $R_{\mathrm{M}} = 7.5\ \Omega$ is estimated using the resistivity of aluminium (15 $\mu\Omega$ cm) and the known film thickness (20 nm) [76]. A COMSOL model of the antenna electrodes gives an estimate of a capacitance of 1.4 pF and a parasitic capacitance of 0.7 pF is added based on previous work [77] making a total parasitic capacitance C_{P} of 2.1 pF. The fit parameters are then A, C_{M}, R, and C_{C}. From the fit $A = -16.657 \pm 0.001$ dB, $C_{\mathrm{M}} = 20.93 \pm 0.01$ pF, $R = 15.87 \pm 0.01\ \Omega$ and $C_{\mathrm{C}} = 1.6432 \pm 0.0001$ pF are obtained.

2.3 Coupling to the Cavity

A coupling between the motion of the membrane and the cavity is formed due to the dependence of the capacitor formed between the electrodes and the metallized membrane C_{C} on the mechanical displacement u. This coupling is given by $\frac{df_{\mathrm{C}}}{du} = \frac{\partial f_{\mathrm{C}}}{\partial C_{\mathrm{T}}}\frac{\partial C_{\mathrm{C}}}{\partial u}$ and $\frac{\partial f_{\mathrm{C}}}{\partial C_{\mathrm{T}}} \approx 1/(4\pi\sqrt{LC_{\mathrm{T}}^3})$ where f_{C} is the cavity resonance frequency, C_{T} the total circuit capacitance and u the membrane's displacement from its equilibrium position. Therefore $\frac{df_{\mathrm{C}}}{du} \approx 1/(4\pi\sqrt{LC_{\mathrm{T}}^3})\frac{\partial C_{\mathrm{C}}}{\partial u}$. The coupling causes shifts in the phase and amplitude of the cavity reflection, allowing the membrane's motion to be monitored in the unresolved sideband limit. The single-photon coupling strength (as discussed in chapter 1), which measures the interaction between a single photon and a single phonon, is

$$\frac{g_0}{2\pi} \approx \frac{1}{4\pi\sqrt{LC_{\mathrm{T}}^3}}\frac{\partial C_{\mathrm{C}}}{\partial u}u_{\mathrm{ZPM}} \tag{2.4}$$

where u_{ZPM} is the amplitude of the membrane's zero-point motion.

Within the parallel plate capacitor approximation, $C_{\mathrm{C}} \sim \frac{\epsilon_0 a}{d}$, where ϵ_0 is the vacuum permittivity, a is the metallised area of the membrane and d is the membrane-electrode gap. From the circuit model $C_{\mathrm{C}} \approx 1.6$ pF and therefore $d \sim 9\ \mu$m. g_0 is extracted further on in this chapter.

2.4 Direct Driving of the Membrane

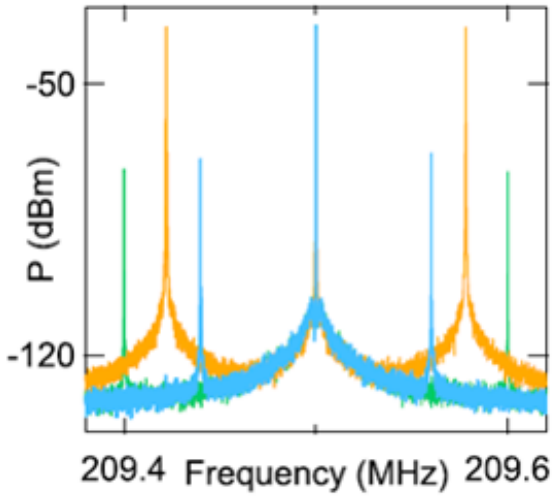


Figure 2.5: Power spectrum of the signal at port 2 showing the peak at the cavity resonance frequency, from the cavity drive applied via port 1, and sidebands corresponding to a frequency modulated tone applied via port 3. The light blue and light green curves correspond to the power spectrum for an excitation f_{E} below (60 kHz) and above (100 kHz) f_0 respectively. Sidebands appear due to non-linearities in the circuit. The orange curve corresponds to $f_{\mathrm{E}} \sim f_0$. In this case, the sidebands are larger.

In order to find the mechanical resonances of the membrane, predicted to be in the kHz regime from considerations of the geometry and tensile stress of the membrane [12] and as reported in Refs. [22, 23], the cavity is driven on resonance ($f_{\mathrm{C}} \approx 209.5$ MHz) through port 1 and a kHz frequency tone f_{E} is swept through port 3. f_{E} is frequency modulated in a white noise pattern with a deviation of 200 Hz. Figure 2.5 shows three measurements taken when the cavity is driven on resonance with input power $P_{\mathrm{C}} = 5$ dBm at port 1 whilst a sinusoidal signal at frequency f_{E}= 60 kHz (light blue), 100 kHz (light green) and $\approx$ 77.9 kHz (orange), is applied to port 3 with amplitude $\mathrm{V_{WN}}$=3.6 $\mathrm{V_{rms}}$ at electrode 1. The sidebands appear due to non-linearities in the circuit, giving rise to frequency mixing, as seen in the light blue and green traces. This signal is increased in the orange trace indicating a mechanical resonance.

It is clearer to see the mechanical signals in Fig. 2.6 which shows the higher frequency sideband of the drive signal at $f_{\mathrm{C}} + f_{\mathrm{E}}$ whilst f_{E} is swept from 27 to 210 kHz. The fundamental mode frequency $f_{1,1}$, which so far I have referred to

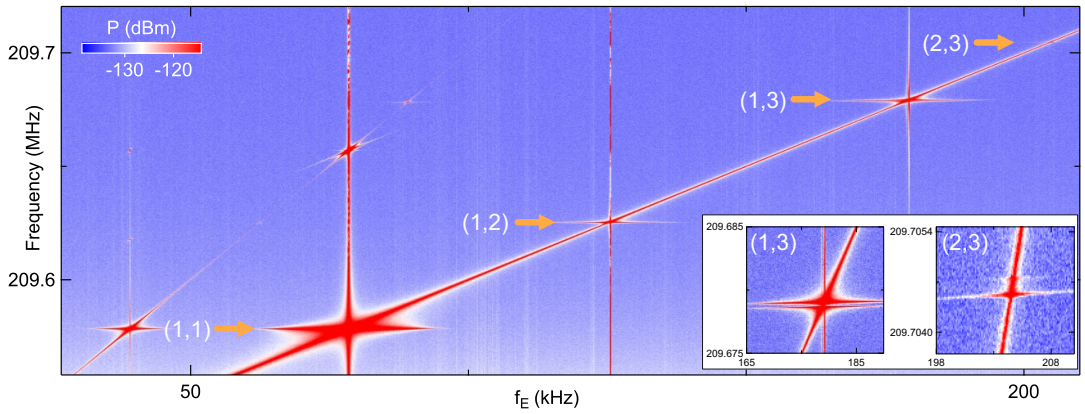


Figure 2.6: Higher frequency sidebands in Fig. 2.5 as a function of f_{E}. When f_{E} is close to a mechanical mode of the membrane, a mechanical sideband appears. The four visible mechanical modes are indicated with arrows. Because higher modes produce fainter features, they are not displayed in this graph. Note that the colour scale displays a range of only 25 dBm in order to reveal the weaker features. Insets: zoom-in of the two highest frequency modes displayed. A splitting of the mechanical feature is visible, indicating nearly degenerate modes.

as f_0, is ~ 77.9 kHz, giving an unresolved sideband ratio of $2\pi f_0/\kappa \sim 3 \times 10^{-3}$, where $\kappa = 2\pi f_{\mathrm{C}}/Q_{\mathrm{E}}$ is the cavity linewidth. As well as the fundamental mode, one can see less strong harmonics $f_{i,j}$ near the expected frequencies. The expected frequencies for higher harmonics theoretically satisfy the ratios $f_{i,j}/f_0 = \frac{1}{\sqrt{2}}\sqrt{i^2+j^2}$ for integers i and j with symmetric roles as expected for a square membrane. Two of the sidebands are double peaked, evidencing nearly degenerate mechanical modes. The broken degeneracy could be due to imperfections in how the membrane was fabricated and fixed in place or uneven binding/deposition of the Al layer.

2.5 Driving the Membrane with White Noise

An alternative way to find the mechanical resonances of the membrane in a single measured power spectrum is to drive the cavity at f_{C} whilst injecting white noise via port 3. White noise excites the motion of the membrane at all frequencies, which is equivalent to raising the effective mechanical temperature. In this way, the root mean square (rms) displacement is increased, thereby facilitating the detection of mechanical modes. Figure 2.7 shows the power spectrum measured

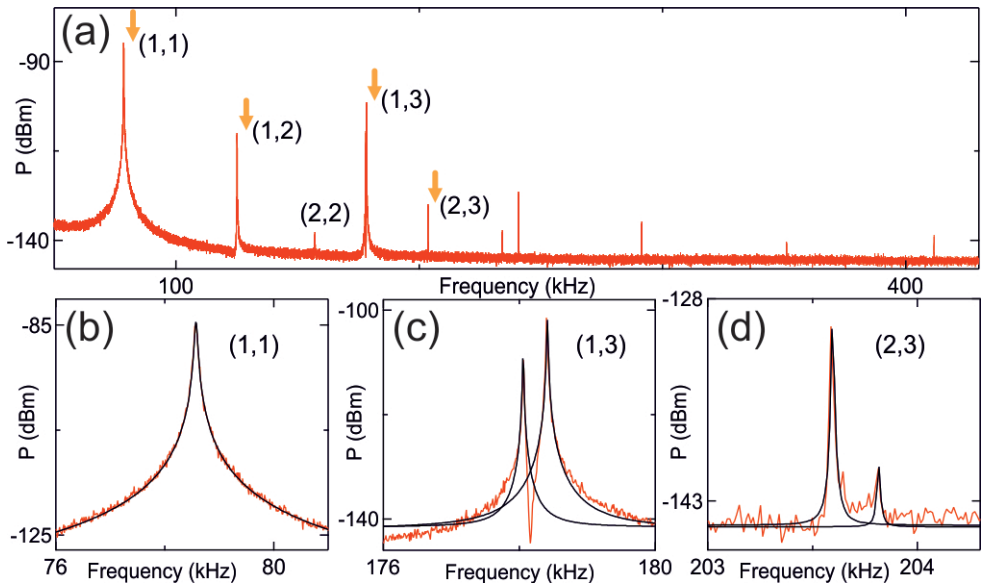


Figure 2.7: Power spectrum as a function of frequency. A tone at f_C is applied with input power $P_C = 5$ dBm and white noise is injected via port 3 at V_{WN} =2.7 V_{rms} at electrode 1. Several mechanical modes are visible. The four mechanical modes visible in Fig. 2.6 are indicated with arrows. The mode at $\sim$ 157 kHz, labelled (2,2), is not visible in Fig. 2.6 due to a higher noise floor than in this figure, which arises from a higher resolution bandwidth. Higher modes are not labelled because the deviation from theoretical ratios makes their identification ambiguous. (b-d) Zoom in showing the fundamental mode, and selected nearly degenerate modes. The black curves are Lorentzian fits.

when the cavity is driven at f_C with input power $P_C = 5$ dBm and a white noise signal with a bandwidth of 1 MHz (larger than the spectral width of the mechanical modes) and an amplitude $V_{WN} = 2.7$ V_{rms} is applied via port 3. The fundamental mode of the membrane is at $f_0 = 78.573 \pm 0.002$ kHz. Each mechanical sideband is fitted with a Lorentzian (Figs. 2.7(b-d)). As in Fig. 2.6, double peaked sidebands are visible in (Figs. 2.7(c,d)).

The ratios $f_{i,j}$ $/f_0$ are plotted as a function of $f_{i,j}$ in Fig. 2.8 for all mechanical resonances observed in Figs. 2.6 and 2.7. Lower frequency modes show better agreement with theoretical ratios than higher frequency modes.

In order to distinguish the mechanical sidebands in Fig. 2.7 from parasitic resonances they are measured as a function of P_C (Fig. 2.9). The frequency of the mechanical modes decreases for the highest values of P_C. This might have to do with heating of the membrane surface and thereby a decrease in its tension. From the circuit model one can calculate the power dissipated in the membrane. For

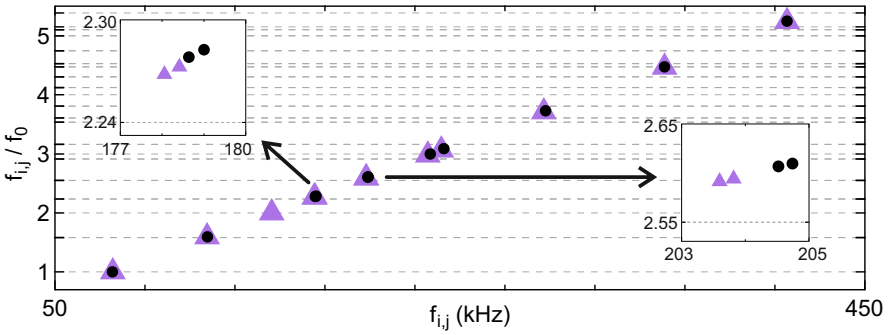


Figure 2.8: Frequency ratios of the mechanical resonances extracted from Fig. 2.6 (circles) and Fig. 2.7 (triangles). Grid lines indicate theoretical ratios. Errors in frequency and frequency ratios are smaller than symbols. Insets: zoom-in showing selected nearly degenerate modes.

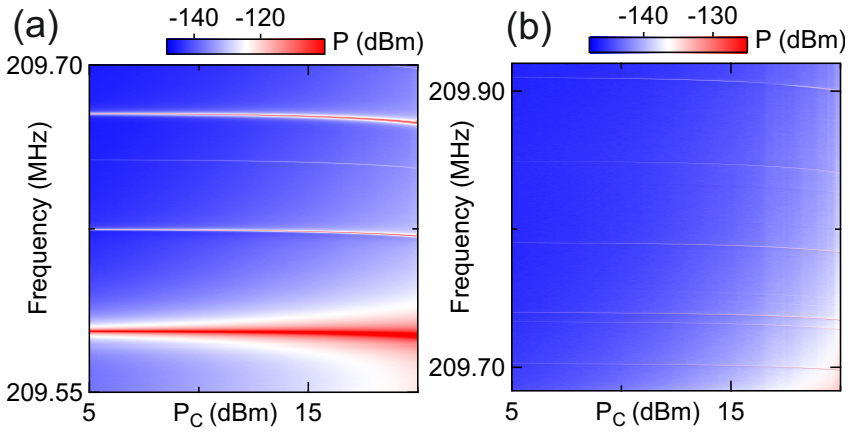


Figure 2.9: Power spectrum as a function of frequency and P_{C} for $V_{\mathrm{WN}} = 2.7\ \mathrm{V_{rms}}$. The cavity drive is at 209.5 MHz. Several mechanical sidebands can be observed. The first few mechanical modes are displayed in (a) and the higher frequency mechanical modes are displayed in (b). As P_{C} increases, the mechanical sidebands are brighter and their frequency shifts to lower values for $P_{\mathrm{C}} \gtrsim 15$ dBm.

$P_{\mathrm{C}} = 15$ dBm, the power dissipated is $\sim 4\ \mu$W. The maximum temperature increase is estimated by assuming that all the dissipated power is emitted as thermal radiation. Taking the emissivity of aluminium as 0.09 and applying the Stefan-Boltzmann law leads to an estimated temperature increase of 4.5 K. For $P_{\mathrm{C}} = 20$ dBm, the temperature difference is ~ 13.5 K. A similar calculation confirms that the injected noise does not change the temperature of the membrane significantly.

2.5.1 Mechanical Quality Factors

The quality factors $Q_{\mathrm{i,j}}$ of the modes $f_{i,j}$ (shown in Fig. 2.10) can be extracted from the Lorentzian fits of Fig. 2.7. These values of $Q_{\mathrm{i,j}}$, measured in the spectral response, are sensitive both to dissipation and dephasing [78]. The fundamental mode has a quality factor $Q_0 = (1.6 \pm 0.1) \times 10^3$ and the highest quality factor measured is $(20 \pm 4) \times 10^3$ for the mode at 241 kHz. Different modes and even nearly degenerate mechanical modes have significant differences in their values of $Q_{\mathrm{i,j}}$, as previously reported [3, 79]. As observed in Ref. [79] a higher mode can exhibit a larger quality factor than the fundamental mode. Interestingly, at cryogenic temperatures the device tested in Ref. [3] had a higher quality factor in the fundamental mode than in the (1,2) mode. The quality factors of this membrane at room temperature are lower than those (of order 10^6 at room temperature) reported in [79]. In fact, quality factors of up to 10^8 have been achieved at room temperature by engineering the design of the membrane[4, 5]. The lower quality factor of this membrane could be due to the large drop of epoxy affixing the membrane to the base chip.

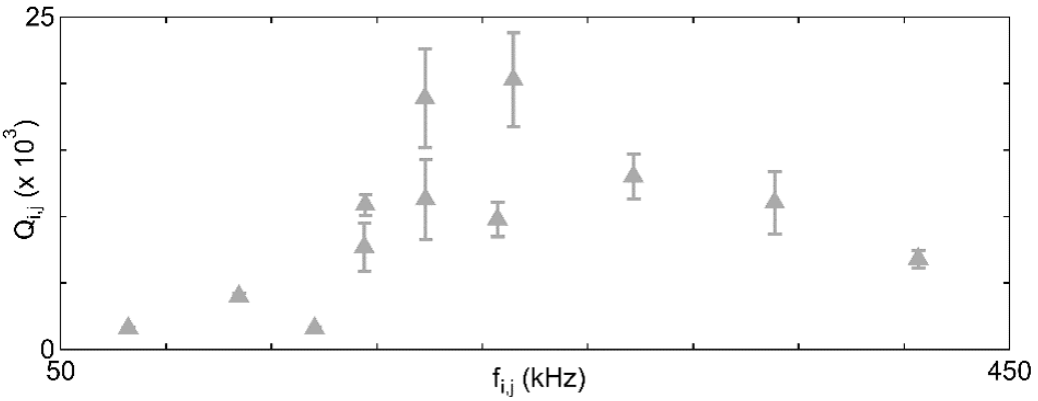


Figure 2.10: Quality factors for each mechanical mode as calculated from Fig. 2.7.

Figure 2.11 shows $Q_{\mathrm{i,j}}$ for different values of $\mathrm{V_{WN}}$. At low $\mathrm{V_{WN}}$, the mechanical sidebands became fainter, and some modes could not be reliably fitted. The values of $Q_{\mathrm{i,j}}$ do not show a trend as a function of $\mathrm{V_{WN}}$, however the larger the values of $Q_{\mathrm{i,j}}$ the larger their variation in values. The better quality factors were found in higher modes which tend to have a lower coupling (see Fig 2.12). The lower

coupling gives rise to a worse signal to noise ratio and makes it more difficult to extract the quality factors, and gives a larger variation in extracted values.

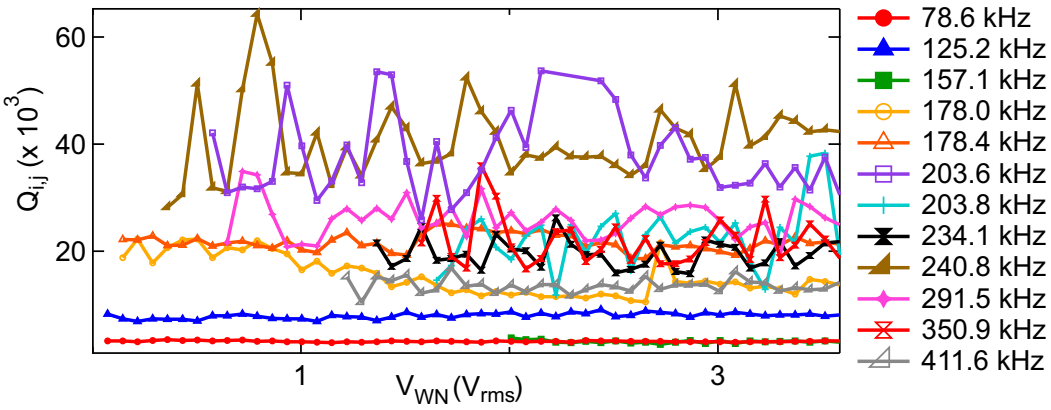


Figure 2.11: Extracted $Q_{\mathrm{i,j}}$ as a function of $\mathrm{V_{WN}}$ for each mechanical mode observed.

2.5.2 Extraction of g_0 from Mechanical Sidebands

From the area below the sidebands in Fig. 2.7 the values of g_0 can be extracted (see appendix A). The values of g_0 are shown as blue squares in Fig. 2.12. For the first mechanical mode $g_0/2\pi = 1.9 \pm 0.1$ mHz. The cavity drive was 5 dBm at port 1, yielding a multiphoton coupling strength $g/2\pi = \sqrt{n_C} g_0/2\pi \sim 4.4$ kHz, where n_C is the mean cavity photon number. As expected, the first mode couples more strongly than higher frequency modes, due to its mode profile and larger zero point motion.

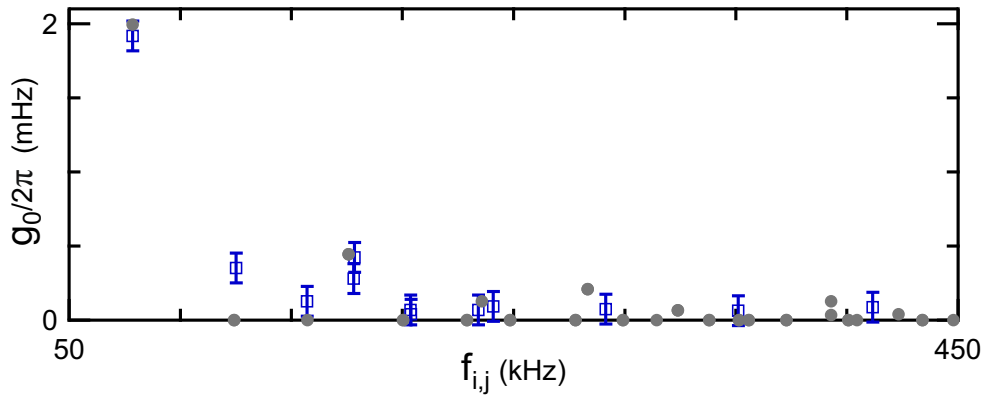


Figure 2.12: Extracted (blue squares) and theoretical (grey circles) values of g_0.

These values of g_0 can be compared with the predictions of Eq. 2.4 (shown in grey circles in Fig. 2.12). Taking C_T and d from the circuit model, and using $\frac{\partial C_\mathrm{C}}{\partial u} \sim \frac{\epsilon_0 a}{d^2}$ for a parallel-plate capacitor (with a prefactor to account for the mechanical mode profile of the membrane), gives a coupling strength $g_0/2\pi \approx 2$ mHz for the fundamental mode. The mode profile modifies $\frac{\partial C_\mathrm{C}}{\partial u}$ and thus g_0. For modes with $i \times j$ even, the sections of the membrane moving away from the antenna and the sections moving towards the antenna are equal, and therefore the net $\frac{\partial C_\mathrm{C}}{\partial u}$ is close to zero, and $g_0 \sim 0$. For $i \times j$ odd, there is always a section of the membrane which does not have a counterpart moving out of phase. Therefore, for odd mode profiles $\frac{\partial C_\mathrm{C}}{\partial u}$, and thus g_0, are reduced by a factor $1/(i \times j)$. The estimated values of g_0 are similar to the ones extracted from the sideband powers.

Taken from the theoretical derivation of g_0 in appendix A the equation

$$[\delta u^2_{\mathrm{i,j}}]_\mathrm{rms} = V^2_\mathrm{dc} \left(\frac{\partial C_\mathrm{C}}{\partial u}\right)^2 \left(\int_0^\infty df |\chi_{\mathrm{i,j}}(f)|^2\right) \frac{S^2_V}{2}, \tag{2.5}$$

can be used to calculate the rms displacement $[\delta u_{\mathrm{i,j}}]_\mathrm{rms}$ corresponding to the mechanical sidebands in Fig. 2.7. For the fundamental mode, $[\delta u_0]_\mathrm{rms} \sim 14$ nm (Fig. 2.13). For comparison, for a thermal state at 293 K, $[\delta u_0]_\mathrm{rms} = u_\mathrm{ZPM}\sqrt{k_\mathrm{B}T/hf_0} \sim 4$ pm. Therefore the white noise power spectrum of the electronic force is much larger than the power spectrum of the thermal noise.

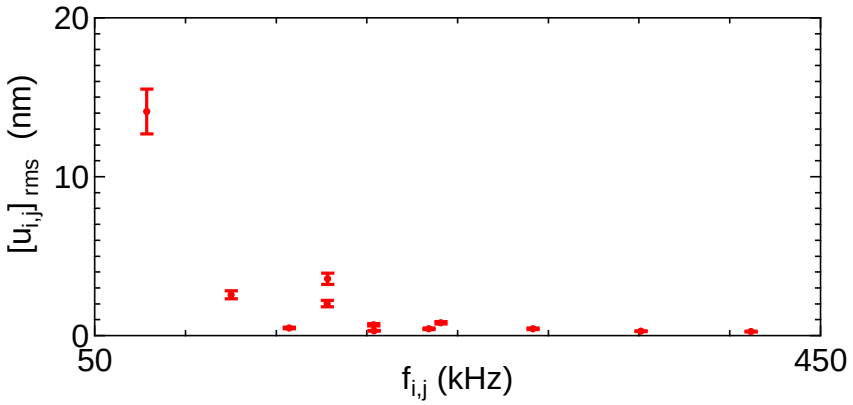


Figure 2.13: Extracted $[\delta u_{\mathrm{i,j}}]_\mathrm{rms}$ as a function of $f_{i,j}$ extracted from the measurements shown in Fig. 2.7.

2.6 Optomechanically Induced Transparency

Optomechanically induced transparency (OMIT) and absorption (OMIA) are signatures of optomechanical coupling and demonstrate that the membrane's motion can be actuated by radiation-pressure alone. OMIT and OMIA are characterized by the emergence of a transparency or absorption window in $|S_{21}|$ when a strong drive tone (f_D) and a weak probe tone (f_P) are injected into the cavity, and the frequency difference between these tones $\delta f = f_P - f_D$ coincides with the frequency of a mechanical mode [80]. When this condition is met, the beat between the drive and the probe field excites the membrane's motion and the destructive (constructive) interference of excitation pathways for the intracavity probe field results in a transparency (absorption) window in $|S_{21}|$. OMIT is the optomechanical analogue of electromagnetically induced transparency where the optical response of an atomic medium is controlled by an electromagnetic field [81].

OMIT has been demonstrated using a toroidal whispering-gallery-mode microresonator [80] and using a optomechanical crystal nanocavity [82]. It has also been demonstrated with a silicon nitride membrane in a membrane in the middle optical setup at room temperature [83] although it should be noted that this setup was at a vastly different frequency to mine and in the system was in the resolved sideband regime. A silicon nitride membrane was also used in a 3D microwave cavity [22] also in the resolved sideband regime. An advantage of working at room temperature is the large number of drive photons I am able to use to drive the cavity (in contrast to the cryogenic temperatures used in chapters 4 and 6). Thanks to this I am able to demonstrate OMIT in a high loss cavity in the unresolved sideband regime, on chip.

Figure 2.15 shows OMIT and OMIA which occurs when a strong drive tone at frequency f_D and a weak probe tone at frequency f_P are injected through a directional coupler at port 1 . Three different drive frequencies are shown; $f_D \sim f_C - \kappa/2$ (red detuned), $f_D \sim f_C$ (resonant) and $f_D \sim f_C + \kappa/2$ (blue detuned). When $f_D \sim f_C$, a peak (dip) is observed at $f_D - (+)f_0$ (Fig. 2.15(a)). When $f_D \sim f_C \pm \kappa/2$, Fano-like features appear at $f_D \pm f_0$ (Fig. 2.15(b,c)). There is not complete extinction or revival of the reflected signal as the system is well within the unresolved sideband limit.

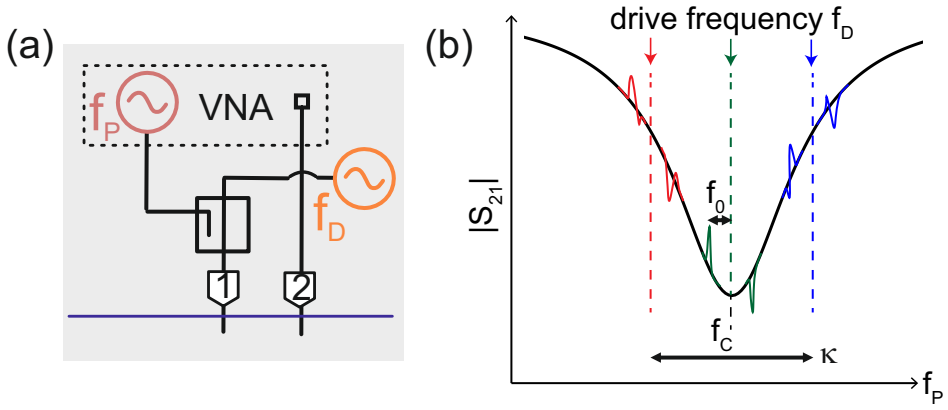


Figure 2.14: (a) Schematic of signal injection and detection for OMIT/OMIA measurements. A tone with frequency f_D and a tone with frequency f_P are injected through a directional coupler via port 1. The caivty reflection, $|S_{21}|$, is monitored with a vector network analyzer. (b) Schematic showing each of the drive frequencies injected and a cartoon of the mechanical sidebands appearing at $f_D \pm f_0$. Drive frequencies were $f_D \sim f_C$ (green), $f_D \sim f_C - \kappa/2$ (red) and $f_D \sim f_C + \kappa/2$ (blue). The corresponding mechanical sidebands are shown in Fig. 2.15

The OMIT and OMIA features can be fitted by modelling the transmission of the probe field. The transmission of the circuit in the presence of a weak probe tone at f_P and a strong drive tone at f_D, as shown in Fig. 2.15 is [1, 80]:

$$|S_{21}(\delta f)| = 1 - \frac{(1 - i\mathcal{F}(\delta f))\kappa_e}{2\pi i(\Delta + \delta f) + \kappa/2 + 4\pi\Delta F(\delta f)}, \tag{2.6}$$

where $\delta f = f_P - f_D$, $\Delta = f_D - f_C$ and

$$\mathcal{F}(\delta f) = \frac{\hbar\, g_0^2\, \chi_0(\delta f)\, \kappa_e\, S_{in}^2}{u_{ZP}^2(2\pi i(\delta f - \Delta) + \kappa/2)((2\pi\Delta)^2 + (\kappa/2)^2)}. \tag{2.7}$$

where χ_0 is the mechanical susceptibility of the fundamental mode and S_{in} is the photon flux incident from the drive tone

$$S_{in}^2 = \frac{\tilde{P}_D}{2\pi\hbar f_D}, \tag{2.8}$$

where $\tilde{P}_D$ is the power of the drive tone (P_D) having taken into account the overall insertion loss. In this case $P_D = 5$ dBm.

Using the values of $\kappa/(2\pi)$ and $\kappa_e/(2\pi)$ from the cavity fit, the curves in each panel of Fig. 2.15 are fit with equation 2.6. From the fit of the spectral features,

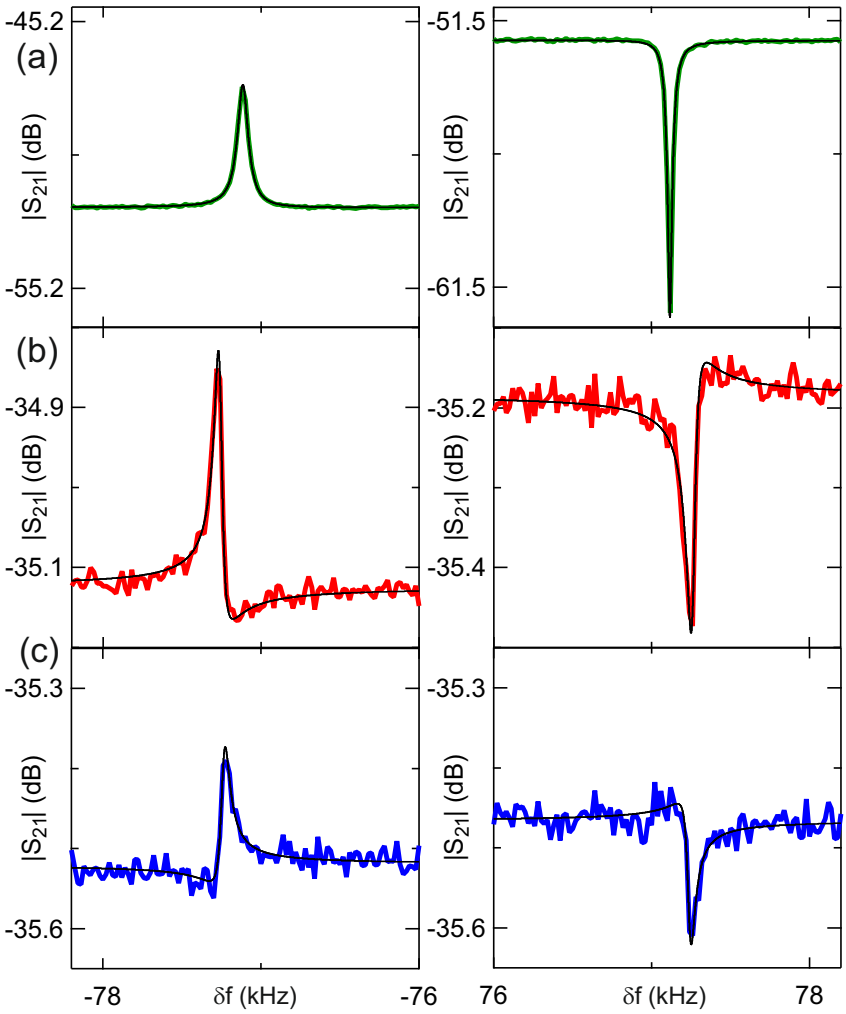


Figure 2.15: Measured $|S_{21}|$ as a function of δf showing mechanical sidebands at $\delta f \sim -f_0$ (left panel) and $\delta f \sim f_0$ (right panel) for each of the values of f_D considered in Fig. 2.14(b). At port 1, the drive power was 5 dBm and the probe power -27.5 dBm. Black curves are a fit to the data.

$f_0 = 77.2 \pm 0.1$ kHz, $Q_0 = (1.2 \pm 0.1) \times 10^3$ and $g_0/2\pi = 2.3 \pm 0.3$ mHz. Error bars are obtained by combining fit results of the six curves in Fig. 2.15. The values obtained for f_0 and Q_0 are similar to those extracted from the Lorentzian fits as in Fig. 2.7. The value of g_0 is in agreement with the extracted from Fig. 2.7 and estimated from the parallel plate capacitor approximation.

To estimate the amplitude of the membrane's motion one can consider the parametric amplification of the oscillator due to the beat frequency between the drive and probe tones [80]. For the OMIT measurement, the probe is 32.5 dB

weaker than the drive, hence the intracavity photon number is modulated by $N \approx 2 \times 10^{-32.5/20} n_C$ (neglecting any difference due to the cavity resonance as both tones are well within the linewidth). The circulating photon number is estimated to be $n_C \approx 5.2 \times 10^{12}$ (at 5 dBm). For OMIT the beat frequency is at f_0, hence the oscillator sees the parametric force $F = \hbar g_0 N \cos(2\pi f_0 t)/u_{ZPM}$. This force results in a coherent amplitude $u_{max} = \frac{\hbar g_0 Q_0 N}{m u_{ZPM} (2\pi f_0)^2} \sim 8.6$ nm, which is of the same order of magnitude, but slightly smaller than the amplitude of 14 nm from the white noise driving. This is significantly above the thermal motion for the fundamental mode.

2.7 Time Domain Measurements

The broad cavity bandwidth makes it possible to measure the actuated membrane's motion in real time as the photons esape from the cavity in a time negligible compared to the oscillation time of the membrane. To do so the membrane's motion is excited with white noise at port 3 whilst driving the cavity at f_C through port 1. In order to obtain the vibrations of the membrane at their fundamental frequency rather than as a sideband of the cavity drive tone the cavity output signal is mixed with a local oscillator as shown in Fig. 2.16. The demodulated output signal is shown in Fig. 2.17 and shows clear sinusoidal oscillations evidencing the membrane's motion. This form of measurement can be used to operate the setup as a thermodynamic clock as outlined in the next chapter.

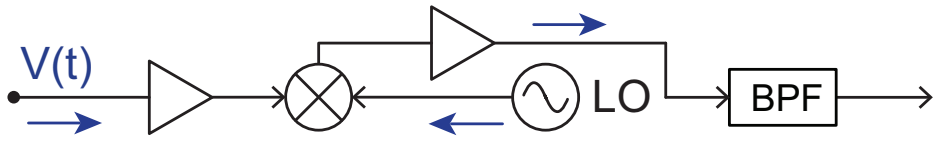


Figure 2.16: The demodulation circuit. (LO: local oscillator; BPF: band pass filter)

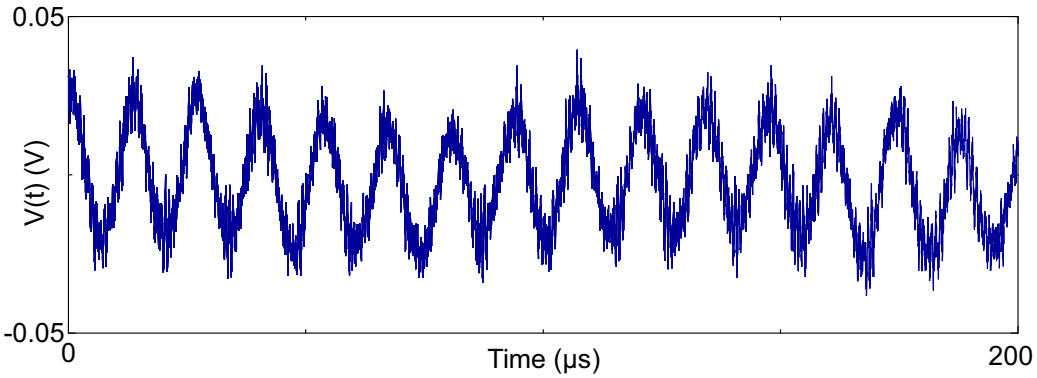


Figure 2.17: Demodulated cavity output signal as a function of time. Input power is P_{C}= 12 dBm at f_{C} and the white noise is $\mathrm{V_{WN}} = 3.6\ \mathrm{V_{rms}}$ at electrode 1.

3
Thermomechanical Clocks

Contents

3.1 Background: Autonomous Clocks 36
3.2 Experimental Determination of a Thermodynamic Trade-off in a Nanoscale Clock 39
3.3 Discussion 44

The best atomic clocks keep time to an accuracy of approximately one second in every one-hundred million years [84]. The magnetic moment of an electron g is known to be accurate to 9 digits [85] and computer arithmetic has an accuracy of 16 digits for 64 bit calculations [86], so timekeeping is one of the most precise skills humans have mastered. Despite this great progress in timekeeping, we know surprisingly little about the relation between quantum clocks (atomic clocks run by the rules of quantum mechanics, targeting a specific hyperfine transition in an atom's energy spectrum) and thermodynamics. The equations of quantum mechanics provide little explanation for the passage of time, being famously invariant under time reversal, in contrast to the theory of thermodynamics [87, 88].

One of the milestones at the intersection of the two fields is to derive a quantitative relation between the second law of thermodynamics and the flow of time. Investigations in this direction are a vital component in our understanding

of quantum thermodynamics, a field which concerns itself with the investigation, analysis and design of machines on the quantum scale, to which clocks are no exception [89]. In the quantum regime, as opposed to the classical case, the thermodynamic cost associated with the precise control of the system in question is of a similar scale to the system energies [90–92]. Quantum clocks have been studied rigorously from the perspective of open quantum systems, where it has been shown that their performance with respect to the resources they consume is subject to trade-off relations [87].

One of the challenges in deriving such trade-offs from microscopic thermodynamic principles is that the models require the systems be of a reasonably large size in order for thermodynamics and irreversible dynamics to appear naturally [93, 94]. Furthermore, in order to make predictions for the trade-offs the models are forced to make assumptions about the underlying parameters and system dynamics along the way [89, 95].

In this chapter I demonstrate that a trade-off derived for the quantum setting holds for the mesoscopic system described in the previous chapter, i.e. an electromechanical system incorporating a nm-thick membrane.

3.1 Background: Autonomous Clocks

A key feature of a clock is its ability to continuously provide a time reference to an external observer. This is in contrast to a system which simply allows one to measure a time interval. Such a system cannot truly be considered a clock - it is a stopwatch. It is therefore essential that any complete model of a clock contains the process of continuous information read-out. This leads to the treatment of a clock as a bipartite system [96] consisting of a pointer and a register as shown in figure 3.1. The dynamics of the pointer (which could also be called the escapement or the clockwork), are dictated by the passage of time, that is, it generates a time-ordered sequence of events (ticks). These ticks are recorded and stored as classical information by the register (which could also be called the dial, the terms pointer and register are chosen for consistency with Refs. [96] and [87]). The register

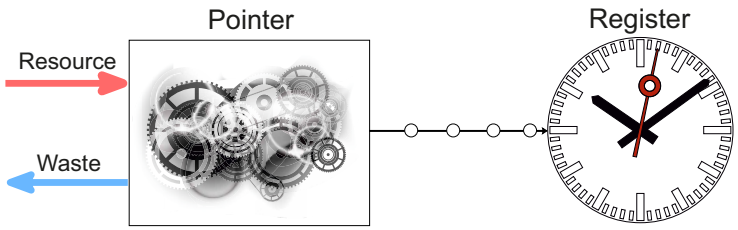


Figure 3.1: Schematic of how a clock can be considered a bipartite system consisting of a pointer and a register. From [87].

transfers the information from the system to an external observer. To be suitable for timekeeping this transfer of information should be asymmetric - information should flow from the pointer to the register to the observer, but not vice versa. The process is therefore irreversible and singles out a direction for the flow of time. Irreversibility is associated with the generation of entropy and the concept is thus connected to the second law of thermodynamics. A system that is suitable for measuring time is expected to produce entropy and this is one relationship that is explored in Ref. [87].

An autonomous clock is a clock that produces a stream of ticks without external control or timing input. In addition one should not require the use of a clock to prepare the resources which power the clock. The type of autonomous clock considered in Ref. [87] is one that is driven by minimal nonequilibrium resources; the flow of heat between two thermal reservoirs. One thermal reservoir is the environment, the other is a reservoir prepared at a temperature hotter than the environment. A further assumption in this model is that the time between any pair of consecutive ticks is statistically independent from, and identically distributed to, the time between any other pair of ticks. One could refer to this requirement as Markovian Stationarity.

Two parameters are used to quantify the performance of an autonomous clock. The first is the resolution of its ticks which I will refer to as the 'tick rate'. It is defined as

$$R := \frac{1}{t_{tick}}, \tag{3.1}$$

where t_{tick} is the average time between two ticks (with respect to a reference clock). This could also be called the frequency of the clock.

The second parameter is the accuracy of the clock, defined as

$$N := \left(\frac{t_{tick}}{\Delta t_{tick}}\right)^2, \tag{3.2}$$

where t_{tick} is the average time between ticks and Δt_{tick} is given by the standard deviation of the waiting times between ticks. The ticks of a clock are not always perfectly distributed, there may be some irregularities in the waiting times between the ticks. The accuracy refers to the number of ticks elapsed before the next tick is uncertain by the average time interval between the ticks. This can also be stated as the number of ticks N such that the standard deviation of the Nth tick time is equal to the average time between ticks. While the analysis for modern atomic clocks is done by using the Allan variance, which focuses on the stability of the output frequency, here the parameter of interest is the accuracy on a single tick level, i.e. no time averaging.

Two trade-offs are derived for the performance of autonomous clocks. The first trade-off is between the accuracy of the clock and the thermal energy used to drive it, or equally between the accuracy of the clock and its entropy production. This is because it is necessary for the driving to make the ticks identifiable above the environmental noise. Not all of the energy supplied to the clock, however, will be converted to useful work; some is dissipated into the environment and entropy is produced. The larger the energy supplied the higher the entropy production, linking this trade-off to the second law of thermodynamics. The larger the entropy production of the clock the more accurate it is predicted to be, until as predicted by the model the accuracy saturates. Below saturation, in Ref. [87], the entropy and accuracy of an autonomous clock are linearly related by

$$N \propto \frac{\Delta S_{tick}}{2}, \tag{3.3}$$

where ΔS_{tick} is the entropy production per tick.

The other, resulting, trade-off is between the accuracy and frequency (tick rate) of a clock and arises due to the prediction that a given amount of work can either produce a large number of ticks at a low accuracy or fewer ticks at a higher accuracy. It is the first trade-off that I explore.

The model, derived for open quantum systems, predicts that there is an intrinsic work cost in measuring time - is this connection between invested work (and therefore entropy production) and clock performance a specific aspect of the model or a universal feature of measuring time? It is not *a priori* obvious that trade-offs derived from the model will hold for more complex mesoscopic systems. This calls for a detailed experimental investigation to test the validity of the approximations used, and the validity of the derived trade-offs.

3.2 Experimental Determination of a Thermodynamic Trade-off in a Nanoscale Clock

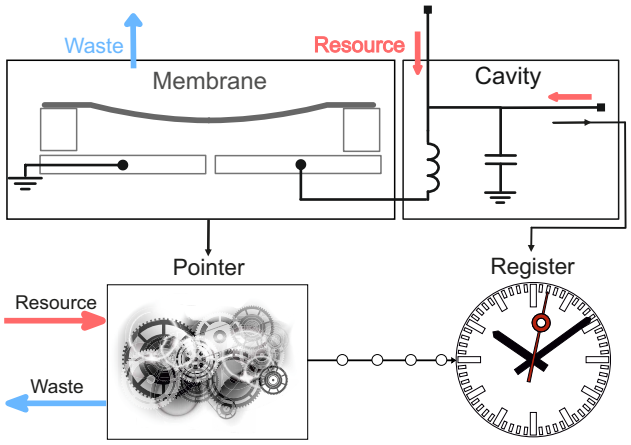


Figure 3.2: Schematic outlining how the device shown in the previous chapter, an electromechanical system consisting of a membrane coupled to an rf cavity, can act as a clock with the motion of the membrane acting as the pointer and the readout circuit as the register.

The experimental set-up described in chapter 2 can be used as a testbed for the study of the thermodynamics of autonomous clocks. The motion of a membrane provides the ticks, acting as a pointer for the clock, and the cavity reads out these ticks, acting as a register (Fig. 3.2). This system serves as a quasi-autonomous

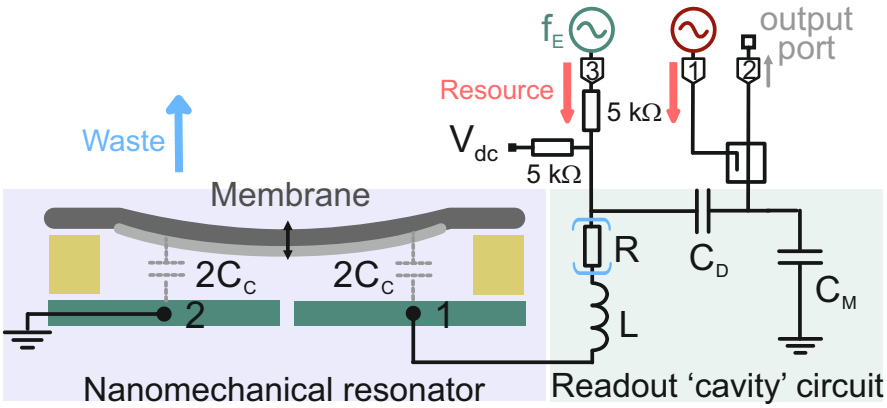


Figure 3.3: Experimental setup as shown in chapter 2 with arrows showing how resources enter the system and how waste is dissipated into the environment. For a full characterisation of the system see chapter 2.

clock, since with a cavity drive it is able to convert the power required to drive the membrane motion (in my case the white nosie drive) into the observable ticks of a clock. This experiment sits in an ideal regime, in some ways similar to Ref. [97], in which the system is too complex to be modelled by a simple open quantum systems approach yet is simple enough to account for the thermodynamic resources used. A thermodynamic analysis of its temporal performance is possible, whilst at the same time the system is too complex for a complete description of all its constituents.

As in the previous chapter, the cavity can be driven by injecting a rf signal to the input (port 1) via a directional coupler and port 3 allows the injection of white noise, V_{WN}, to excite the membrane's motion. The clock is thus powered both by the cavity drive and the white noise. The latter takes on the role of a thermal bath. Increasing the white noise power is equivalent to raising the effective mechanical temperature of the membrane or equally increasing the resources that I put into the system. While it is not straightforward to assign a temperature to the noise, it is a source of high entropy excitations that enter the system and one can expect that it is reasonably abundant in out of equilibrium environments.

To detect the ticks of the clock, the displacement of the membrane is measured in real time by demodulating the cavity output signal. This demodulated signal is measured in an oscilloscope as seen in Fig. 3.4 for two different values of V_{WN}.

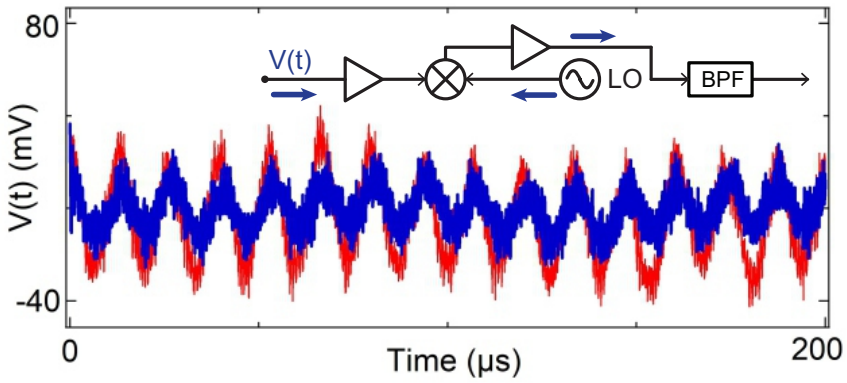


Figure 3.4: The demodulated cavity output signal V(t) as a function of time for an input power of 14 dBm to the cavity with 0.25 W (0.0625 W) white noise driving the membrane's motion for the red (blue) trace. The inset shows the demodulation circuit. (LO: local oscillator; BPF: band pass filter)

From these time traces the ticks of the clock can be identified, and an accuracy and tick rate can be calculated for each trace.

Traces of 1 s of cavity signal were recorded for several cavity driving powers and values of V_{WN}. The data analysis was done in collaboration with Dr Yelena Guryanova. The signal contains various sources of noise, therefore a band pass filter of 75 kHz, centred around 75 kHz was applied to all of the data. The width of the band pass filter was chosen to be slightly larger than the membrane's resonant frequency (which during this experiment was approx 74.5 kHz which is slightly different to the frequency in the previous chapter) in order to avoid introducing correlations to the oscillations. The tick identification is implemented by an algorithm that can be computed live or 'on the fly'. This ensures that the entire data set is not needed for the identification of ticks and that the system can indeed be operated as a clock and not as a stopwatch. It would defeat the purpose of a clock if one can only use a finished sequence of events to identify the ticks in retrospect. The algorithm locates the zero upward crossing of the signal and counts the number of data points before the location of the next upward crossing. The sampling rate was 40 MSa/s giving us 25 ns resolution for our analysis. We applied the same tick identification algorithm to all recorded traces, allowing for a meaningful comparison of the accuracy and tick rate. From the tick statistics

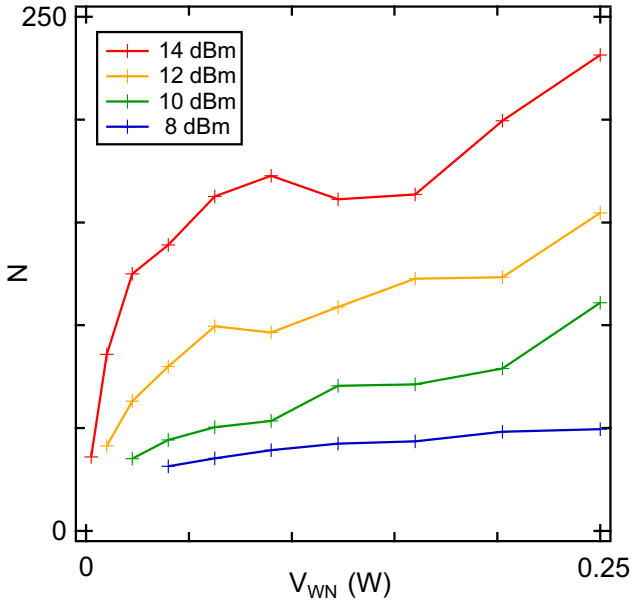


Figure 3.5: Accuracy of the clock vs the white noise power applied to input port 3 for a 75 kHz band pass filter applied to V(t) for cavity drive powers of 8, 10, 12 and 14 dBm.

we calculate the mean and the standard deviation of the tick rate, with respect to our reference clock which allows us to compute the clock accuracy. Given the frequency of the membrane, the measurement resolution puts an upper limit on a meaningful value of the accuracy we can compute of 290 000. The accuracies computed from the experimental data are well under this limit.

In addition to computing the accuracy we also extract the power in the mechanical sideband, that is we Fourier transform the signal V(t) and convert it to a power spectrum and take the area of the mechanical sideband giving the power in the sideband, P_{SB}. P_{SB} is proportional to the entropy produced by the membrane. It should be noted that this is an operation that is not done 'on the fly' but completed once the measurement has been completed. This is however not required for the accuracy computation, simply to demonstrate that the entropy produced by the membrane increases with the white noise driving. In this way I validate the claim that the increase in accuracy is indeed linked to the entropy production.

The demonstration of the trade-off predicted in Ref. [87] is displayed in Fig. 3.5. In the range of drive powers displayed in Fig. 3.5, an increased V_{WN} power increases

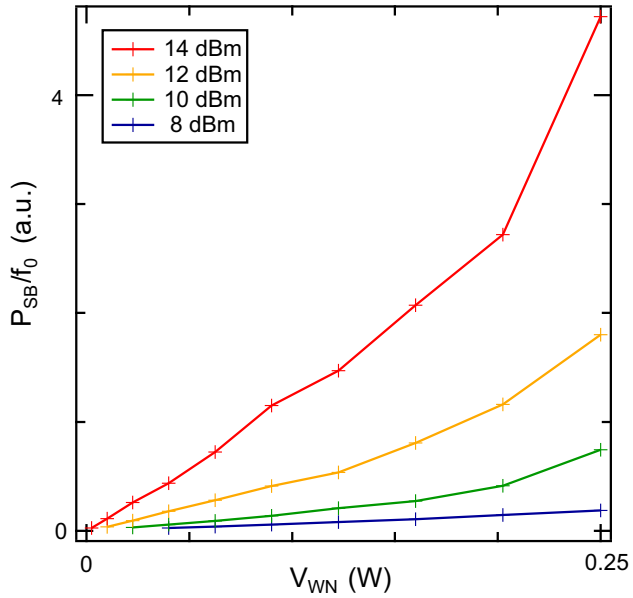


Figure 3.6: Area of the mechanical sideband divided by the membrane frequency vs the white noise power applied to input port 3 for a 75 kHz band pass filter applied to V(t) for cavity drive powers of 8, 10, 12 and 14 dBm.

the accuracy of the clock. The relation is approximately linear for the lower drive powers. The increase of accuracy with V_{WN} and with the cavity drive can be intuitively understood since a stronger drive will make the mechanical oscillations easier to distinguish from the background noise. The entropy per tick is proportional to P_{SB} divided by the frequency of the membrane, f_0. The increase in P_{SB}/f_0 for different drive powers with increasing V_{WN} is shown in Fig. 3.6.

Above a cavity drive power of 14 dBm the stability of the cavity signal fluctuates heavily, as shown in Fig. 3.7. In this case the relationship between the accuracy and white noise power is more erratic. The general trend of accuracy increasing with the white noise power is still there for the lower values of V_{WN}, but unstable dynamics dominates the motion of the membrane. As V_{WN} further increases, the linear relationship breaks down and saturation effects can be observed. This is to be expected from a finite physical system, as adding more and more heat to the system will at some point change the internal physical constitution of the system. The membrane cannot arbitrarily amplify its oscillations through noise.

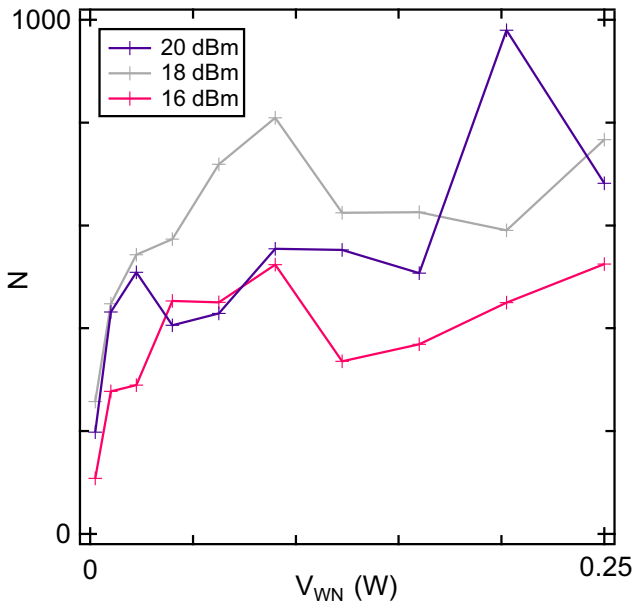


Figure 3.7: Accuracy of the clock vs the white noise power applied to input port 3 for a 75 kHz band pass filter applied to V(t) for cavity drive powers of 16, 18, 20 dBm.

The trend of entropy per tick increasing with the white noise power still holds for the higher drive powers as shown in Fig. 3.8.

Figures 3.5 and 3.6 show measurements down to a drive power of 8 dBm. This is due to the fact that below this drive power the signal is weak and identifying the oscillations corresponding to the membranes motion becomes difficult. Example traces corresponding to a white noise power of 0.25 W with 10, 8 and 6 dBm drive powers are shown in Fig. 3.9. For a 10 dBm drive oscillations can easily be identified, they are much fainter in the 8 dBm signal and for a 6 dBm drive they are not visible.

3.3 Discussion

This system holds an interesting relation to the phenomenon of stochastic resonance [98], where noise can push a signal beyond a detection threshold and with it actually increase the signal quality. This is in some sense similar to this system where adding noise reveals a periodic signal in time. There is however a fundamental difference, namely that I do not add noise the output signal but rather directly to excite the membrane's motion.

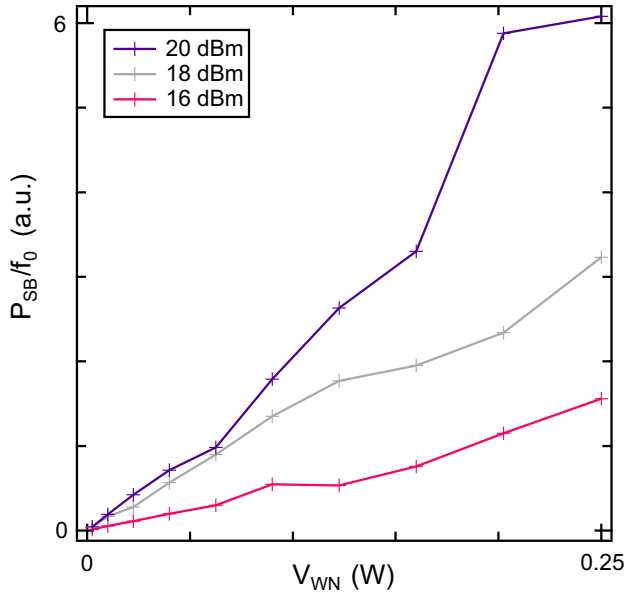


Figure 3.8: Area of the mechanical sideband divided by the membrane frequency vs the white noise power applied to input port 3 for a 75 kHz band pass filter applied to V(t) for cavity drive powers of 16, 18, 20 dBm.

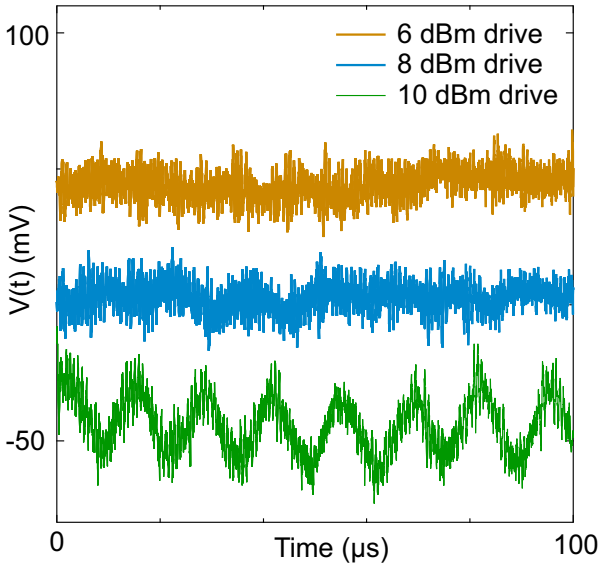


Figure 3.9: The demodulated cavity output signal, V(t) as a function of time for input powers of 10, 8 and 6 dBm to the cavity with 0.25 W of white noise applied at input port 3. The data is offset in the y direction for clarity.

Although the system is not fully autonomous, as a cavity drive is necessary for signal readout, it presents a perfect testbed for the exploitation of a thermal bath for the generation of a stable time-ordered signal. I have demonstrated how the power of the white noise introduced into the system enhances the accuracy of the signal, and also how it increases the entropy produced by the system. In this way, I have shown that a trade-off derived using a simple open quantum systems approach holds for this system. The qualitative correspondence of the trade-off between power and accuracy with the theoretical predictions of the model in Ref. [87] points toward a universality of this trade-off and corroborates the notion that the quality of the arrow of time is indeed determined by the entropy dissipated by a clock.

Thinking ahead to future work that could be done in this direction, a multi-membrane system (e.g. a modification of the double membranes demonstrated in Ref. [99]) would allow for the investigation of the operation of coupled clocks. If the setup were shielded from external vibrations a promising direction for future research would also be the investigation of amplitude fluctuations in time keeping signals. One could also investigate if the techniques used in the field of stochastic resonance could be applied to the output signal.

4

Radio Frequency Probing of Mechanical Motion at Cryogenic Temperatures

Contents

4.1 Measuring Motion at Cryogenic Temperatures 47
4.2 Direct Driving of the Membrane 48
4.3 Driving the Membrane with White Noise 51
4.4 Discussion 53

The membrane displacement can be detected at cryogenic temperatures with an rf cavity. In this way I characterise the membrane's motion at ~ 30 mK.

4.1 Measuring Motion at Cryogenic Temperatures

Cryogenic measurements require the use of a dilution refrigerator. The dilution refrigerator used was a *Triton 200* series by *Oxford Instruments* which can reach a base temperature of 10-20 mK (Fig. 4.1). It is a so called 'dry fridge' which makes use of a pulse tube cooler for the first stages of cooling down from room temperature down to around 10 K followed by a condensation cycle using a mixture of helium 3 and 4 to get down to base temperature.

The measurements taken in this chapter were taken using a reflectometry set-up as shown in figure 4.2. The signal is sent through Tx and attenuated by 25 dB



Figure 4.1: The inside of a dilution refridgerator like the one used in this chapter.

at 4 K and a further 6 dB at 600 mK in order to thermalise the electrons before being passed to a directional coupler thermalised to the mixing chamber at around 20 mK and through a stripline filter (which cuts high frequency signals to reduce the noise levels) before reaching the sample. On the way back the signal passes through a DC block before being amplified by 34 dB at 4 K with a cryogenic amplifier (CITLF2 from *Weinreb*) and is read out from Rx. The *Weinreb* amplifier is a SiGe low noise amplifier and has a noise temperature as low as 3.4 K at 1 GHz. It operates from 10 MHz to 2 GHz.

4.2 Direct Driving of the Membrane

The device used was similar to that of chapter 2. It consists of a slightly smaller 1 by 1 mm 50 nm thick, high stress silicon nitride membrane metallized with 20 nm

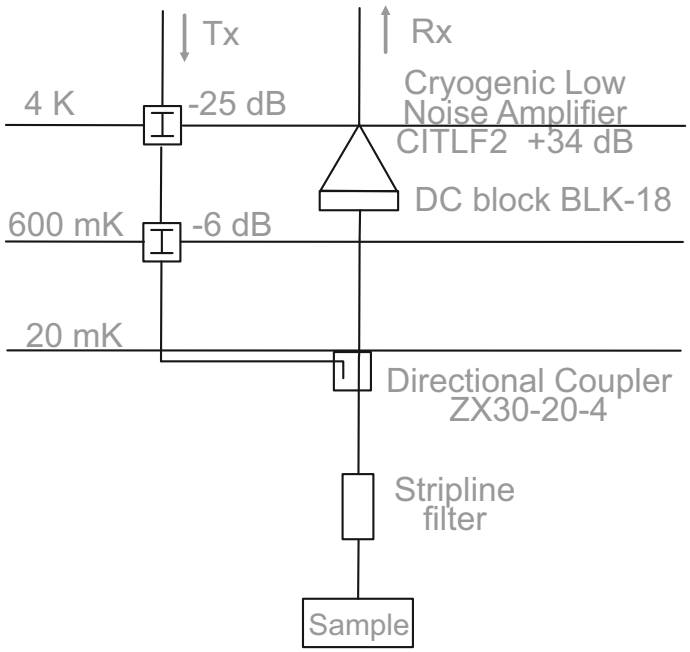


Figure 4.2: Schematic of the wiring in the fridge for the measurements taken in this chapter.

of aluminium (Al). The membrane is suspended over two Al electrodes patterned onto a sapphire chip. The electrodes are made of Al rather than gold as Al becomes superconducting below 1.2K so will induce less losses in the circuit. The base chip is made of sapphire rather than silicon in order to be compatible for use in a 3D cavity, inducing less losses. The base chip and membrane used in this chapter is the same as that used in chapter 5. As in chapter 2 one of the electrodes is grounded and one is connected to a rf tank circuit which acts as a cavity. As before the cavity has two input ports; port 1 to drive the cavity (and hence also the membrane through the optomechanical interaction) and port 3 connected to one of the electrodes to directly actuate the motion of the membrane.

The resonant frequency of the cavity is found by sweeping a MHz frequency tone. The cavity is fit using Eg. 2.1. This cavity at base temperature has a resonant frequency of 282.3 $\pm$ 0.1 MHz and a total decay rate $\kappa/2\pi$ of 16.16 $\pm$ 0.02 MHz giving a quality factor of 17.5. The ratio of coupling rates to the cavity, κ_e/κ is 0.60 (Fig. 4.4).

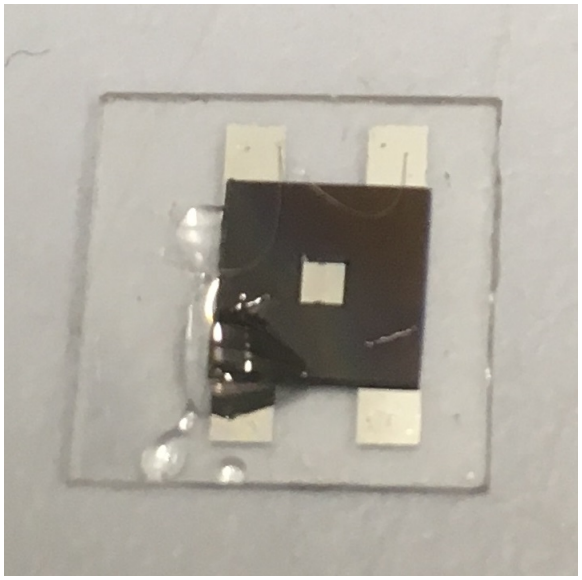


Figure 4.3: Device similar to that tested at low temperatures. The size of the sapphire chip is 1 by 1 cm, the membrane frame is 5 by 5 mm and the membrane is 1 by 1 mm.

As shown in chapter 2, a method of finding the mechanical resonance frequency of a device is to drive the cavity at its resonant frequency through port 1 whilst sweeping a kHz frequency tone through port 3. Due to the lower powers of the signals used at cryogenic temperatures in order to avoid heating and also due to the smaller amplitude of the vibrations of the membrane at cryogenic temperatures the mechanical signal from the device is expected to be much smaller than that at room temperature. The measurement shown in Fig. 4.5 was taken with a 10 dBm cavity drive at port 1 sent to the fridge. The cavity drive gets attenuated by 31 dB before reaching the sample plus incurring extra losses in the lines, and is sent at the cavity's resonance frequency. In addition a 4 V_{pp} kHz frequency signal modulated in a white noise pattern by 200 Hz to facilitate the detection of the modes sent via port 3. At first glance the measurement shown in Fig. 4.5(a) shows an extremely faint feature however an analysis of the maximum power of each column (Fig. 4.5(b)) shows that there is an increase in the peak height at 369.2 kHz and a zoom-in at this frequency shows a clear feature (Fig. 4.5(c)).

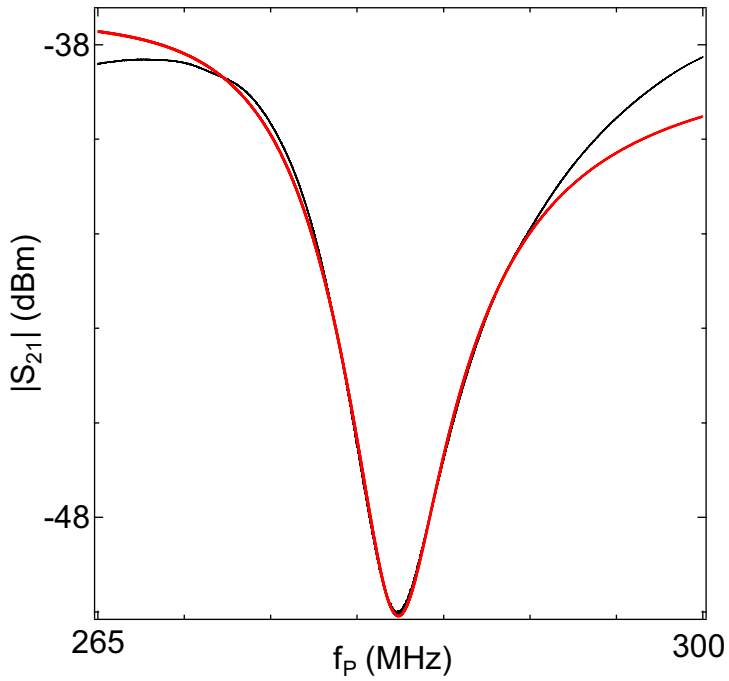


Figure 4.4: $|S_{21}|$ as a function of probe frequency f_P at base temperature (black) and a fit to the data using equation 2.1 (red).

4.3 Driving the Membrane with White Noise

As discussed in chapter 2, an alternative way to check for mechanical resonances in a device is to drive the cavity at its resonant frequency at port 1 and apply white noise to port 3. This has the effect of increasing the mechanical mode temperature of the device, increasing the amplitude of the vibrations and thus increasing the signal from the device. Figure 4.6 shows measurements of this kind taken with white noise of 1.5 MHz bandwidth with amplitudes of 4 V_{pp} (red) and 2m V_{pp} (blue), with a 10 dBm cavity drive. The peaks that become larger with a larger amplitude of white noise indicate mechanical resonances. In addition to growing with the amplitude of the noise increasing, these peaks also have the spacing expected of the modes of a square drum as shown in table 4.1 obeying the relation $f_{i,j}/f_0 = \frac{1}{\sqrt{2}}\sqrt{i^2+j^2}$ for integers i and j to within 1%. The higher modes such as 1,2 and 2,1 are nearly degenerate however imperfections in how the membrane was fabricated or fixed in place or uneven binding of the Al layer could cause this broken degeneracy. Modes

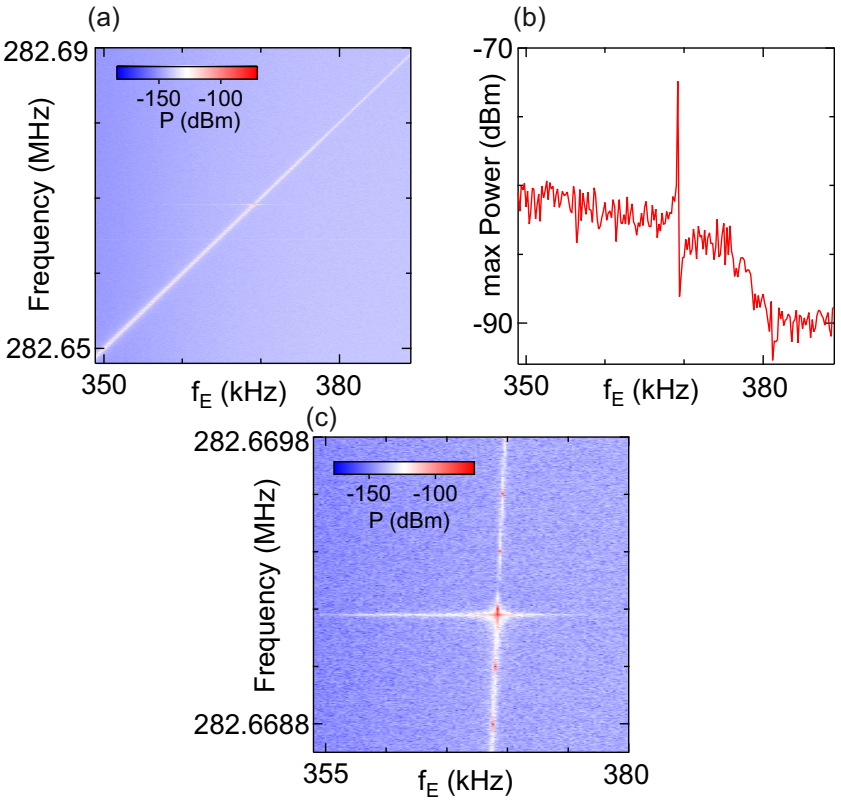


Figure 4.5: (a) Higher frequency sideband of the cavity drive when a kHz frequency signal f_E of amplitude 4 V_{pp} is swept. (b) Analysis of (a) showing the maximum value of each column which increases sharply at 369.2 kHz. (c) A zoom-in of (a) shows that the mechanical resonance signal is visible.

couple differently to the antenna as seen for the 1,2(3) and (3)2,1 modes, and as a result for the higher frequency less strongly coupled modes, even though the 2,3 and 1,4 modes are visible, their counterparts 3,2 and 4,1 are not.

A further way to investigate the mechanical signal is to focus on one mode, in this case the fundamental mode, and take a 3D plot of how it grows with the amplitude of the white noise as shown in Fig. 4.7. This measurement shown in Fig. 4.7(a) was taken with a 10 dBm cavity drive at the resonant frequency of the cavity through port 1 and 0.002-4 V_{pp} white noise with a 500 kHz bandwidth at port 3. Fig. 4.7(b) shows a cut of the 3D plot at 1 Vpp and a Lorentzian fit to the peak. Fig. 4.7(c) shows how the quality factor of the membrane changes with the amplitude of the voltage used to drive it. The average quality factor of the measurements shown in Fig 4.7(c) is 190 000 $\pm$ 80 000. The error comes from the uncertainty of the fit.

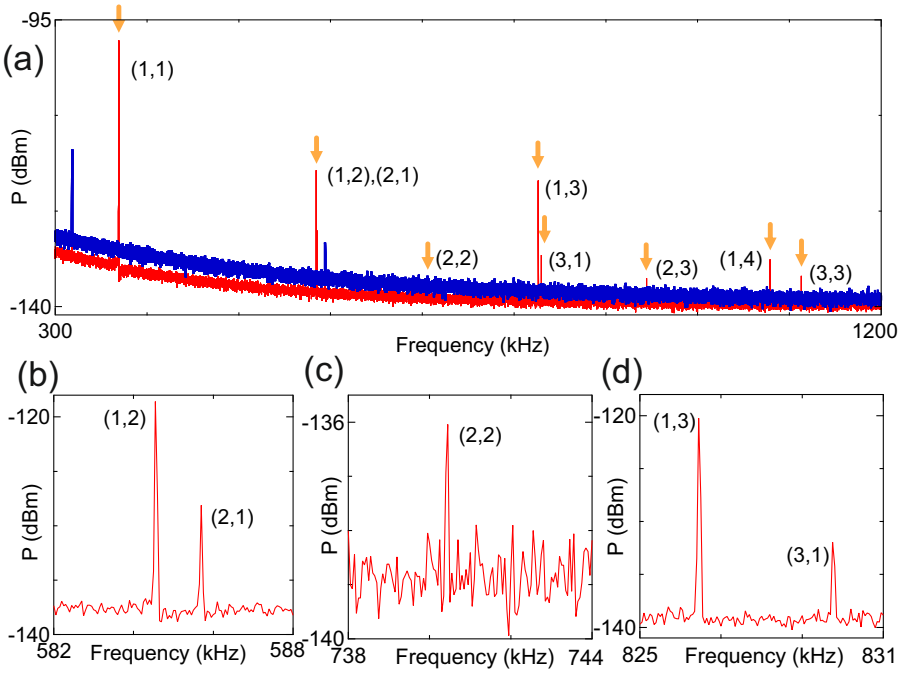


Figure 4.6: (a) Reflected power from the cavity as a function of frequency taken with white noise of 1.5 MHz bandwidth with amplitudes of 4 V_{pp} (red) and 2 mV_{pp} (blue), with a 10 dBm cavity drive at the cavity's resonance frequency. The modes are labeled with arrows. (b) Zoom-in showing the splitting of the 1,2 and 2,1 modes. (c) Zoom-in showing the (2,2) mode which is not visible on the scale used in (a). (d) Zoom-in showing the splitting of the 1,3 and 3,1 modes.

Mode	Predicted Frequency (Hz)	Measured Frequency (Hz)	Percentage Deviation (%)
(1,1)	-	369 150	-
(1,2),(2,1)	583 677	584 550, 585 700	0.15, 0.35
(2,2)	738 300	740 450	0.29
(1,3),(3,1)	825 444	826 450, 829 750	0.12, 0.52
(2,3),(3,2)	941 152	944 250, -	0.33, -
(1,4),(4,1)	1 076 248	1 078 950, -	0.25, -
(3,3)	1 107 450	1 113 000	0.5

Table 4.1: Table showing the predicted and measured frequencies for the modes of a square drum as measured for the device

4.4 Discussion

This chapter has demonstrated that this setup provides an efficient tool to characterise the properties of a membrane at cryogenic temperatures. The setup is of course not limited to silicon nitride membranes. The properties of other

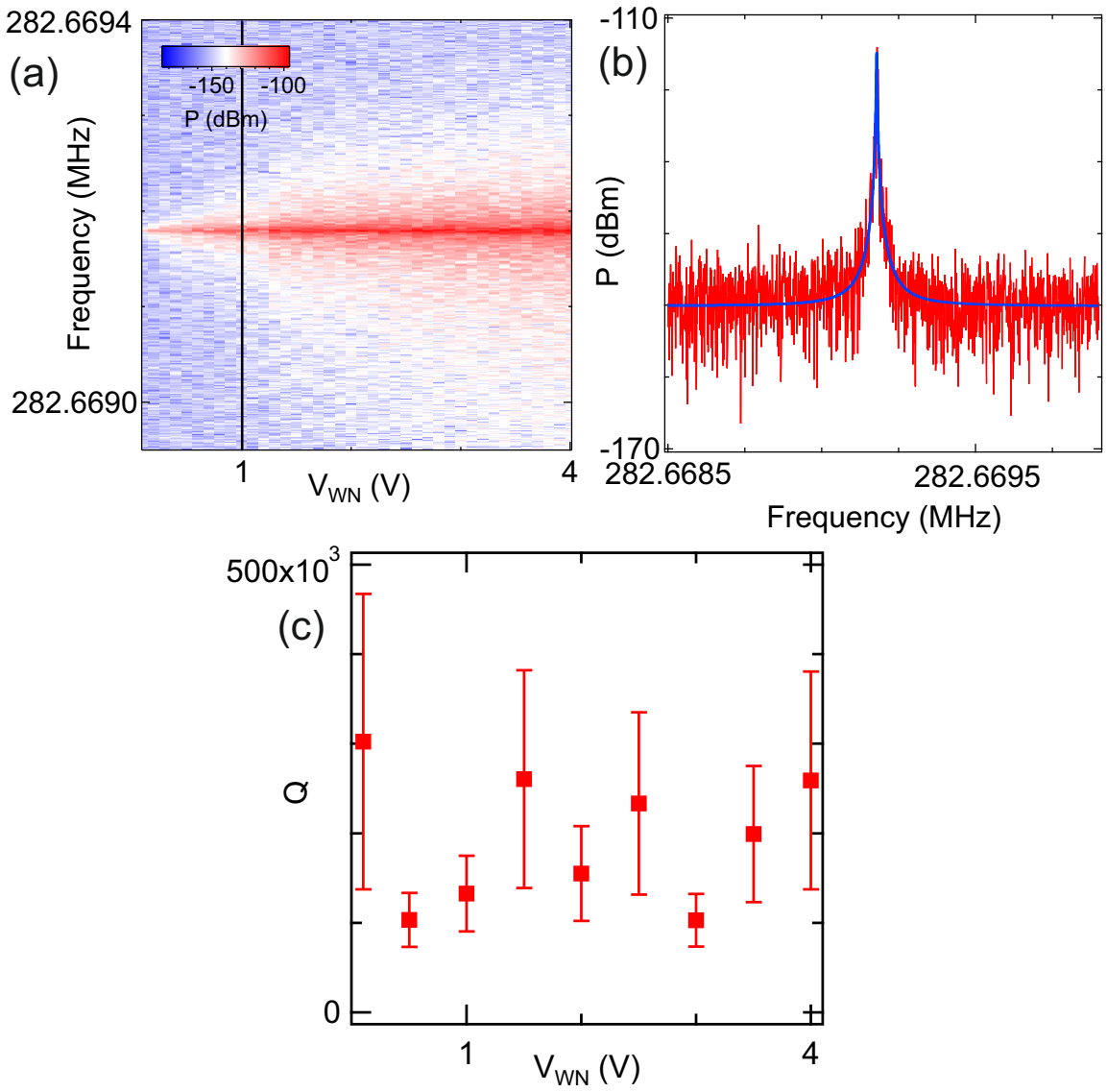


Figure 4.7: (a) Lowest mechanical mode as a function of V_{WN}. The cavity drive is at 282.3 MHz and the signal is at the mechanical frequency above this. The black line shows the cut for (b). (b) Cut of (a) (red) fit with a Lorentzian (blue). (c) Extracted quality factors of the peak from the Lorentzian fits.

membranes such as e.g. diamond like carbon [100] could be investigated at cryogenic temperatures. One could also do a study on the effect of membrane thickness on the mechanical properties such as quality factor and frequency at low temperatures and also on how different shapes such as the so called 'trampoline resonators'[4, 5] respond to the cool down process.

5

Microwave Optomechanics with a 3D Cavity

Contents

5.1 Device Design 56
5.2 Measuring Superconducting Cavities at Cryogenic Temperatures 57
5.3 Measurements of Electromechanical Sidebands 60
5.4 Increasing the Measurement Resolution 61
5.5 Determination of the Mode Temperature 64
5.6 Discussion 67

Different cavities have different advantages. The large bandwidth of the lumped element cavity allows for fast readout of the mechanical motion, while a cavity with a higher quality factor allows for more sensitive measurements. This is due to the fact that each photon interacts more times with the membrane before leaving the cavity. To explore this capability, which will allow me to investigate the role of gravitation in quantum mechanics, I used a 3D superconducting aluminium cavity [22], which has been used in the superconducting qubit community for readout of superconducting qubits [101]. In this chapter, I demonstrate measurements of thermomechanical motion in this setup.

5.1 Device Design

The 3D cavity is made of high purity aluminium, which becomes superconducting at cryogenic temperatures below 1.2 K. The dimensions of our cavity are 28 x 28 x 8 mm. The inside of the cavity was etched for 4 hours with aluminium etchant to improve the inner surface and increase its quality factor. SMP connectors with an extruding pin allow for insertion and detection of a microwave signal in the cavity. The length of the extrusion of the pins controls the coupling of the microwave photons to the cavity, with longer pins giving stronger coupling but also increasing the linewidth of the cavity. In order to be sideband resolved the linewidth of the cavity must be smaller than the mechanical frequency of the mechanical resonator. In the centre of the cavity I place a sapphire chip on top of which is patterned an aluminium antenna of approximately 100 nm thickness like in chapter 4. The antenna is made using photolithography. A 1 by 1 mm, 50 nm thick high stress silicon nitride membrane metallized with 20 nm of Al is placed on top of the antenna and secured with a drop of epoxy, like in chapters 2 and 4. Several devices were made, some with a second step of photolithography to pattern 100 nm tall pillars on top of the antenna however it was found that the limiting factor in the spacing between the membrane and the antenna was not the height of the pillars but rather residue which formed a larger μm gap. A crude estimate of the gap between the antenna and the membrane can be made by placing the device in an optical microscope and focusing first on the aluminium forming the antenna (visible through the edges of the membrane which are not covered in aluminium). The focal length of the microscope is then changed until the edge of the aluminium covering the membrane is in focus and the gap taken from the change in focal length.

Devices are then bonded to a lumped element cavity and tested to find out at which frequency the fundamental resonance frequency lies, first at room temperature and then at cryogenic temperatures as outlined chapters 2 and 4. Of 8 tested devices one gave a mechanical signal at both room and low temperatures. The low temperature measurements of this device are shown in chapter 4. This device was placed inside the 3D cavity (Fig. 5.1) and cooled down in a dilution refrigerator.



Figure 5.1: A photo of the optomechanical system used in this chapter. Inside the 3D aluminium cavity is a sapphire chip with an Al antenna patterned on it. A 1 by 1 mm 50 nm silicon nitride membrane metallized with 20 nm of Al is placed over the antenna and secured with epoxy. The two SMP connectors with a pin inside allow for insertion and detection of a microwave signal.

5.2 Measuring Superconducting Cavities at Cryogenic Temperatures

The dilution refrigerator used is a *Triton 200* from *Oxford Instruments* like the one used in chapter 4. The wiring needed for the microwave measurements is however different to that used for the rf measurements. At GHz frequencies $1/f$ noise is not much of an issue however thermal (Johnson) noise is. To suppress this, all microwave signals sent into the fridge are strongly attenuated. As shown in Fig. 5.2 the signal is attenuated by 20 dB at the 4 K plate, another 20 dB at the 100 mK plate and a further 10 dB at the mixing chamber which has a base temperature of around 20 mK.

On the path out an isolator (CWJ1019KS41 from *Pamtech*) is used in order to protect the sample from the thermal noise of higher temperature stages. In order to be able to detect the output signal it is amplified by 40 dB at the 4 K stage using

a low noise amplifier (LNF-LNC1_12A from *Low Noise Factory*). The amplifier is operational from 1-12 GHz and has a noise temperature of 4 K at 6 GHz. If needed further amplification can be carried out at room temperature.

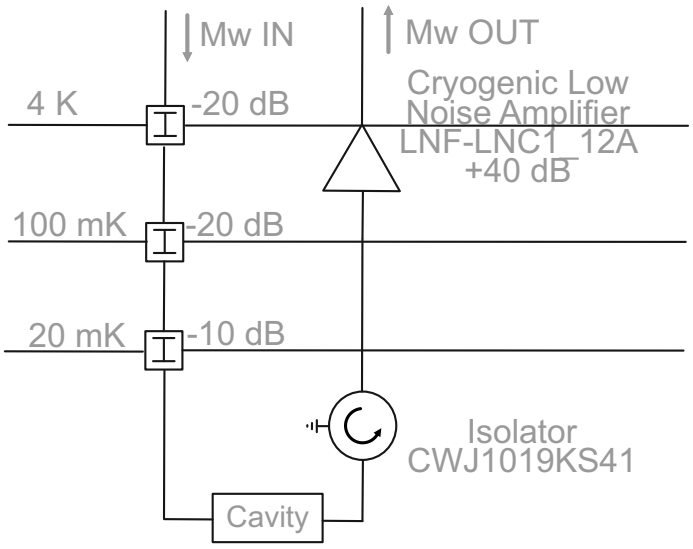


Figure 5.2: Cryogenic microwave transmission setup. A signal sent into the fridge through Mw IN is attenuated by a total of 50 dB before reaching the sample. On the way out it is passed through an isolator which protects the sample from thermal noise before being amplified by 40 dB at the 4 K plate and exiting the fridge through Mw OUT.

To characterise the cavity I take a measurement of the cavity's quality factor, however this gives the loaded quality factor Q_L which is a combination of the internal and external quality factors Q_{int} and Q_{ext} respectively [102].

$$\frac{1}{Q_L} = \frac{1}{Q_{int}} + \frac{1}{Q_{ext}} \tag{5.1}$$

and

$$IL = -20log\left(\frac{r}{r+1}\right) dB \tag{5.2}$$

where IL is the insertion loss and $r = Q_{int}/Q_{ext}$. These two equations can be combined to give

$$Q_{int} = \frac{Q_L}{1 - 10^{\frac{-IL}{20}}} \tag{5.3}$$

$$Q_{ext} = Q_L \times 10^{\frac{IL}{20}} \tag{5.4}$$

The cavity transmission can be fit using the following expression [103]

$$|S_{21}|^2 = -IL - 10log(1 + 4Q_L^2(f/f_0 - 1)^2) \tag{5.5}$$

At base temperature (which was approx 40 mK during this experiment) with the sample inside the cavity had a quality factor of 29 980 ± 80 and a resonant frequency of 6.02605 ± 0.00001 GHz as seen in Fig. 5.3. The red curve is the data and the blue curve is a fit using eq. 5.5. The calibrated insertion loss is 31.63 ± 0.05 giving $\kappa/2\pi = 201.0 \pm 0.5$ kHz, $\kappa_e = 5.27 \pm 0.03$ kHz, $\kappa_i = 195.7 \pm 0.5$ kHz and $\kappa_e/\kappa = 0.026$ so the cavity is undercoupled.

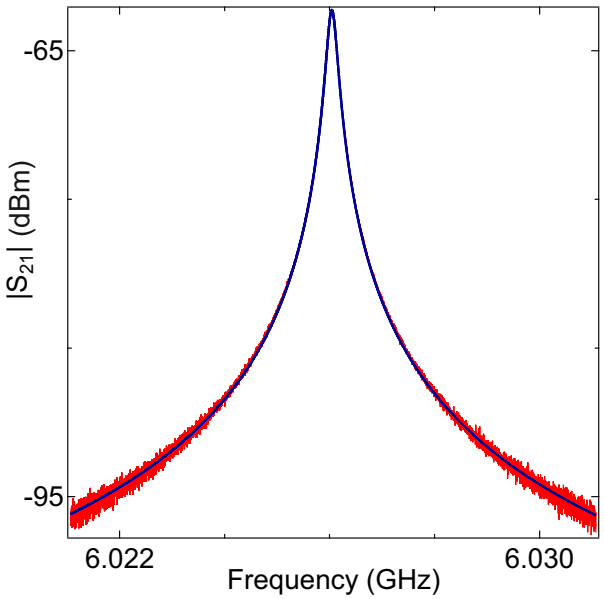


Figure 5.3: Cavity transmission as a function of probe frequency (red) and a fit using equation 5.5 (blue).

The quality factor of the cavity is not constant with temperature. As seen in Fig. 5.4 above 150 mK it starts to decrease from around 30 000 down to 15 000 at 900 mK. For these measurements, taken in two separate runs during the same cooldown (during the cooldown the temperature was changed but never above the superconducting transition temperature of aluminium), the cavity was allowed to thermalise every time the temperature was changed for at least one hour.

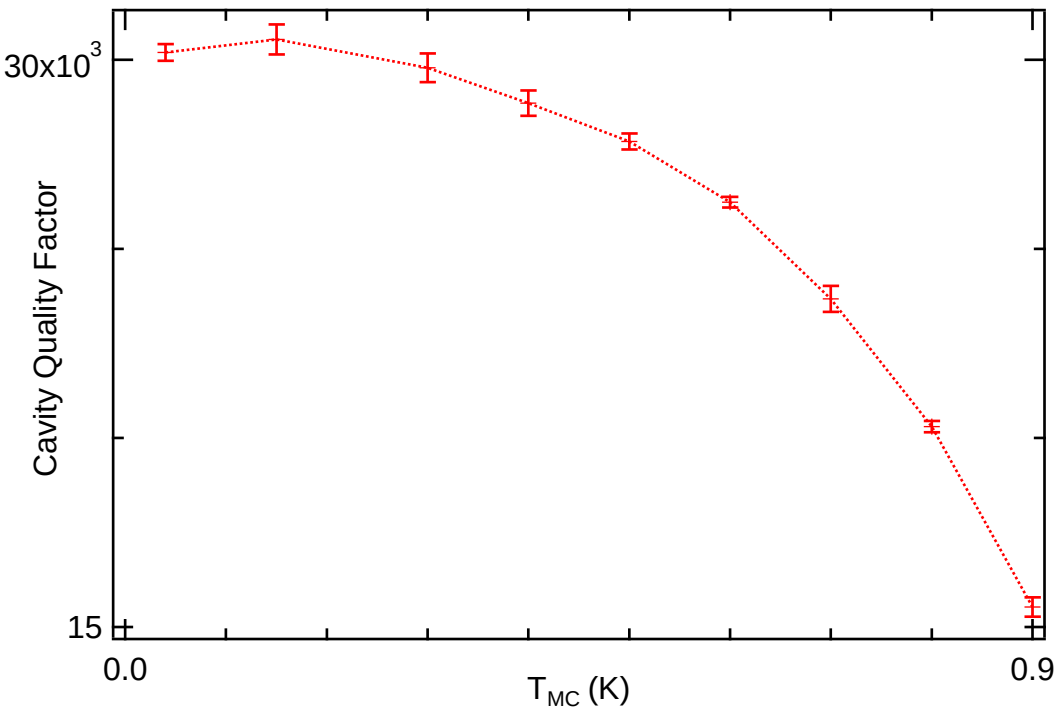


Figure 5.4: Cavity quality factor as a function of the mixing chamber temperature, T_{MC}. The error bars span the results from two separate runs of the experiment taken during the same cooldown in which the superconducting transition temperature of the cavity was not exceeded.

5.3 Measurements of Electromechanical Sidebands

If the cavity is driven with a single tone at its central frequency sidebands appear separated by the mechanical frequency both at a higher frequency and a lower frequency than the drive tone. These can be seen in a spectrum analyser as seen in Fig. 5.5 but limited to a resolution bandwidth of 1 Hz. As silicon nitride membranes have been reported to have quality factors as high as 10^8 [3] at cryogenic temperatures, corresponding to linewidths of around 2.5 mHz, a resolution bandwidth of 1 Hz is expected not to be narrow enough to accurately obtain the shape of the resonance of the membrane.

The peak shown in Fig. 5.5 is taken with the pulse tube on. (As briefly discussed in chapter 4 the pulse tube cools the fridge down from room temperature to around 10 K by mechanically pumping on helium. The motion of the pulse tube causes mechanical vibrations in the fridge.) I found that when the pulse tube is on the

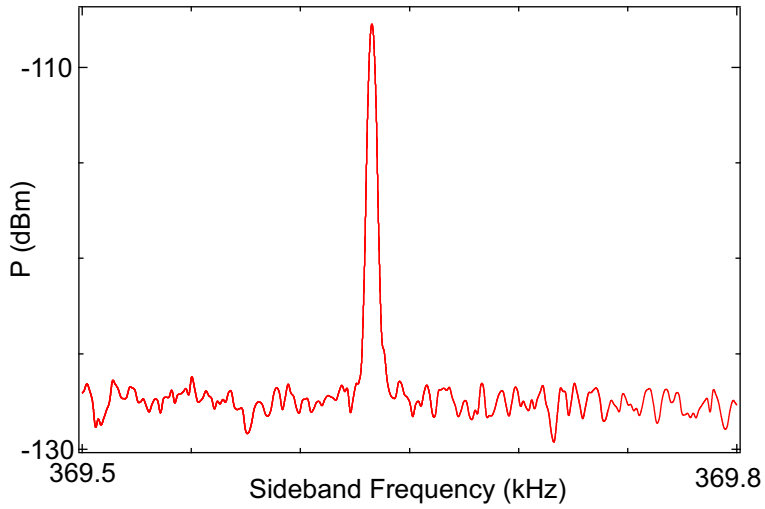


Figure 5.5: Sideband corresponding to the membrane's resonance. The pulse tube is on for this measurement.

motion of the membrane is vastly increased. To obtain an accurate measurement of the motion of the membrane due to its thermal energy the pulse tube must be turned off, the membrane allowed to ring down, and the measurement taken all within a window of approximately three minutes before the fridge starts to heat back up again. During this time the 4 K plate and the magnet inside the fridge heat up to about 7 K but the mixing chamber temperature stays constant. It takes around 15 minutes for them to cool back down again. Figure 5.6 shows a measurement of the mechanical sideband with the pulse tube of the fridge that the sample is in turned off compared to when it is on. I found however that it was not enough to simply turn off the pulse tube of the fridge I was working in. The blue peak in Fig. 5.6 is still increased by the effect of the other pulse tubes in the lab. If all the pulse tubes in the lab are turned off a signal is not visible in the spectrum analyser due to its bandwidth of 1 Hz.

5.4 Increasing the Measurement Resolution

In order to decrease the resolution bandwidth of the measurement and increase the resolution of the measurement I implement time-domain measurements and Fourier

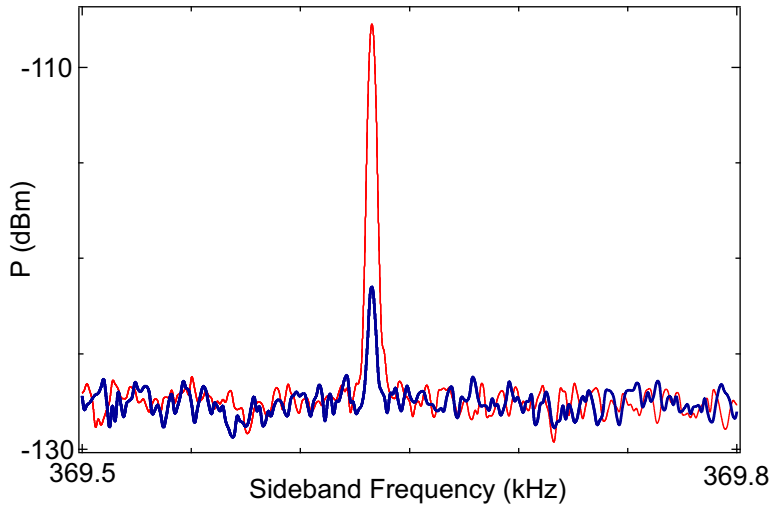


Figure 5.6: Mechanical sideband with the pulse tube on (red) and off (blue). For the blue trace two other pulse tubes in the same room were still on.

transformed the signal. I used a data acquisition card (Alazartech 9440) with a maximum sampling rate of 125 MS/s in order to acquire the signal.

For ease of signal processing I demodulate the signal, as a 6 GHz signal cannot be processed by the computer. The first step is to demodulate down to rf frequencies and I choose 150 MHz to be in the operational range of both the mixer and rf lock in amplifier. In the lock in amplifier I demodulate further down to 40Hz in order to be able to use a narrow bandpass filter of 100 Hz around the local oscillator tone. This reduces the noise level, and in addition allows for the minimum sampling rate of the Alazartch card of 10 kHz to be used to acquire signal, reducing the requirements on the computer's memory. The set-up is shown in figure 5.7 and is as follows:

1) The signal which is sent into the cavity, at its resonant frequency, is split using a PD40 power splitter. Half is sent into the fridge and to the cavity and half is sent through fixed attenuators, a variable attenuator (0-30 dB, RFVAT0218A30) and a manual phase shifter (RFPSHT0018W7) into the CPL port of a directional coupler (ZUDC20-183+) in order to act as a cancelling tone to the tone that comes out of the fridge. This cancelling tone is needed to reduce the amplitude of the signal entering the amplifiers at room temperature.

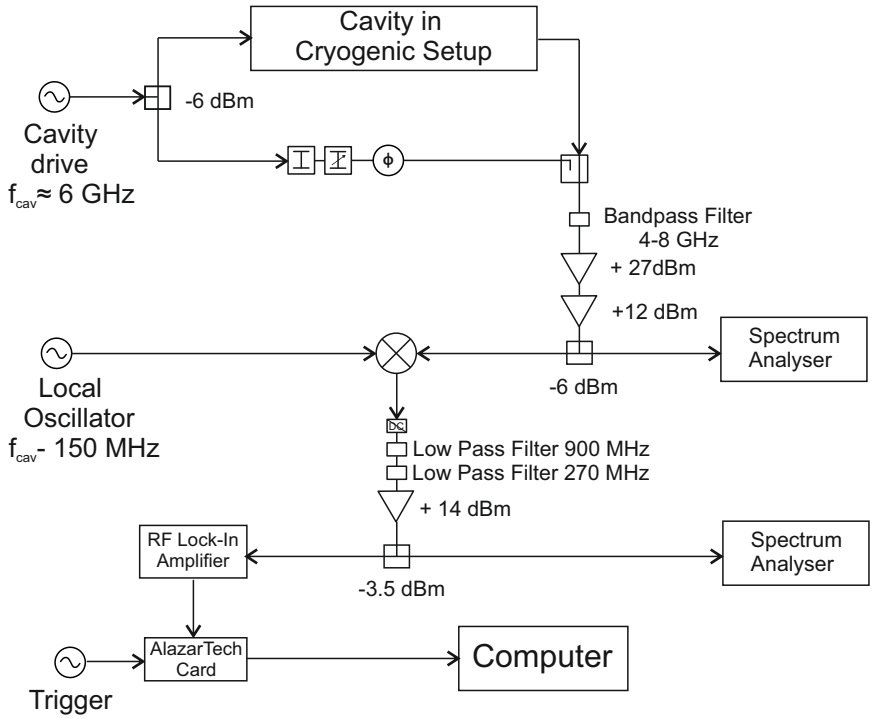


Figure 5.7: Multi-step demodulation process to take the sideband frequency down to 40 Hz. See main text for a description of each component

2) The tone that comes out of the fridge is fed into the OUT port of the directional coupler and combined with the canceling tone to exit via the IN port. The signal exiting is approximately 30 dB smaller with the cancelling tone applied.

3) The signal is then filtered using a 4-8 GHz filter (KBF-4/8-Q7S) and amplified by +27 dBm (ZVA-183-S+) and +12 dBm (ZX60-14012L-S+).

4) The amplified signal is split and half is passed to a spectrum analyser (Agilent N9010 EXA) in order to monitor the sidebands before demodulation. The other half is fed to the RF port of a mixer (ZX05-153-S+) where it is mixed with a local oscillator at 150 MHz below the cavity tone, entering the LO port from a signal generator (SG386) .

5) The signal leaving the mixer via the IF port is passed to a DC block (PE8212) and two low pass filters (SLP-1000+ LPF DC-900MHz, SLP-300+ LPF DC-270MHz) into a x5 amplifier (Stanford Research Systems SR445A).

6) The signal leaving the SR445A amplifier is split (ZESC-2-11+). Half goes to a spectrum analyser to monitor the demodulated sideband at 150 MHz plus the

mechanical frequency and half goes to a lock-in amplifier (Zurich Instruments UHF).

7) Inside the lock-in amplifier the signal is mixed with a tone at 150.369672 MHz in order to demodulate the signal down to 40 Hz. It is passed through a bandpass filter of 100 Hz around the central tone. The 'demod X' signal is amplified by a factor of 50 000 and sent to the Alazartech card (9440). The settings are 50 Ω AC coupling, 100 mV range and 1V/V scaling and the clock was synchronised with the other signal generators and spectrum analysers.

8) 1 million samples are taken using the Alazartech card with a clock rate of 10 kSa/s to give an acquisition time of 100 s. The settings of the Alazartech card were DC coupling, ± 400 mV for the range and 50 Ω impedance. An external trigger (Agilent 33510B) was used for the acquisition card with a 1 kHz, 2 Vpp, 50% duty cycle, square wave with 50 Ω coupling.

The Fourier transform of this data gives a resolution of 10 mHz. In order for the peak to be visible in the noise floor four traces are taken, Fourier transformed and then averaged. The average trace is then converted into units of watts. An example of the result at 700 mK is shown in Fig. 5.8 where the red trace is the smoothed data and the blue is a Lorentzian fit to the peak. The fit gives a mechanical decay rate of 0.199 ± 0.006 Hz giving a quality factor of the membrane of $1\,860\,000 \pm 50\,000$. From this fit the area of the peak can be calculated and the mode temperature determined.

Figure 5.9 shows the quality factor of the membrane as a function of temperature averaged for both runs of the experiment. There is no discernable trend in the data, although there is variation between two points taken at the same temperature as seen from the large error bars. This could indicate that the quality factors may be affected by external vibrations in the lab which I have no control over, or that the membrane is not thermalising properly. The average quality factor is $2\,400\,000 \pm 700\,000$.

5.5 Determination of the Mode Temperature

The mode temperature of the membrane is proportional to the area of the electromechanical sideband. We are interested in the power of the sideband. In our case the conversion is a multistep process. We first take the magnitude

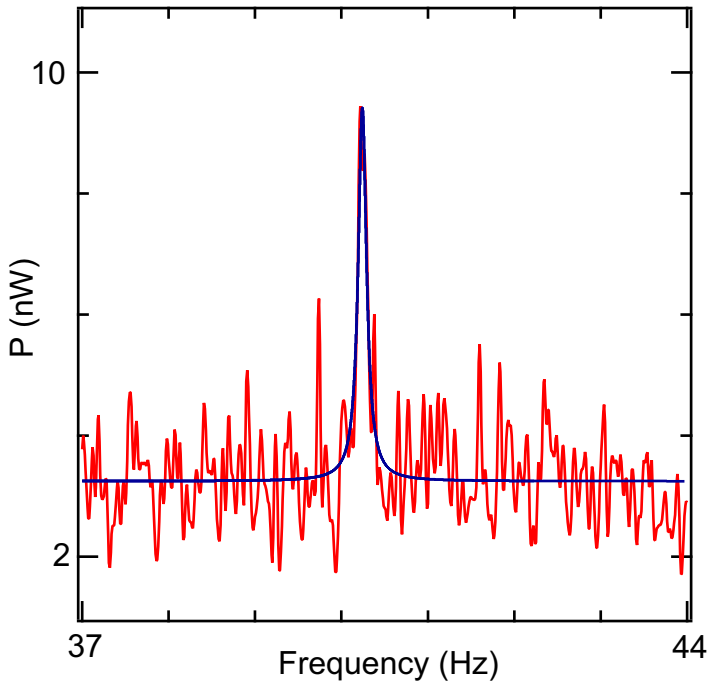


Figure 5.8: Power spectral density from the normalised Fourier transform of the time trace taken, showing the mechanical signal from the membrane at 700 mK with an input power of 18 dBm to the fridge and all pulse tubes turned off. The data has been smoothed by a factor of 5 (red) and is fitted with a Lorentzian (blue).

of the Fourier transform and normalise it as outlined in Ref. [104] to give an amplitude spectrum in volts rms.

$$\text{Amplitude spectrum in } \mathrm{V_{rms}} = \frac{\sqrt{2}\,\text{Magnitude[FFT]}}{N} \tag{5.6}$$

where N is the number of points in the time trace. The amplitude spectrum squared divided by 50 Ω (the resistance of the lines) gives a power spectral density in units of watts.

The power of the sideband, $\mathrm{P_{SB}}$, at frequency ω is related to the number of phonons of the membrane n_m by the following equation (supplementary material of Ref. [22]),

$$P_{\mathrm{SB}}(\omega) = P_{in}\, g_0^2\, 2\, n_m \frac{(\frac{\kappa_e}{2})^2}{(\frac{\kappa}{2})^2 + (\omega - \omega_{r,b})^2} \frac{1}{(\frac{\kappa}{2})^2 + (\omega - \omega_0)^2} \tag{5.7}$$

where P_{in} is the power into the sample, g_0 is the single photon coupling strength ω is the frequency you are at, $\omega_{r,b}$ is the frequency of the red or the blue sideband

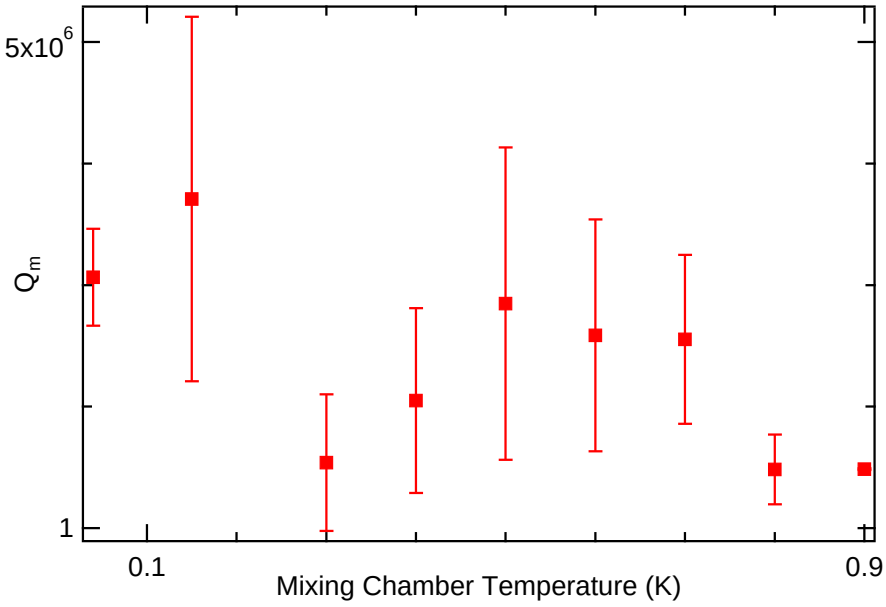


Figure 5.9: Quality factor of the membrane as a function of the mixing chamber temperature. The values are the average of two experimental runs (within the same cooldown in which the superconducting transition temperature of the cavity is not exceeded) and error bars span the different values obtained in each experimental run.

and ω_0 is the cavity's resonant frequency.

As ω is at the sideband frequency we can rewrite equation 5.7 and say that n_m equals

$$n_m = \frac{P_{\mathrm{SB}}}{2P_{in}g_0^2}\left(\frac{\kappa}{\kappa_e}\right)^2\left(\left(\frac{\kappa}{2}\right)^2+\omega_m^2\right) \tag{5.8}$$

which is related to the mode temperature T_m by

$$T_m = \frac{n_m\hbar\omega_m}{k_B} \tag{5.9}$$

where k_B is Boltzmann's constant.

The area of the sideband can thus be converted to a mode temperature which is required for a test of classical channel gravity as discussed in the following chapter.

It is also important to check that the power sent to the cavity at its resonant frequency to drive the membrane does not heat the membrane mode temperature. As seen in Fig. 5.10 the mode temperature fluctuates with input power but there is no evidence of mode heating. The fit area is compared to the area below the raw peaks and the error bars are extracted from the difference in these values. Some

peaks shows a larger variation between these values, especially at the lowest drive power resulting in a large variation in error bars.

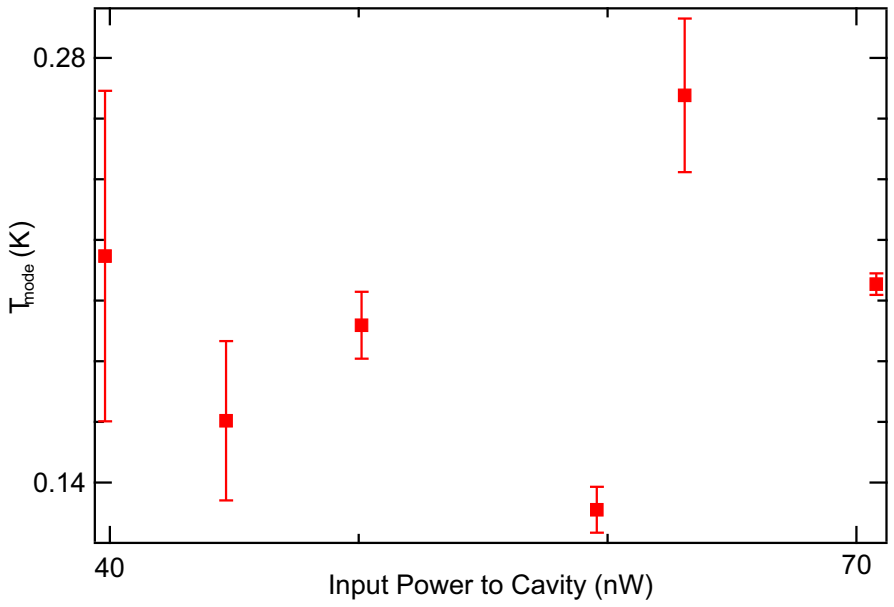


Figure 5.10: Mode temperature of the membrane as a function of input power to the cavity.

5.6 Discussion

In this chapter I have demonstrated a setup that can reach 10 mHz resolution, limited by the measurement time possible before the fridge warms up with the pulse tube turned off. In a wet fridge or a dry fridge shielded from the vibrations of the pulse tube one could achieve higher resolutions. It is clear from my data of the quality factors of both the cavity and the membrane that the cavity and membrane weren't thermalising very well. A reason for this could be that the membrane-antenna chip might not have been tightly clamped to the 3D cavity, resulting in bad thermalisation.

6

A Test of Classical Channel Gravity

Contents

6.1 Gravitation as an Observer of Quantum States 69
6.2 The Predicted Heating Rate of a SiN Membrane . . . 71
6.3 Experimental Results 73
6.4 Estimating the Sensitivity of the Setup 75
6.5 Outlook 77

The theory of classical channel gravity, as will be shown in this chapter, predicts a density dependent heating rate of a silicon nitride membrane, and sensitive measurements of the membrane's mode temperature as a function of the temperature of the environment could be used to put bounds on this prediction. This theory predicts the minimum heating rate. It is clear from the sensitivity estimates of section 6.4 that the minimum predicted heating rate from this theory will not be found with this setup within any reasonable time-span, however the heating rate could be larger than the minimum predicted rate and it is a valuable exercise to aim to begin to put bounds on the theory.

6.1 Gravitation as an Observer of Quantum States

For almost the past 100 years the questions surrounding the boundary of the quantum realm have vexed physicists and philosophers alike [105]. One of these questions is the question of the role of the observer - the observer is supposed to act outside the unitary evolution of quantum systems and have an external influence on results, however one doesn't want to anthropomorphise the theory making the old mistake of assuming that humans lie at the centre of the universe (or in this case the theory). A way around this could be to include gravity in the theory - could gravitational interactions act as an observer?

The question of whether or not gravity has a role to play in quantum mechanics goes back at least to Feynman [106], with new approaches to answering this question being given up to the present day [107]. Kafri, Taylor and Milburn (KTM) have proposed that gravitational interactions could act as classical measurement channels [51], developing proposals by Diósi and Penrose [108–111]. One cannot shield from gravity, and thus any massive object exhibits open measurement channels through its effect on space-time geometry. This distinguishes gravity from all other forces. The measurement channels are a source of decoherence even if the results of the measurements are never known (that is, measured by a measuring apparatus) and thus the gravitational interaction can be thought of as having the same effect as an observer. It should be noted that any system – environment coupling in the Born-Markov approximation can be thought of as an observer however the idea in Ref. [51] is to consider this coupling as a measurement in order to get around quantizing gravity.

In KTM's model gravitational interactions are realised as measurement feed-forward channels. That is, the classical Newtonian potential is the physical channel through which information about a measurement on object A is sent to object B and vice versa. The classical measurement channel is an example of a local operation with classical communication and it cannot entangle the two masses. The term classical channel refers to a channel that cannot be used to entangle systems.

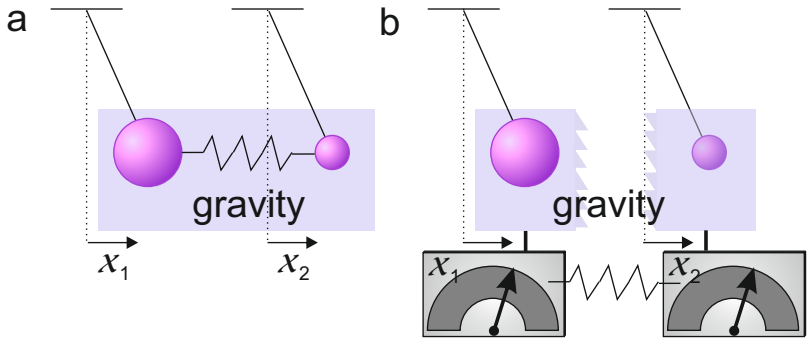


Figure 6.1: (a) A system consisting of two harmonic oscillators entangeld by the gravitational interaction. (b) In classical channel gravity the Newtonian potential effectively measures the position of each mass. In this case gravity acts as an observer which prevents the masses becoming entangled.

This measurements of position carried out via the classical Newtonian potential cause a corresponding back-action force on the momentum of each mass. The measurement results appearing in the gravitational potential effectively result in gravitational interactions plus noise as they modulate a classical stochastic force on all other masses. Decoherence enters the model via two channels: quantum noise on the feed-forward channel due to stochastic measurement noise and via the back-action due to the measurement. Decoherence in the position basis is the first of two (potentially) experimentally detectable signals from this theory. The second is a heating rate as when decoherence is present in position it implies diffusion (heating) in momentum. A heating effect is a common signature of collapse theories, such as the Ghirardi-Rimini-Weber (GRW) theory [39] which evolved into the theory of continuous spontaneous localization (CSL) [112] .

In Ref. [51] two mechanical resonators with the same mass and resonant frequency are considered, and they reduce the model to the case of two quadratically coupled simple harmonic oscillators. The model is in 1D and is linearised about a fixed position. They find that the gravitational decoherence rate for position in natural units is one half of the gravitational heating rate, and also that these parameters are of the order of the normal mode spitting between the two mechanical resonators due to their gravitational coupling. The normal modes consist of the centre of mass mode and the breathing mode of the oscillators. The ability to prepare the ground

state of two normal modes through purely gravitational interactions is a test of gravitational decoherence (assuming no other long range interactions) because such a state is a superposition state of the local modes. An experiment capable of resolving the normal mode splitting (or lack of) is extremely challenging. To make the normal mode splitting as large as possible one needs a material with a large density and low mechanical frequency. The best case scenario considered in Ref. [51] predicts a splitting of 10^{-7} Hz using depleted uranium spheres with a frequency of one Hertz.

In collaboration with Dr Kiran Khosla and Prof. Gerard Milburn, we have found that trying to distinguish the normal mode splitting is not the only way to put the model to the test. We realised that the use of one composite test mass, in place of two masses placed close together, is sufficient. This is because inside the composite test mass one can consider the individual masses of the atoms, and the spacing between atoms within an object is far closer than we could achieve experimentally, albeit with the trade-off that the masses are far lighter. In our case the composite test mass is a silicon nitride membrane.

6.2 The Predicted Heating Rate of a SiN Membrane

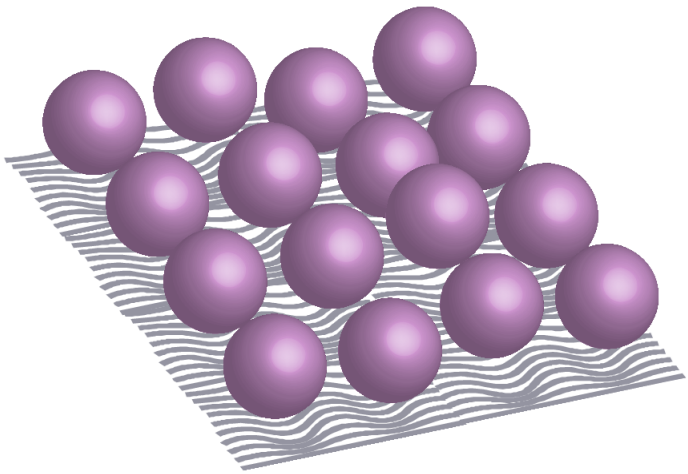


Figure 6.2: In this model, the membrane consists of many masses (atoms) whose positions are measured via the classical gravitational interaction, leading to a heating rate.

In this model each atom in the object interacts with the background Newtonian potential as depicted in Fig. 6.2. In the classical channel description, each atom is effectively measured exactly once in time step dt, and the measurement outcomes modify the global Newtonian potential. This potential acts on all other atoms. Due to the measurements each individual atom undergoes decoherence in the position basis, leading to momentum diffusion (heating). Dr Kiran Khosla calculated the heating rate expected in this case (the derivation is given in appendix B):

The system is modelled as a crystal with a Hamiltonian of atoms with momenta p_i, mass m_i at locations x_i,

$$H = \sum_i \frac{p_i^2}{2m_i} + \frac{m_i\omega_i^2 x_i^2}{2} + \sum_{j\neq i} V_q(x_i, x_j) + V_{ij}x_i x_j, \tag{6.1}$$

where each operator x_i is understood to have zero mean and centred at the point about which the atom is bound. $V_q(x_i, x_j)$ describes any quantum interactions between the atoms (including electron shielding and the Coulomb interactions that hold the atoms in place) and $V_{ij} = 2Gm_im_j/d_{ij}^3$ is the lowest order gravitational interaction between atoms in the crystal separated by mean distance d_{ij}.

The heating rate is calculated by assuming a minimum value for the classical channel measurement rate so the prediction is for the minimum allowable heating rate for the theory. It is also derived assuming one is measuring the fundamental mechanical mode of a crystal of density μ, and in this case it is given by

$$\dot{E} \geq \frac{1}{2}\hbar G\sqrt{S}\mu. \tag{6.2}$$

where $S = \sum_i R_{0i}^2 S_i$ is a dimensionless constant of order unity for a crystal structure that depends on all relative masses $R_{0i} = m/m_i$ and we take $\sqrt{S} = 1$. For a silicon nitride membrane $\mu = 3.44\text{g/cm}^3$ and so we obtain $\dot{E} \geq 1.2 \times 10^{-41}$ W. Although this heating rate is very small, it is a minimum bound and the actual heating rate could be larger than this. It is also worth pointing out that equation 6.2 combines both a quantum fundamental constant $\hbar$ and a gravitational fundamental constant G in one equation.

Another important note is that a different multiparticle heating rate was derived in Ref. [113] and excluded using data from single-atom interference experiments. The authors used the same linearised gravitational interaction, however an important difference is that they assumed each particle is measured separately in pairwise interactions leading to a significantly larger decoherence rate. Therefore the conclusion of the paper, that gravity is not pairwise classical, does not hold for this derivation as a global background potential was assumed in our case, not pairwise interactions.

6.3 Experimental Results

As outlined in chapter 5 my setup can be used to measure the mode temperature of a silicon nitride membrane. The protocols outlined in chapter 5 were carried out at several different mixing chamber temperatures with the aim of putting bounds on the theory of classical channel gravity. The basic idea is that if the heating rate predicted by the theory is present then the membrane should always be slightly hotter than its environment inside the fridge. A graph of the membrane's mode temperature vs the fridge temperature is predicted to have a small non-zero intercept, similar to the work carried out in a different system testing the heating predicted by CSL [45, 46] as discussed in chapter 1.

Figure 6.3 shows the experimental data. It was taken in two separate runs of the experiment (within the same cooldown i.e. without exceeding the superconducting transition temperature of aluminium) and the error bars span the values obtained in these runs. The blue line is a straight line fit ($T_{mode} = a + bT_{MC}$) with parameters $a = 0.26\pm\ 0.05$ and $b = 0.40\pm\ 0.07$. The black dashed line is a guide for the eye with gradient $b = 1$ to show what one would expect if the mode temperature of the membrane was perfectly thermalised, i.e. $\mathrm{T}_{mode} = \mathrm{T}_{MC}$, and no heating was present i.e. $a = 0$. As the gradient is not equal to 1, we can not be certain that the membrane is thermalised or if spurious vibrations from the lab may be affecting T_{mode}, and we can't draw any conclusions about the gravitational heating rate from the value of the intercept. Also, as the error bars are so large for certain points, it strongly

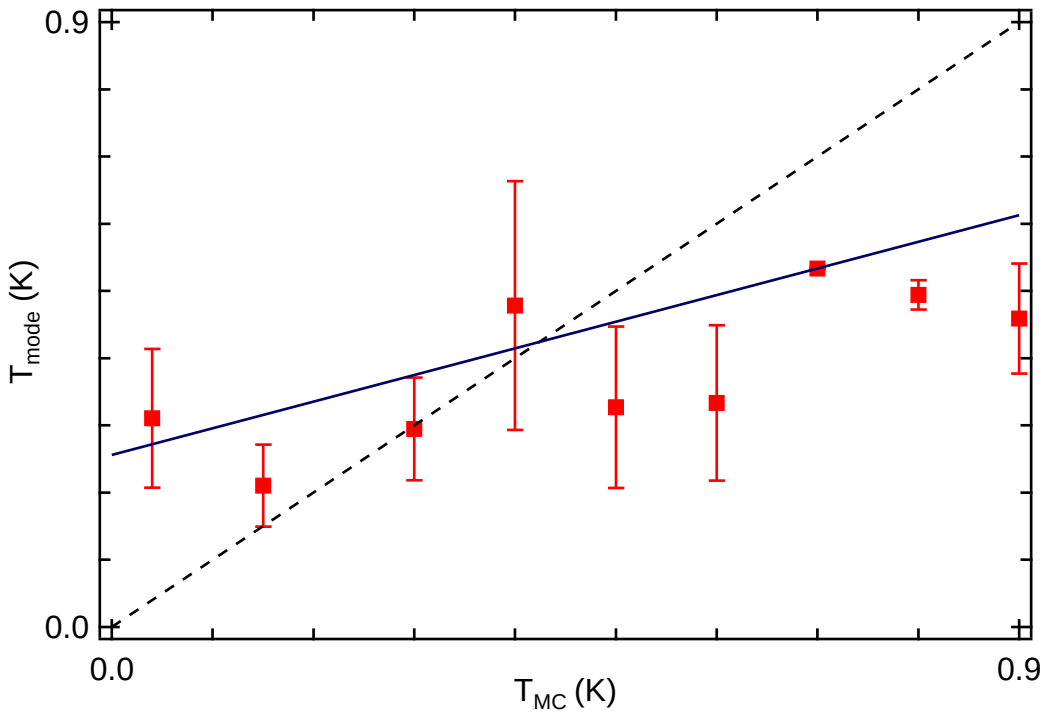


Figure 6.3: Calculated mode temperature of the membrane vs the fridge's mixing chamber temperature (red) with a straight line ($T_{mode} = a + bT_{MC}$) fit (blue). The obtained parameters are a = 0.26 ± 0.05 and b = 0.40 ± 0.07. The black dashed line is a guide for the eye showing $T_{mode} = T_{MC}$. The values are obtained from the average value of two experimental runs (within the same cooldown during which the superconducting transition temperature of the cavity was not exceeded). The error bars span the values obtained in each run.

indicates that the mode temperature of the membrane was indeed not thermalising with the environment or that it was being affected by spurious vibrations in the lab. A further issue is that due to the weak coupling to the cavity and to the mechanics, I was unable to observe optomechanically induced transparency (OMIT). This would have been the optimal way to extract the value of g_0 . In my case g_0 was estimated by assuming perfect thermalisation of each point and taking the average value of g_0 , which allows an estimate of the mode temperature of the membrane to be made but with the large drawback of masking any heating which may be present.

There are a number of reasons as to why my data can not put a bound on the theory. The first is that coupling both to the cavity and to membrane was very small giving a small signal to noise ratio, and not allowing for the observation of OMIT.

The coupling to the cavity could be improved by using longer pins and the coupling to the membrane could be improved by making a device with a smaller gap between the membrane and the antenna. The second is the sensitivity of the setup to external vibrations. As mentioned previously in chapter 5 the signal is vastly amplified not only by the pulse tube of the dilution refrigerator that the experiment is located in, but also by the pulse tubes of the other two dilution refrigerators in the same room. All the mode temperature data in this chapter was taken with all of the pulse tubes turned off but there may well be other noise sources that I have no control over that affect the measurements. I have incorporated a vibration isolation platform into my setup (Fig. 6.4) but I found that the 3D cavity would not superconduct. To overcome this I introduced copper braid to form a thermal link but this reintroduced some of the vibrations from the pulse tube which I wished to shield the device from, and would therefore have also reintroduced any unknown sources of vibrations as well. The third is that I was limited in both the measurement time and the number of averages I could feasibly take by the fact that I had a limited amount of time whilst the pulse tubes were turned off before the fridge would warm up.

6.4 Estimating the Sensitivity of the Setup

During discussions about the experimental setup to be used to test the theory of classical channel gravity, Dr. Edward Laird made an estimation of the sensitivity that the setup described in chapter 5 could achieve.

The detection scheme can be considered as a classical total-power radiometer integrating over a sideband of the cavity drive tone [114]. In the critically coupled good-cavity limit the sideband power, $\mathrm{P_{SB}}$, is [22]:

$$P_{\mathrm{SB}} = P_{\mathrm{in}} \left(\frac{g_0}{\omega_{\mathrm{m}}} \right)^2 \frac{k_{\mathrm{B}} T_{\mathrm{m}}}{2\hbar\omega_{\mathrm{m}}} \tag{6.3}$$

where P_{in} is the cavity drive tone power, ω_{m} the mechanical frequency, T_{m} the mechanical mode temperature and g_0 the single-photon coupling strength. This is equivalent to an effective radiation temperature, averaged over the width γ_{m} of the

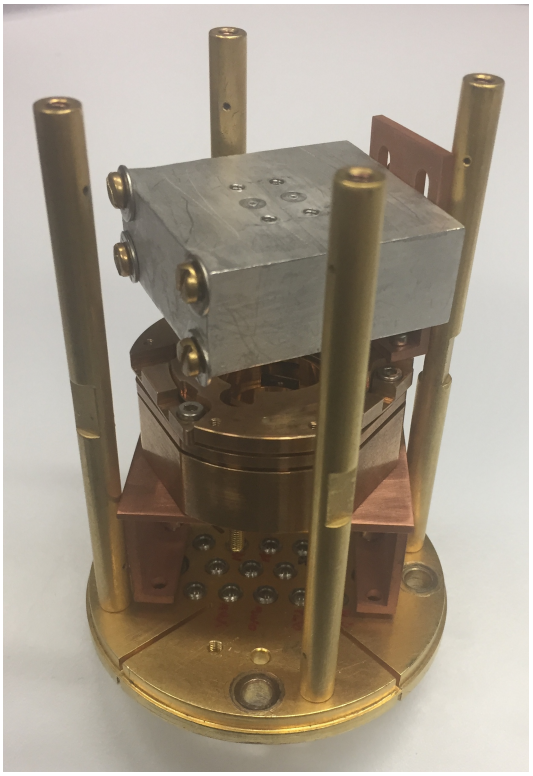


Figure 6.4: Setup showing a cryogenic vibration isolation platform (CVIP) incorporated into the cavity setup with the aim of shielding the membrane from the effect of the pulse tube. The vibration isolation platform is a CVIP purchased from *JPE* and the parts to attach it to the cavity and the puck which the experiment is placed in were designed by me.

sideband, of $T_{\mathrm{ER}} = P_{\mathrm{side}}/k_{\mathrm{B}}\gamma_{\mathrm{m}}$. For typical parameters, T_{ER} is much greater than the noise temperature T_N of the microwave amplifier, so that the radiometer formula gives for the thermodynamic imprecision in the membrane temperature [114, 115]:

$$\Delta T_{\mathrm{m}} = \frac{T_{\mathrm{m}}}{\sqrt{\gamma_{\mathrm{m}}\tau}} \tag{6.4}$$

where τ is the measurement duration and we optimise the radiometer filter bandwidth by setting it equal to the sideband width.

The heating rate predicted by equation 6.2 can be converted to a change in mode temperature via

$$\dot{E} = \gamma_{\mathrm{m}} k_{\mathrm{B}} T_{\mathrm{m}} \tag{6.5}$$

and therefore one can write τ as

$$\tau = \gamma_{\mathrm{m}} \left(\frac{T_m k_{\mathrm{B}}}{\dot{E}} \right)^2 \tag{6.6}$$

For our parameters of $\dot{E} = 1.2 \times 10^{-41}$ W and $\gamma_{\mathrm{m}} = 0.15$ Hz the predicted minimum bound of the change in mode temperature of our silicon nitride membrane is 5.8×10^{-18} K. Assuming a base temperature of 20 mK and that the membrane thermalises to this temperature, to resolve the temperature change with our setup would require a measurement time τ of 7.9×10^{31} s or 2.5×10^{24} years. This is however just the tightest bound the theory predicts and one could improve the experimental setup with a lower environmental temperature or narrower linewdith membrane. (2.5 mHz linewidths have been reported at cryogenic temperatures [3] or even 1.4 mHz linewidths at room temperature [5] with en expected increase in Q factor of 2 orders of magnitude if the membrane were cooled down to cryogenic temperatures.)

6.5 Outlook

This experiment could be made with a critically coupled cavity, and with a stronger coupling to the mechanics. This would give a better signal to noise ratio and would also allow for OMIT measurements to extract the value of g_0 . In addition it could be carried out in a lab with purpose built vibration isolation and ideally in a wet fridge (which does not have a pulse tube) or a dry fridge with shielding from the effect of the pulse tube. This would allow for longer measurement times, giving higher resolution, as the current time is limited by the amount of time the pulse tube can be turned off for several times in a row without the mixing chamber and fridge heating up. It could also allow for more averages to be taken to improve the signal to noise ratio. These improvements might allow a table-top experiment like the one described in this thesis to put a first bound on the theory of classical channel gravity.

7
Conclusion

The briefest summary would simply state that the first question *Do trade-offs pertaining to the thermodynamics of time keeping, derived in the quantum domain, hold for a larger more complex system?* has been answered in the affirmative, whilst the second *Is the gravitational interaction classical rather than quantum?* needs further experimental investigation. However, as with many things in life, it's not just the destination but the journey that counts. Along the journey seeking to answer those two questions a number of things have been demonstrated experimentally. The contributions include the development of an off resonant electromechanical system capable of the estimation of key parameters of a silicon nitride membrane without the need for frequency matching or cryogenic cooling, along with a demonstration of optomechanically induced transparency in a high loss cavity on chip. The design of this system allows for the motion of the membrane to be actuated and the large bandwidth of this cavity allows for real time measurements of the actuated membrane's motion. These measurements enable the system to be operated as a thermomechanical clock for the investigation of a thermodynamic trade-off, previously predicted to hold in the quantum regime. I have shown that this trade-off holds in my system which points toward a universality of this trade-off and corroborates the notion that the quality of the arrow of time, that is, the accuracy at a given resolution with which the passage of time is kept, is indeed determined

by the entropy dissipated by a clock. In addition, my system is compatible with cryogenic temperatures, allowing me to actuate and detect the resonance frequency of a membrane at low temperatures. A further contribution is that with close collaboration with theorists my project has developed a bench top test with the aim of putting bounds on the theory of classical channel gravity. A development from the original theory paper [51] is the realisation that it is sufficient to use one test mass, such as a silicon nitride membrane, not two as previously thought in order to test the theory. Using a cavity microwave optomechanical system [22], along with a multi-step demodulation circuit I have achieved 10 mHz resolution of the mechanical signal (limited only by the measurement time during which the pulse tubes had to be turned off to limit vibrations; in a wet fridge my setup would be capable of resolving the signal to an even higher precision) which is required for an accurate estimation of the mode temperature.

Thinking to where this might lead there are a number of avenues which could be pursued. The first and most obvious one is to redo the gravitational experiment in an environment which is fully shielded from external vibrations, along with stronger coupling both to the cavity and to the mechanics. This would allow for the peak to be resolved more clearly with a better signal to noise ratio, and as mentioned the limitations in measurement time could be circumvented by the use of a wet fridge or a dry fridge with appropriate vibration isolation. The stronger coupling to the cavity would also allow for OMIT measurements to be taken at different temperatures to measure the coupling strength of the mechanics. With these improvements one could put the first experimental bounds on the theory of classical channel gravity.

The on chip rf optomechanical system I have developed allows for many cavities to couple severalmechanical resonators. It would certainly be feasible to explore multimode optomechanics both for different cavity modes and different mechanical modes provided the membranes were designed to have different natural frequencies. A direction that it may be possible to investigate with a multi-membrane system is if two correlated clocks give better or worse performance than two uncorrelated clocks.

Thinking of further thermodynamical investigation, provided I could shield the membrane from external vibrations it would be possible to evaluate the amplitude fluctuations of the membrane driven with white noise and interpret it as an engine rather than as a clock.

Coming in to land, here concludes the small step taken along the extensive path of scientific discovery. One question answered, and a remaining experimental challenge for myself or perhaps a motivated reader. Thank you for reading!

Appendices

A

Extraction of g_0 from Thermomechanical Sidebands: Theory

(This calculation is published in the supplementary information of Ref [71].)

This section derives the expression relating g_0 to the effective thermomechanical power (P_{SB}) extracted from the area of the sideband. Starting with $g_0/2\pi = \frac{df_{\mathrm{C}}}{du} u_{\mathrm{ZP}} = \frac{\partial f_{\mathrm{C}}}{\partial C_{\mathrm{T}}} \frac{\partial C_{\mathrm{C}}}{\partial u} u_{\mathrm{ZP}}$ and using $\frac{\partial f_{\mathrm{C}}}{\partial C_{\mathrm{T}}} \approx (4\pi\sqrt{LC_{\mathrm{T}}^3})^{-1}$ one obtains

$$g_0/2\pi \approx (4\pi\sqrt{LC_{\mathrm{T}}^3})^{-1} \frac{\partial C_{\mathrm{C}}}{\partial u} u_{\mathrm{ZPM}}, \tag{A.1}$$

where $u_{\mathrm{ZPM}} = \sqrt{\hbar/(4\pi m f_{i,j})}$ is the zero point motion of the membrane with effective mass $m \sim 4.5 \times 10^{-10}$ kg. We choose to normalize the mode eigenfunctions such that the effective mass equals the mass of the suspended segment for all modes [12]. The value of L is known, C_{T} is obtained from the circuit model fit and u_{ZPM} can be estimated from the values of $f_{i,j}$ extracted from the Lorentzian fit of the mechanical sidebands. To estimate $\frac{\partial C_{\mathrm{C}}}{\partial u}$, we write P_{SB}, which obeys

$$P_{\mathrm{SB}} = \tilde{P}_{\mathrm{C}}\ 2\bar{n}_{\mathrm{i,j}} \left(\frac{\kappa_e}{\kappa}\right)^2 \frac{g_0^2}{(\frac{\kappa}{2})^2 + (2\pi f_{i,j})^2}, \tag{A.2}$$

where $\tilde{P}_{\rm C}$ is the cavity drive $P_{\rm C}$ having taken into account the overall insertion loss and $\bar{n}_{\rm i,j}$ is the phonon occupancy of the mode [22]. Replacing g_0^2 with Eq. (A.1),

$$P_{\rm SB} \approx \tilde{P}_{\rm C}\ 2\bar{n}_{\rm i,j} \left(\frac{\kappa_e}{\kappa}\right)^2 \frac{\left(\frac{\partial C_{\rm C}}{\partial u}\right)^2 u_{\rm ZPM}^2}{((\frac{\kappa}{2})^2 + (2\pi f_{i,j})^2)(2\sqrt{LC_{\rm T}^3})^2}. \tag{A.3}$$

The values of κ and κ_e are obtained from the cavity characterization.

We now write $\bar{n}_{\rm i,j}$,

$$\bar{n}_{\rm i,j} = \frac{m\ (2\pi f_{i,j})^2 \langle \delta u_{\rm i,j}^2 \rangle}{\hbar\ (2\pi f_{i,j})}, \tag{A.4}$$

where $\delta u_{\rm i,j}$ is the membrane displacement from its equilibrium position. In order to estimate the rms value $\langle \delta u_{\rm i,j}^2 \rangle$, we write the effective electromechanical force on the membrane,

$$F(t) = \frac{1}{2} V^2(t) \frac{\partial C_C}{\partial u}, \tag{A.5}$$

where $V(t) = V_{\rm dc} + \delta V(t)$. The time-independent part $V_{\rm dc} = 15$ V is much larger than the time-dependent part $\delta V(t)$. The time-dependent part of $F(t)$ is to lowest order

$$\delta F(t) = V_{\rm dc} \frac{\partial C_C}{\partial u} \delta V(t), \tag{A.6}$$

where we assumed this electronic fluctuating force is much larger than the thermal noise.

In the frequency domain, the displacement is

$$\delta u_{\rm i,j}(f) = \chi_{\rm i,j}(f) \delta F(f), \tag{A.7}$$

where the mechanical susceptibility is $\chi_{\rm i,j}(f) = \frac{1}{4\pi^2 m}[f_{i,j}^2 - f^2 + i f f_{i,j}/Q_{\rm i,j}]^{-1}$ [1, 72]. The values of $Q_{\rm i,j}$ can be extracted from the Lorentzian fit of the mechanical sidebands. We calculate $[\delta u_{\rm i,j}^2]_{\rm rms}$,

$$[\delta u_{\rm i,j}^2]_{\rm rms} = V_{\rm dc}^2 \left(\frac{\partial C_{\rm C}}{\partial u}\right)^2 \int_{-\infty}^{\infty} \int_{-\infty}^{\infty} df df' \langle \delta V(f) \delta V(f') \rangle \langle \chi_{\rm i,j}(f) \chi_{\rm i,j}(f') \rangle, \tag{A.8}$$

where $\chi_{\mathrm{i,j}}(f)$ and $\delta V(f)$ are uncorrelated. The fluctuating voltage $\delta V(f)$ is assumed to be well approximated by white noise over the frequency range of interest, with $\langle \delta V(f)\delta V(f')\rangle = \frac{S_V^2}{2}\ \delta(f+f')$, where S_V is the single-sided white noise power spectrum of the driving voltage V. We obtain

$$[\delta u_{\mathrm{i,j}}^2]_{\mathrm{rms}} = V_{\mathrm{dc}}^2 \left(\frac{\partial C_{\mathrm{C}}}{\partial u}\right)^2 \left(\int_0^\infty df |\chi_{\mathrm{i,j}}(f)|^2\right) \frac{S_V^2}{2}, \tag{A.9}$$

given that $\chi_{\mathrm{i,j}}(f)^* = \chi_{\mathrm{i,j}}(-f)$.

We can now rewrite Eq. A.4,

$$\bar{n}_{\mathrm{i,j}} = m(2\pi f_{i,j}/\hbar)\ V_{\mathrm{dc}}^2 \left(\frac{\partial C_{\mathrm{C}}}{\partial u}\right)^2 \frac{S_V^2}{2} \int df |\chi_{\mathrm{i,j}}(f)|^2. \tag{A.10}$$

Replacing Eq. A.10 in Eq. A.2, we obtain the following expression,

$$\frac{\partial C_{\mathrm{C}}}{\partial u} = \sqrt[4]{\frac{P_{\mathrm{SB}}}{\tilde{P}_{\mathrm{C}}} \left(\frac{\kappa}{\kappa_e}\right)^2 \frac{((\frac{\kappa}{2})^2 + (2\pi f_{i,j})^2)(2LC_{\mathrm{T}}^3)}{V_{\mathrm{dc}}^2\ \frac{S_V^2}{2} \int_0^\infty df |\chi_{i,j}(f)|^2}}. \tag{A.11}$$

With the amplitude of the driving noise set to $\mathrm{V_{WN}} = 2.7\ \mathrm{V_{rms}}$, the corresponding spectral density is measured as $S_V^2 = (3 \pm 0.1) \times 10^{-10}\ \mathrm{V^2/Hz}$ and we calculate $\int_0^\infty df |\chi_{\mathrm{i,j}}(f)|^2$ numerically. Once we estimate $\frac{\partial C_{\mathrm{C}}}{\partial u}$, Eq. A.1 gives us g_0 for each observed mechanical mode. The error in this quantity reflects uncertainty in the cavity characterization (κ and κ_e), the circuit model fit (C_{T}), the measurement of S_V^2, P_{SB} and the fit of the mechanical sidebands ($f_{i,j}$ and $Q_{\mathrm{i,j}}$).

B

Derivation of the Heating Rate of a Silicon Nitride Membrane

This derivation was carried out by Dr Kiran Khosla under the supervision of Prof. Gerard Milburn. It is included here for completeness, and with permission.

The system is modelled as a crystal with the Hamiltonian of atoms with momenta p_i, mass m_i at locations x_i,

$$H = \sum_i \frac{p_i^2}{2m_i} + \frac{m_i\omega_i^2 x_i^2}{2} + \sum_{j\neq i} V_q(x_i, x_j) + V_{ij}x_i x_j, \tag{B.1}$$

where each operator x_i is understood to have zero mean and centered at the point about which the atom is bound. $V_q(x_i, x_j)$ describes any quantum interactions between the atoms (including electron shielding) and $V_{ij} = 2Gm_im_j/d_{ij}^3$ is the lowest order gravitational interaction between atoms in the crystal separated by mean distance d_{ij}. Following the work done in Ref. [51], the gravitational interaction Hamiltonian H_{grav} can be generated by measurements of x_i, which have measurement results $\bar{x}_i$. The feedback control Hamiltonian is $H_{\text{fb}} = \sum_{ij} \frac{1}{2} V_{ij} x_i \bar{x}_j$. The multiparticle master equation for a classical channel model of gravity is derived from continuous quantum measurement and feedback control [116]. The position of each particle is continuously measured leading resulting in the stochastic master

equation [117],

$$\begin{aligned} d\rho_c &= -\frac{idt}{\hbar}[H_q, \rho_c] - \sum_{i=1}^{N} \frac{\Gamma_i dt}{2\hbar}[x_i, [x_i, \rho_c]] \\ &\quad + \sqrt{\frac{\Gamma_i}{\hbar}} dW_i [x_i \rho_c + \rho_c x_i - 2\langle x_i \rangle_c \rho_c] \end{aligned} \tag{B.2}$$

which is conditioned (subscript c) on the N measurement currents

$$dJ_i = \langle x_i \rangle_c dt + \sqrt{\frac{\hbar}{2\Gamma_i}} dW_i. \tag{B.3}$$

Here dW is the standard Wiener increment satisfying $\mathcal{E}(dW) = 0$ and $dW^2 = dt$ where $\mathcal{E}(\cdot)$ denotes the ensemble average over the noise process. The measurement currents are then used to control a feedback Hamiltonian

$$H_{\rm fb} = \sum_{ij} V_{ij} x_j \frac{dJ_i}{dt} \tag{B.4}$$

which is applied immediately after the measurement,

$$\rho_c(t + dt) = e^{-iH_{\rm fb}dt/\hbar}(\rho_c(t) + d\rho_c)e^{iH_{\rm fb}dt/\hbar}. \tag{B.5}$$

Expanding to first order in dt (second order in dW) gives the conditional master equation

$$\begin{aligned} \rho_c(t + dt) &= \rho_c - \frac{idt}{\hbar}[H_q + \sum_{ij} V_{ij} x_i x_j, \rho_c] \\ &\quad - dt \sum_i \left(\frac{\Gamma_i}{2\hbar} + \sum_{j \neq i} \frac{V_{ij}^2}{8\hbar\Gamma_j} \right) [x_i, [x_i, \rho]] \\ &\quad + \sum_k \sqrt{\frac{\Gamma_k}{\hbar}} dW_k [x_k \rho_c + \rho_c x_k - 2\langle x_k \rangle_c \rho_c] \end{aligned} \tag{B.6}$$

in Ito form. An observer unaware of the measurement current will see the ensemble averaged (unconditional) state $d\rho = \mathcal{E}(d\rho_c)$ resulting in the unconditional master equation,

$$\begin{aligned} \frac{d\rho}{dt} &= -\frac{i}{\hbar}[H_q + H_{\rm grav}, \rho] \\ &\quad - \sum_i \left(\frac{\Gamma_i}{2\hbar} + \sum_{j \neq i} \frac{G^2 m_i^2 m_j^2}{d_{ij}^6} \frac{1}{8\hbar\Gamma_j} \right) [x_i, [x_i, \rho]] \end{aligned} \tag{B.7}$$

where Γ_i is the measurement rate of the ith atom's position and H_q (H_{grav}) describes the quantum (linearised gravitational) interactions.

The structure of the decoherence terms in (B.7) can be intuitively understood; as Γ_i becomes large, the measurement backaction dominates the decoherence, while if Γ_i is too small, the classical fluctuations in H_{fb} dominate the decoherence. Since Γ_i characterizes the measurement strength, we propose that Γ_i is proportional to m_i as is the case for (CSL) [38, 40]. Furthermore we note that without the feedback term, the dynamics of Eq. (B.7) are equivalent to Ghirardi-Rimini-Weber (GRW) spontaneous position localization [39]. Taking the mass proportional measurement strength $\Gamma_i = \Gamma_0 m_i$, the heating rate of the ith atom is

$$\dot{E}_i = \text{Tr}[\frac{p_i^2}{2m_i}\dot{\rho}] = \frac{\Gamma_0\hbar}{2} + \frac{G^2 m_i \hbar}{8\Gamma_0}\sum_{j\neq i}\frac{m_j}{d_{ij}^6}. \tag{B.8}$$

The d^{-6} scaling strongly suppresses heating from distant particles, therefore, to a very good approximation, every particle ~ 3 cells deep in the crystal sees the same heating as if it were in an infinitely large crystal. This can be seen by the radial volume scaling $r^2 dr$, giving an overall dr/r^4 scaling for the sum. The sum in Eq. (B.8) can be recast as a dimensionless factor that depends only on the crystal structure,

$$\frac{G^2\hbar m_i}{8\Gamma_0}\sum_{j\neq i}\frac{m_j}{d_{ij}^6} = \frac{G^2\hbar m_i^2}{8\Gamma_0 a^6}\sum_{j\neq i}\frac{R_{ji}}{q_{ij}} = \frac{G^2\hbar m_i^2}{8\Gamma_0 a^6}S_i \tag{B.9}$$

where $R_{ji} = m_j/m_i$ is the ratio of masses, q_{ij} is the dimensionless lattice coordinate pointing from atom i to atom j, and a is the lattice constant of the unit cell. The dimensionless constant S_i can be computed numerically using the "infinite lattice" approximation for a given crystal. The total heating rate is

$$\dot{E}_{\text{tot}} = \frac{\Gamma_0\hbar N}{2} + \frac{G^2\hbar}{8\Gamma_0 a^6}Nm^2 S \tag{B.10}$$

where N is the number of atoms, m is the average mass of the unit cell and $S = \sum_i R_{0i}^2 S_i$ is a dimensionless constant that depends on all relative masses $R_{0i} = m/m_i$. The heating rate is minimized when $\Gamma_0 = Gm\sqrt{S}/2a^3$, giving the minimum heating rate allowable from a classical channel model of gravity of

$$\dot{E}_{\text{min}} = \frac{\hbar G N m\sqrt{S}}{2a^3} \tag{B.11}$$

where m/a^3 is the mass density and Nm is the total mass. The form of Eq. (B.7) shows the energy is distributed (almost) evenly between all atoms in the crystal and therefore the energy is distributed evenly between all normal modes of the crystal. This holds for the centre of mass motion of the fundamental mode where the mode mass is of the order of the total mass. The minimum heating rate of the fundamental mode for a crystal of density μ, as given in the main text of chapter 6 is therefore

$$\dot{E} \geq \frac{1}{2}\hbar G\sqrt{S}\mu. \tag{B.12}$$

References

[1] Markus Aspelmeyer, Tobias J. Kippenberg, and Florian Marquardt. "Cavity optomechanics". In: *Reviews of Modern Physics* 86.4 (2014), pp. 1391–1452. DOI: 10.1103/RevModPhys.86.1391.

[2] Florian Elste, S. M. Girvin, and A. A. Clerk. "Quantum noise interference and backaction cooling in cavity nanomechanics". In: *Physical Review Letters* 102.20 (2009), pp. 1–4. DOI: 10.1103/PhysRevLett.102.207209.

[3] Mingyun Yuan, Martijn A Cohen, and G A Steele. "Silicon nitride membrane resonators at millikelvin temperatures with quality factors exceeding 10^8". In: *Applied Physics Letters* 107.26 (2015), p. 263501. DOI: 10.1063/1.4938747.

[4] Christoph Reinhardt et al. "Ultralow-noise SiN trampoline resonators for sensing and optomechanics". In: *Physical Review X* 6.2 (2016), p. 021001. DOI: 10.1103/PhysRevX.6.021001.

[5] Richard A Norte, João P Moura, and Simon Grőblacher. "Mechanical resonators for quantum optomechanics experiments at room temperature". In: *Physical review letters* 116.14 (2016), p. 147202. DOI: 10.1103/PhysRevLett.116.147202.

[6] T P Purdy, R W Peterson, and C A Regal. "Observation of Radiation Pressure Shot Noise on a Macroscopic Object". In: *Science* 339.6121 (2013), pp. 801–804. DOI: 10.1126/science.1231692.

[7] T P Purdy et al. "Strong optomechanical squeezing of light". In: *Phys. Rev. X* 3.3 (2013), p. 031012. DOI: 10.1103/PhysRevX.3.031012.

[8] JM Fink et al. "Efficient microwave frequency conversion mediated by the vibrational motion of a silicon nitride nanobeam oscillator". In: *arXiv preprint arXiv:1911.12450* (2019).

[9] R W Andrews et al. "Bidirectional and efficient conversion between microwave and optical light". In: *Nature Phys.* 10.4 (2014), pp. 321–326. DOI: 10.1038/nphys2911.

[10] Tolga Bagci et al. "Optical detection of radio waves through a nanomechanical transducer". In: *Nature* 507.7490 (2014), pp. 81–85. DOI: 10.1038/nature13029.

[11] I. Moaddel Haghighi et al. "Sensitivity-Bandwidth Limit in a Multimode Optoelectromechanical Transducer". In: *Phys. Rev. Appl.* 9.3 (2018), p. 34031. DOI: 10.1103/PhysRevApplied.9.034031.

[12] Menno Poot, Herre S J Van Der Zant, and G E W Bauer. "Mechanical systems in the quantum regime". In: *Physics Reports* 511 (2012), pp. 273–335. DOI: 10.1016/j.physrep.2011.12.004.

[13] A D O'Connell et al. "Quantum ground state and single-phonon control of a mechanical resonator." In: *Nature* 464.7289 (2010), pp. 697–703. DOI: 10.1038/nature08967.

[14] K R Brown et al. "Passive cooling of a micromechanical oscillator with a resonant electric circuit." In: *Physical Review Letters* 99.13 (2007), p. 137205. DOI: 10.1103/PhysRevLett.99.137205.

[15] Johannes M Fink et al. "Quantum electromechanics on silicon nitride nanomembranes". In: *Nature communications* 7.1 (2016), pp. 1–10. DOI: 10.1038/ncomms12396.

[16] J. D. Teufel, C. A. Regal, and K. W. Lehnert. "Prospects for cooling nanomechanical motion by coupling to a superconducting microwave resonator". In: *New Journal of Physics* 10 (2008). DOI: 10.1088/1367-2630/10/9/095002.

[17] T. J. Kippenberg and K. J. Vahala. "Cavity optomechanics: back-action at the mesoscale." In: *Science (New York, N.Y.)* 321.5893 (2008), pp. 1172–6. DOI: 10.1126/science.1156032.

[18] C A Regal, J D Teufel, and K W Lehnert. "Measuring nanomechanical motion with a microwave cavity interferometer". In: *Nature Physics* 4.7 (2008), pp. 555–560. DOI: 10.1038/nphys974.

[19] J D Teufel et al. "Dynamical backaction of microwave fields on a nanomechanical oscillator". In: *Physical Review Letters* 101.19 (2008). DOI: 10.1103/PhysRevLett.101.197203.

[20] T Rocheleau et al. "Preparation and detection of a mechanical resonator near the ground state of motion." In: *Nature* 463.7277 (2010), pp. 72–75. DOI: 10.1038/nature08681.

[21] J D Teufel et al. "Sideband cooling of micromechanical motion to the quantum ground state." In: *Nature* 475.7356 (2011), pp. 359–363. DOI: 10.1038/nature10261.

[22] Mingyun Yuan et al. "Large cooperativity and microkelvin cooling with a three-dimensional optomechanical cavity". In: *Nat. Commun.* 6 (2015), p. 8491. DOI: 10.1038/ncomms9491.

[23] Atsushi Noguchi et al. "Ground state cooling of a quantum electromechanical system with a silicon nitride membrane in a 3D loop-gap cavity". In: *New Journal of Physics* 18.10 (2016), p. 103036. DOI: 10.1088/1367-2630/18/10/103036.

[24] Andreas Sawadsky et al. "Observation of generalized optomechanical coupling and cooling on cavity resonance". In: *Physical Review Letters* 114.4 (2015). DOI: 10.1103/PhysRevLett.114.043601.

[25] Talitha Weiss, Christoph Bruder, and Andreas Nunnenkamp. "Strong-coupling effects in dissipatively coupled optomechanical systems". In: *New Journal of Physics* 15.15 (2013), pp. 45017–45017. DOI: 10.1088/1367-2630/15/4/045017.

[26] A. D. Armour, M. P. Blencowe, and K. C. Schwab. "Entanglement and Decoherence of a Micromechanical Resonator via Coupling to a Cooper-Pair Box". In: *Physical Review Letters* 88.14 (2002), p. 148301. DOI: 10.1103/PhysRevLett.88.148301.

[27] Kiran E Khosla et al. "Displacemon electromechanics: how to detect quantum interference in a nanomechanical resonator". In: *Physical Review X* 8.2 (2018), p. 021052. DOI: 10.1103/PhysRevX.8.021052.

[28] William Marshall et al. "Towards Quantum Superpositions of a Mirror". In: *Physical Review Letters* 91.13 (2003), p. 130401. DOI: 10.1103/PhysRevLett.91.130401.

[29] O Romero-Isart et al. "Large quantum superpositions and interference of massive nanometer-sized objects". In: *Physical Review Letters* 107.2 (2011), p. 020405. DOI: 10.1103/PhysRevLett.107.020405.

[30] Brian Pepper et al. "Optomechanical superpositions via nested interferometry". In: *Physical Review Letters* 109.2 (2012), p. 023601. DOI: 10.1103/PhysRevLett.109.023601.

[31] Brian Pepper et al. "Macroscopic superpositions via nested interferometry: Finite temperature and decoherence considerations". In: *New Journal of Physics* 14 (2012). DOI: 10.1088/1367-2630/14/11/115025.

[32] Uzma Akram, Warwick P Bowen, and G J Milburn. "Entangled mechanical cat states via conditional single photon optomechanics". In: *New Journal of Physics* 15.15 (2013). DOI: 10.1088/1367-2630/15/9/093007.

[33] Huatang Tan et al. "Generation of macroscopic quantum superpositions of optomechanical oscillators by dissipation". In: *Physical Review A* 88.2 (2013). DOI: 10.1103/PhysRevA.88.023817.

[34] Jie Qiao Liao et al. "Enhancement of mechanical effects of single photons in modulated two-mode optomechanics". In: *Physical Review A* 92.1 (2015). DOI: 10.1103/PhysRevA.92.013822.

[35] Jie Qiao Liao and Lin Tian. "Macroscopic Quantum Superposition in Cavity Optomechanics". In: *Physical Review Letters* 116.16 (2016). DOI: 10.1103/PhysRevLett.116.163602.

[36] Eun Jong Kim, J. R. Johansson, and Franco Nori. "Circuit analog of quadratic optomechanics". In: *Physical Review A* 91.3 (2015). DOI: 10.1103/PhysRevA.91.033835.

[37] J. R. Johansson, G Johansson, and Franco Nori. "Optomechanical-like coupling between superconducting resonators". In: *Physical Review A* 90.5 (2014). DOI: 10.1103/PhysRevA.90.053833.

[38] Gian Carlo Ghirardi, Philip Pearle, and Alberto Rimini. "Markov processes in Hilbert space and continuous spontaneous localization of systems of identical particles". In: *Physical Review A* 42.1 (1990), pp. 78–89. DOI: 10.1103/PhysRevA.42.78.

[39] G C Ghirardi, A Rimini, and T. Weber. "Unified dynamics for microscopic and macroscopic systems". In: *Physical Review D* 34.2 (1986), pp. 470–491. DOI: 10.1103/PhysRevD.34.470.

[40] Angelo Bassi et al. "Models of wave-function collapse, underlying theories, and experimental tests". In: *Reviews of Modern Physics* 85.2 (2013), pp. 471–527. DOI: 10.1103/RevModPhys.85.471.

[41] Stephen L Adler. "Lower and upper bounds on CSL parameters from latent image formation and IGM heating". In: *Journal of Physics A: Mathematical and Theoretical* 40.12 (2007), pp. 2935–2957. DOI: 10.1088/1751-8113/40/12/S03.

[42] M. Bahrami et al. "Proposal for a Noninterferometric Test of Collapse Models in Optomechanical Systems". In: *Physical Review Letters* 112.21 (2014), p. 210404. DOI: 10.1103/PhysRevLett.112.210404.

[43] Stefan Nimmrichter, Klaus Hornberger, and Klemens Hammerer. "Optomechanical Sensing of Spontaneous Wave-Function Collapse". In: *Physical Review Letters* (2014). DOI: 10.1103/PhysRevLett.113.020405.

[44] Lajos Diósi. "Testing Spontaneous Wave-Function Collapse Models on Classical Mechanical Oscillators". In: *Physical Review Letters* (2015). DOI: 10.1103/PhysRevLett.114.050403.

[45] A. Vinante et al. "Upper Bounds on Spontaneous Wave-Function Collapse Models Using Millikelvin-Cooled Nanocantilevers". In: *Physical Review Letters* 116.9 (2016), pp. 1–5. DOI: 10.1103/PhysRevLett.116.090402.

[46] A Vinante et al. "Improved Noninterferometric Test of Collapse Models Using Ultracold Cantilevers". In: *Physical Review Letters* 119.11 (2017), p. 110401. DOI: 10.1103/PhysRevLett.119.110401.

[47] Daniel Goldwater, Mauro Paternostro, and P F Barker. "Testing wave-function-collapse models using parametric heating of a trapped nanosphere". In: *Physical Review A* 94.1 (2016), p. 010104. DOI: 10.1103/PhysRevA.94.010104.

[48] Ying Li et al. "Detecting continuous spontaneous localization with charged bodies in a Paul trap". In: *Physical Review A* 95.3 (2017), p. 032112. DOI: 10.1103/PhysRevA.95.032112.

[49] Sayantani Bera et al. "A proposal for the experimental detection of CSL induced random walk." en. In: *Scientific Reports* 5 (2015), p. 7664. DOI: 10.1038/srep07664.

[50] Stefan Forstner et al. "Testing collapse mechanisms with high frequency quantum optomechanics". In: *arXiv preprint arXiv:1909.01608* (2019).

[51] D. Kafri, J. M. Taylor, and G. J. Milburn. "A classical channel model for gravitational decoherence". In: *New Journal of Physics* 16 (2014), pp. 1–11. DOI: 10.1088/1367-2630/16/6/065020.

[52] Alejandro W Rodriguez, Federico Capasso, and Steven G Johnson. "The Casimir effect in microstructured geometries". In: *Nature Photonics* 5 (2011), pp. 211–221. DOI: 10.1038/nphoton.2011.39.

[53] Daniel Garcia-Sanchez et al. "Casimir probe based upon metallized high Q SiN nanomembrane resonator". In: *Review of Scientific Instruments* 84.1 (2013). DOI: 10.1063/1.4774396.

[54] R L Jaffe. "Casimir effect and the quantum vacuum". In: *Physical Review D* 72.2 (2005), p. 021301. DOI: 10.1103/PhysRevD.72.021301.

[55] Hrvoje Nikolic. "Proof that Casimir force does not originate from vacuum energy". In: *Physics Letters, Section B* 761 (2016), pp. 197–202. DOI: 10.1016/j.physletb.2016.08.036.

[56] J. R. Johansson et al. "Dynamical casimir effect in a superconducting coplanar waveguide". In: *Physical Review Letters* 103.14 (2009), pp. 1–4. DOI: 10.1103/PhysRevLett.103.147003.

[57] J. R. Johansson et al. "Dynamical Casimir effect in superconducting microwave circuits". In: *Physical Review A* 82.5 (2010), p. 52509. DOI: 10.1103/PhysRevA.82.052509.

[58] Pasi Lähteenmäki et al. "Dynamical Casimir effect in a Josephson metamaterial." In: *Proceedings of the National Academy of Sciences* 110.11 (2013), pp. 4234–4238. DOI: 10.1073/pnas.1212705110.

[59] James Q Quach. "Gravitational casimir effect". In: *Physical Review Letters* 114.8 (2015), p. 081104. DOI: 10.1103/PhysRevLett.114.081104.

[60] Richard A Norte et al. "Platform for measurements of the Casimir force between two superconductors". In: *Physical Review Letters* 121.3 (2018), p. 030405. DOI: 10.1103/PhysRevLett.121.030405.

[61] Wolfram H.P. Pernice et al. "Analysis of short range forces in opto-mechanical devices with a nanogap". In: *Opt. Express* 18.12 (2010), pp. 12615–12621. DOI: 10.1364/OE.18.012615.

[62] Yutian Wen et al. "Measuring carbon nanotube vibrations using a single-electron transistor as a fast linear amplifier". In: *Applied Physics Letters* 113.15 (2018), p. 153101. DOI: 10.1063/1.5052185.

[63] D. F. Walls. "Squeezed states of light". In: *Nature* 306.5939 (1983), pp. 141–146. DOI: 10.1038/306141a0.

[64] R E Slusher et al. "Observation of squeezed states generated by four-wave mixing in an optical cavity". In: *Physical Review Letters* 55.22 (1985), pp. 2409–2412. DOI: 10.1103/PhysRevLett.55.2409.

[65] M. P. Blencowe and M. N. Wybourne. "Quantum squeezing of mechanical motion for micron-sized cantilevers". In: *Physica B: Condensed Matter* 280.1-4 (2000), pp. 555–556. DOI: 10.1016/S0921-4526(99)01862-1.

[66] Andreas Kronwald, Florian Marquardt, and Aashish A Clerk. "Arbitrarily large steady-state bosonic squeezing via dissipation". In: *Physical Review A* 88.6 (2013). DOI: 10.1103/PhysRevA.88.063833.

[67] Huatang Tan, Gaoxiang Li, and P Meystre. "Dissipation-driven two-mode mechanical squeezed states in optomechanical systems". In: *Physical Review A* 87.3 (2013). DOI: 10.1103/PhysRevA.87.033829.

[68] J. M. Pirkkalainen et al. "Squeezing of Quantum Noise of Motion in a Micromechanical Resonator". In: *Physical Review Letters* 115.24 (2015). DOI: 10.1103/PhysRevLett.115.243601.

[69] F Lecocq et al. "Quantum Nondemolition Measurement of a Nonclassical State of a Massive Object". In: *Physical Review X* 5.4 (2015), p. 041037. DOI: 10.1103/PhysRevX.5.041037.

[70] C F Ockeloen-Korppi et al. "Stabilized entanglement of massive mechanical oscillators". In: *Nature* 556 (2018), pp. 478–482. DOI: 10.1038/s41586-018-0038-x.

[71] AN Pearson et al. "Radio-frequency optomechanical characterization of a silicon nitride drum". In: *Scientific reports* 10.1 (2020), p. 1654. DOI: https://doi.org/10.1038/s41598-020-58554-x.

[72] Konrad W Lehnert. "Introduction to Microwave Cavity Optomechanics". In: *Cavity Optomechanics*. Springer, 2014, pp. 233–252. DOI: 10.1007/978-3-642-55312-7_11.

[73] N Ares et al. "Resonant Optomechanics with a Vibrating Carbon Nanotube and a Radio-Frequency Cavity". In: *Phys. Rev. Lett.* 117.17 (2016), p. 170801. DOI: 10.1103/PhysRevLett.117.170801.

[74] T Faust et al. "Microwave cavity-enhanced transduction for plug and play nanomechanics at room temperature". In: *Nature Communications* 3 (2012). DOI: 10.1038/ncomms1723.

[75] V. Singh et al. "Optomechanical coupling between a multilayer graphene mechanical resonator and a superconducting microwave cavity". In: *Nature Nanotechnology* 9.10 (2014), pp. 820–824. DOI: 10.1038/nnano.2014.168.

[76] Fred Lacy. "Developing a theoretical relationship between electrical resistivity, temperature, and film thickness for conductors". In: *Nanoscale Research Letters* 6 (2011), pp. 1–26. DOI: 10.1186/1556-276X-6-636.

[77] N Ares et al. "Sensitive radio-frequency measurements of a quantum dot by tuning to perfect impedance matching". In: *Phys. Rev. Applied* 5.3 (2016), p. 34011. DOI: 10.1103/PhysRevApplied.5.034011.

[78] Ben H Schneider et al. "Observation of decoherence in a carbon nanotube mechanical resonator". In: *Nat. Commun.* 5 (2014), p. 5819. DOI: 10.1038/ncomms6819.

[79] B M Zwickl et al. "High quality mechanical and optical properties of commercial silicon nitride membranes". In: *Applied Physics Letters* 92.10 (2008), p. 103125. DOI: 10.1063/1.2884191.

[80] Stefan Weis et al. "Optomechanically induced transparency." In: *Science (New York, N.Y.)* 330.6010 (2010), pp. 1520–3. DOI: 10.1126/science.1195596.

[81] K-J Boller, A Imamoğlu, and Stephen E Harris. "Observation of electromagnetically induced transparency". In: *Physical Review Letters* 66.20 (1991), p. 2593. DOI: 10.1103/PhysRevLett.66.2593.

[82] A. H. Safavi-Naeini et al. "Electromagnetically induced transparency and slow light with optomechanics". In: *Nature* 472.7341 (2011), pp. 69–73. DOI: 10.1038/nature09933.

[83] M Karuza et al. "Optomechanically induced transparency in a membrane-in-the-middle setup at room temperature". In: *Physical Review A* 88.1 (2013), p. 013804. DOI: 10.1103/PhysRevA.88.013804.

[84] T.L. Nicholson *et. al.* "Systematic evaluation of an atomic clock at 2 x 10^{-18} total uncertainty". In: *Nat. Commun.* 6 (2015). DOI: 10.1038/ncomms7896.

[85] H. H affner *et. al.* "High-accuracy measurement of the magnetic moment anomaly of the electron bound in hydrogenlike carbon". In: *Phys. Rev. Lett.* 85 (25 2000), pp. 5308–5311. DOI: 10.1103/PhysRevLett.85.5308.

[86] V. Rajaraman. "IEEE Standard for Floating Point Numbers". In: *Resonance* 21 (1 2016), pp. 11–30. DOI: 10.1007/s12045-016-0292-x.

[87] Paul Erker et al. "Autonomous Quantum Clocks: Does Thermodynamics Limit Our Ability to Measure Time?" In: *Physical Review X* 7.3 (2017). DOI: 10.1103/physrevx.7.031022.

[88] Andre C. Barato and Udo Seifert. "Cost and Precision of Brownian Clocks". In: *Physical Review X* 6.4 (2016). DOI: 10.1103/physrevx.6.041053.

[89] John Goold et al. "The role of quantum information in thermodynamics—a topical review". In: *Journal of Physics A: Mathematical and Theoretical* 49.14 (2016), p. 143001. DOI: 10.1088/1751-8113/49/14/143001.

[90] Gonzalo Manzano, Ralph Silva, and Juan M. R. Parrondo. "Autonomous thermal machine for amplification and control of energetic coherence". In: *Physical Review E* 99.4 (2019). DOI: 10.1103/physreve.99.042135.

[91] Obinna Abah et al. "Energetic cost of quantum control protocols". In: *New Journal of Physics* 21.10 (2019), p. 103048. DOI: 10.1088/1367-2630/ab4c8c.

[92] Fabien Clivaz et al. "Unifying Paradigms of Quantum Refrigeration: A Universal and Attainable Bound on Cooling". In: *Physical Review Letters* 123.17 (2019). DOI: 10.1103/physrevlett.123.170605.

[93] Christian Gogolin and Jens Eisert. "Equilibration, thermalisation, and the emergence of statistical mechanics in closed quantum systems". In: *Reports on Progress in Physics* 79.5 (2016), p. 056001. DOI: 10.1088/0034-4885/79/5/056001.

[94] J. Eisert, M. Friesdorf, and C. Gogolin. "Quantum many-body systems out of equilibrium". In: *Nature Physics* 11.2 (2015), 124–130. DOI: 10.1038/nphys3215.

[95] Mark T. Mitchison. "Quantum thermal absorption machines: refrigerators, engines and clocks". In: *Contemporary Physics* 60.2 (2019), 164–187. DOI: 10.1080/00107514.2019.1631555.

[96] Paul Erker. "The Quantum Hourglass - Approaching time measurement with quantum information theory". In: *Master Thesis, ETH Zurich* (2014).

[97] M. Brunelli et al. "Experimental Determination of Irreversible Entropy Production in out-of-Equilibrium Mesoscopic Quantum Systems". In: *Phys. Rev. Lett.* 121 (2018), p. 160604. DOI: 10.1103/PhysRevLett.121.160604.

[98] Luca Gammaitoni et al. "Stochastic resonance". In: *Rev. Mod. Phys.* 70 (1 1998), pp. 223–287. DOI: 10.1103/RevModPhys.70.223.

[99] Claus Gűrtner et al. "Integrated optomechanical arrays of two high reflectivity SiN membranes". In: *Nano letters* 18.11 (2018), pp. 7171–7175. DOI: 10.1021/acs.nanolett.8b03240.

[100] Erwin Peiner et al. "Diamond-like carbon for MEMS". In: *Journal of Micromechanics and Microengineering* 17.7 (2007), S83. DOI: 10.1088/0960-1317/17/7/S04.

[101] Oliver Dial et al. "Bulk and surface loss in superconducting transmon qubits". In: *Superconductor Science and Technology* 29.4 (2016), p. 044001. DOI: 10.1088/0953-2048/29/4/044001.

[102] M Göppl et al. "Coplanar waveguide resonators for circuit quantum electrodynamics". In: *Journal of Applied Physics* 104.11 (2008), p. 113904. DOI: 10.1063/1.3010859.

[103] A. P. Sears. "Extending Coherence in Superconducting Qubits: from microseconds to milliseconds". PhD Thesis. Yale, 2013.

[104] Michael Cerna and Audrey F Harvey. *The fundamentals of FFT-based signal analysis and measurement*. Tech. rep. Application Note 041, National Instruments, 2000.

[105] Maximilian Schlosshauer, Johannes Kofler, and Anton Zeilinger. "A snapshot of foundational attitudes toward quantum mechanics". In: *Studies in History and Philosophy of Science Part B* 44.3 (2013), pp. 222–230. DOI: 10.1016/j.shpsb.2013.04.004.

[106] Richard Feynman. *Feynman Lectures on Gravitation*. eng. 1st. CRC Press, 2018. DOI: 10.1201/9780429502859.

[107] Franck Laloë. "A model of quantum collapse induced by gravity". In: *The European Physical Journal D* 74.2 (2020), pp. 1–9.

[108] Lajos Diósi. "A universal master equation for the gravitational violation of quantum mechanics". In: *Physics letters A* 120.8 (1987), pp. 377–381. DOI: 10.1016/0375-9601(87)90681-5.

[109] Lajos Diósi. "Models for universal reduction of macroscopic quantum fluctuations". In: *Physical Review A* 40.3 (1989), p. 1165. DOI: 10.1103/PhysRevA.40.1165.

[110] Lajos Diósi. "The gravity-related decoherence master equation from hybrid dynamics". In: *Journal of Physics: Conference Series*. Vol. 306. 1. 2011. DOI: 10.1088/1742-6596/306/1/012006.

[111] Roger Penrose. "On gravity's role in quantum state reduction". In: *General relativity and gravitation* 28.5 (1996), pp. 581–600. DOI: 10.1007/BF02105068.

[112] Gian Carlo Ghirardi, Philip Pearle, and Alberto Rimini. "Markov processes in Hilbert space and continuous spontaneous localization of systems of identical particles". In: *Physical Review A* 42.1 (1990), p. 78. DOI: 10.1103/PhysRevA.42.78.

[113] Natacha Altamirano et al. "Gravity is not a pairwise local classical channel". In: *Classical and Quantum Gravity* 35.14 (2018), p. 145005. DOI: 10.1088/1361-6382/aac72f.

[114] David M Pozar. *Microwave engineering*. Wiley, 1998.

[115] Robert Henry Dicke. "The measurement of thermal radiation at microwave frequencies". In: *Classics in Radio Astronomy*. Springer, 1946, pp. 106–113. DOI: 10.1007/978-94-009-7752-5_11.

[116] H M Wiseman and G J Milburn. *Quantum Measurement and Control*. Cambridge University Press, 2009. DOI: 10.1017/CBO9780511813948.

[117] Kurt Jacobs and Daniel A. Steck. "A straightforward introduction to continuous quantum measurement". In: *Contemporary Physics* 47.5 (2006), pp. 279–303. DOI: 10.1080/00107510601101934.